



# Università degli studi di Trento

Dipartimento di Fisica

Ph.D. thesis - XXII Cycle

## Light-matter interaction in silicon nanophotonic structures

**Candidate:**  
Alessandro Pitanti

**Supervisor:**  
Prof. Lorenzo Pavesi

February 2010



*To the memory of my father.*

*Haud igitur penitus pereunt quaecumque videntur,  
quando alit ex alio reficit natura nec ullam  
rem gigni patitur nisi morte adiuta aliena.*

# Contents

|  |            |
|--|------------|
| <b>Introduction</b>  | <b>1</b>   |
| <b>1 Silicon nanocrystals and rare earth ions for light amplification</b>                        | <b>5</b>   |
| 1.1 Materials under investigation  | 7          |
| 1.1.1 Nanostructured Silicon   | 7          |
| 1.1.2 Rare Earth Erbium  | 9          |
| 1.2 Energy transfer in Si-nc:Er codoped silicon dioxide material                                 | 11         |
| 1.3 Quantitative optical characterization of waveguide amplifiers                                | 28         |
| 1.3.1 Quantitative photoluminescence analysis: coupled and active<br>Er <sup>3+</sup> fraction   | 29         |
| 1.3.2 Enhancement and losses in slab and channel waveguides                                      | 32         |
| 1.4 Conclusions  | 47         |
| Appendix to chapter 1  | 48         |
| Transfer mechanism in re-annealed samples  | 48         |
| <b>2 Microdisk resonators: photoluminescence, strain engineering and<br/>Purcell enhancement</b> | <b>51</b>  |
| 2.1 Active microresonator with Si-np   | 52         |
| 2.1.1 Hybrid structure and strain engineering: kylix microresonators                             | 61         |
| 2.1.2 Purcell effect   | 66         |
| 2.2 Vertically coupled passive microresonators   | 75         |
| 2.3 Conclusions and future perspectives  | 79         |
| <b>3 Light-matter interaction enhancements in slow-light waveguides</b>                          | <b>82</b>  |
| 3.1 Slow light in silicon coupled cavities waveguides  | 83         |
| 3.2 LDOS, Purcell factor and superradiance in Si-patterned slot waveguides                       | 94         |
| 3.3 Conclusions  | 106        |
| Appendix to chapter 3  | 107        |
| Electromagnetic Green's tensor determination in FDTD scheme                                      | 107        |
| <b>Conclusions</b>   | <b>108</b> |
| <b>Acknowledgments</b>   | <b>114</b> |
| <b>Bibliography</b>  | <b>116</b> |

# Introduction

Though different at a first sight, light and matter share many properties which become apparent only when the right length scale is considered. In 1924, Louis De Broglie extended the dualism particle-wave, which were a symptomatic characteristic of photons, to all matter, connecting to every momentum  $p$  a wavelength  $\lambda = h/p$ , with  $h$  Planck's constant. Electrons have then been confined in low-dimensional systems in similar way to what happens to light in microcavities. Both 1D (quantum well), 2D (quantum wire) and 3D (quantum dot) confinements have been realized [1], offering the platform where novel physical phenomena can be investigated. This approach allows, to a certain degree, to tailor the optical properties of semiconductors, in which an enhancement of absorption, emission or optical nonlinearity can be achieved. The booming optoelectronic industry has specialized in this kind of research, realizing several novel devices, such as high-brilliance Light-Emitting Diodes (LEDs), blue laser diodes or Quantum Cascade Lasers. All these exploit the electronic confinement effect. Even poor optoelectronic materials, such as bulk Si, have revealed material gain and enhanced light emission when reduced to nanometric size (Si-nanoparticle) [2].

Nowadays, the possibility to employ electronic quantum confinement, though widely spread, it is not always sufficient to get high performance optoelectronic devices or to reach particular physical regimes. A smart solution, in this sense, is to add the contribution of light to the recipe. Very similarly to electrons in potential wells, but at different length scale, photons can be confined and controlled, even if their bosonic nature, in comparison with the electrons fermionic one, changes the physical effects which can be observed. By the contemporary modification of the electronic and photonic density of states, the optoelectronic materials can then be further tuned towards the desired function. Moreover, new functionalities can be added and new physical effects explored.

In the common meaning, with the term "light-matter interactions" are indicated all the physical phenomena in which the coupling between the photon and electrons/excitons is so strong that is not anymore possible consider them as separate physical entities. In this regime, known as strong coupling, mixed electrons/photons (excitons/photons) eigenstates are formed. However, important interactions between light and matter can be found even in the weak coupling regime in which, though maintaining a separate nature, light and matter deeply influences each other. In this thesis, the weak coupling regime will be explored showing the possibility to investigate a rich and interesting physics, which is usually neglected in this line of research. Indeed, while the achievement of strong coupling requires extraordinary

experimental efforts, the weak coupling regime is present in everyday life, considering the simplest radiation absorption/emission of light from matter. More complicated effects, such as stimulated emission or nonlinear optics are widely used by optoelectronic industry, while a novel class of physical phenomena, like Purcell effect or quantum dots (QDs) superradiance are widely investigated by the cutting-edge research and could offer smart solutions for technological advancements.

In this thesis the light matter interaction in weak coupling regime is investigated in several, different systems. Being an experimental work, even if not all the research is devoted to the development of real world applications, the parts dealing with theory and simulations have a strong empirical look, considering the feasibility to realize measurable samples.

Additionally, most of the samples analyzed, discussed or designed in this work are based on group-IV Si element, which not only represents an optimal platform to investigate fundamental physics, but in case of high-impact discoveries, offers high rewards in terms of technological transfer. Since this material has been so important in the development of integrated circuits technology and could play a prominent role in the all-optical chip research line, a brief deepening on the subject is required.

## Why Silicon ?

Bulk silicon is a group IV semiconductor, with good electrical, mechanical and thermal stability. Due to its abundance in the Earth's crust and the large numbers of methods which allow a good purification of the element, Si has been historically one of the most used materials in construction/siderurgic industry. Only last century has witnessed the rise of Si as the key material for integrated electronics. In fact Si possesses an insulating oxide ( $\text{SiO}_2$ ), which can act as a good diffusion barrier; adding to that the possibility of easy donor and acceptor doping, make Si a good material for CMOS-related transistors production. Considering the cheap material manufacturability and the rise of Very-Large-Scale-Integration (VLSI) technology, Si has been essential to the maturation of integrated circuit technology and to the ascend of computer industry.

In 1965 Moore's predicted that the number of transistors which can be placed in an integrated circuit will double every two years [3]. While this trend has been well verified up to the beginning of 21<sup>st</sup> century, as stated by Moore himself, the doubling effect can not be perpetually sustained and definitively has to reach its own limit. Most importantly, the number of transistors is not linear with the computing performance (CPU), and alternative methods which allow a CPU improvement without resorting to an increased number of transistors would be suitable for technological advancement and could represent a breakthrough respect to Moore's original hypothesis. Nowadays, the main limitation imposed in CPU performance is given by heating of electrical interconnects, which links the logic gates together. While the possibility of getting faster processors exists (overclocking), thermal dissipation is then the main hindrance toward faster computers.

Fascinating is the possibility to link the logic gates together substituting the electrons in metallic wires with photons in optical fibers, which propagates without any

sensible heating in the structure. In this sense, the whole substitution of electronic interconnects with all-optical networks could represent a strong technological jump. The optical network should be easily integrable in pre-existing electronic structures, that is it has to be produced employing CMOS-related technology. Again silicon, for certain aspects, appears as a perfect material for this task. Its large refractive index in the near-infrared spectral region, together with the low refractive index of silicon oxide, make light transport possible. Unfortunately, its poor light emitting properties make the use of this element as integrated light source an awkward reality. Silicon-nanoparticles (Si-np) have partially resolved this problem, showing improved light emission and optical gain (in the visible) respect to their bulk counterpart. Even if this is case, strong detrimental effects (Auger recombination) and difficult control of nanocrystal fabrication at the nanoscale, makes the realization of Si-based laser a difficult task, when only electronic quantum confinement is considered. If the light is considered in the game, several possibilities arise, which are currently widely investigated by many different research groups in the world. The work in this thesis is inserted in this context: while on one side it can be placed in the seeking of Si-based light source field, on the other presents a general investigation of light matter interactions related effects in Si based materials.

In chapter 1 a pure spectroscopic study of an innovative Er-doped Silicon-Rich-Silicon-Oxide (SRSO) material is presented. In this case, the influence of matter (spontaneous/stimulated emission, absorption) over light is considered. Er-doped SiO<sub>2</sub> material is the haul of telecommunication industry for optical amplification, being its emission tuned with the third telecom window (i.e. about 1.55  $\mu\text{m}$ ). The current existing amplifiers are organized in very long doped fiber (EDFA), which requires an optical excitation, supplied by expensive and spectrally narrow laser sources. When Si-np are added to Er-doped SiO<sub>2</sub>, a sensitization effect, which increase the ions effective absorption cross section, is found. This opens the route towards compact, waveguide amplifiers (EDWA), pumped by spectrally broad LEDs. Intriguing is the possibility to resort to electrical injection schemes, which are not realizable in standard EDFAs.

Before the realization of working devices an understanding of the energy transfer physics is compulsory. In section 1.2, accurate experiments in which the energy transfer is analyzed are presented. The main achievement of this work is the identification of the transfer mechanism (Dexter transfer) and the verification that no intrinsic limit exists to the population inversion condition, opposing to the most recent findings in the literature.

Considering a set of optimized samples, quantitative optical experiments, devoted to the evaluation of the number of coupled/active Er<sup>3+</sup> ions and to the Er-doped SRSO active waveguide performances, are reported in sec. 1.3. By means of pump & probe experiments an internal gain of 1 dB/cm has been measured, while a coupled population of 56 % of active Er<sup>3+</sup> concentration has been found. Both these values, even if not enough to have a working device, are the best ever reported in the literature.

Chapter 2 deals with the possibility to trap and control light by means of az-

imuthally symmetric dielectric microcavities (Whispering Gallery Mode - WGM - cavities). Embedded Si-np can be efficiently employed to inject light within the cavity, while on the other side, light propagation investigation can furnish useful insights on material optical characteristics. The possibility to control light is manifested in a new class of WGM resonators (micro-kylix), which are described in sec. 2.1.1. Here, strain engineering is used to realize a quality factor (Q) tuning, blue-shifting the highest Q up to 60nm with respect to standard resonator of the same size.

In section 2.1.2, a case in which light influences matter is presented, evaluating the Purcell factor ( $F_P$ ) in Si-np active microdisk resonators. Despite being far from ideality, a Purcell enhancement, that is an increase in spontaneous emission rate due to large photonic density of states (DOS), can be revealed for Si-np. Moreover, a new technique is proposed to estimate the optical linewidth with which the emitters are coupled to cavity modes.

Finally, section 2.2 reports simulations and design of vertically-coupled microdisks. If Si-np Kerr nonlinearity is considered, interesting physical phenomena, such as an optical analogous of superconductor Josephson oscillations, can be achieved. This regime is reached when Optical Parametric Oscillations are realized, representing an effective Si-based light source, though optically excited.

In chapter 3 some applications of Si-based slow light waveguides are discussed. Due to the longer interaction time dictated by the slowing down effects, light-matter interactions are strongly enhanced in these devices. In particular, a photonic crystal waveguide design is presented in sec. 3.1. Here slot waveguides, where the electrical field can be localized in low-index materials, are used as a substrate to realize coupled-cavities photonic crystals, directly etched within the waveguide itself. The small group velocity greatly increases the optical nonlinearity of the material interacting with the optical field, being the enhancement factor equals to  $(c/v_g)^2$ . The slot peculiarity offers again the possibility to employ low index SRSO as nonlinear material embedded in Si-based waveguides. When the waveguide is properly designed, a quasi-flat transmission band can be achieved, with the important result of having undistorted propagation of pulses in the structure.

The small group velocity (increased photonic DOS) and field localization effects can be exploited to have large Purcell factors for an ensemble of many emitters, whereas in standard waveguide spatial correction effects produce large  $F_P$  only for the few emitters close to a field antinode (in sec. 3.2). This situation sounds interesting to verify the theoretically predicted bandgap superradiance, in which the light influences the matter, realizing a collective, coherent spontaneous emission effect.

As conclusions, some future perspective and possibilities for this line of research are discussed.

# Chapter 1

## Silicon nanocrystals and rare earth ions for light amplification

Let us consider an atomic two level system (of energy  $E_i$  and population  $n_i$ ) in thermal equilibrium with a radiation photon field of energy  $\hbar\omega = E_2 - E_1$ . It is a well known fact that the processes which govern photons and electrons dynamics are not only spontaneous emission, but even stimulated emission and absorption. These latter require a direct interaction between the atomic charges and the photon field: in stimulated absorption one photon exchanges its energy with a ground state electron, promoting it to the excited state, while in stimulated emission one electron relaxes from the excited level triggered by a radiation field photon and emitting at the same time one additional photon which is *coherent* with the first one.

Following Einstein's considerations, this kind of light matter interaction effects can then be totally described employing three probability coefficients (Einstein's coefficients):

$$\begin{aligned} A_{12} &= \frac{g_1}{g_2} \frac{2\omega^2 e^2}{m_e c^3} f_{12} && \text{Spontaneous emission,} \\ B_{12} &= \frac{4\pi e^2}{m_e \hbar c} f_{12} && \text{Stimulated emission,} \\ B_{21} &= \frac{g_1}{g_2} \frac{4\pi e^2}{m_e \hbar c} f_{12} && \text{Stimulated absorption,} \end{aligned} \tag{1.1}$$

where  $e$  and  $m_e$  are the electron mass and charge,  $\hbar$  is the reduced Planck's constant and  $c$  the vacuum speed of light.  $g_i$  represents the level degeneration while  $f_{12}$  is the transition oscillator strength.

The production of coherent photons in stimulated emission sounds fascinating for the possibility to generate a beam of indistinguishable particles with narrow spectral width and collimated propagation direction.

It is worth to note that stimulated emission probability is given by the product  $\hbar\omega/4\pi n_2 B_{12}$ , where  $n_2$  is the atomic excited state population. Since the occupancy of the excited state is a non-equilibrium condition, external energy injection is required to promote electrons to this level and eventually exploit stimulated emission. This can be done injecting energy in the atomic system, both with optical or electrical means. Considering for the sake of discussion  $g_1 = g_2$ , it is worth to define the

material absorption coefficient as:

$$\alpha = \frac{\hbar\omega}{4\pi}(n_2B_{12} - n_1B_{21}) = \frac{\hbar\omega}{4\pi}B_{12}(n_2 - n_1), \quad (1.2)$$

which represents the fraction of light absorbed by the material per unit distance. When  $n_1 > n_2$ ,  $\alpha < 0$  and the light intensity is decreased by the interaction with the material. On the other hand, when  $n_1 < n_2$  (population inversion),  $\alpha > 0$ , resulting in an optical amplification of light traveling in the atomic system. Laser (Light Amplification by Stimulated Emission of Radiation) and optical amplifiers are based on the physical phenomena here described and have clearly represented a technological revolutions in different application fields. Even though some hybrid approaches exist, this kind of technology lacks, up to now, the CMOS compatibility, and so can not be implemented monolithically in integrated circuit technology. The possibility of having CMOS-compatible lasers, eventually electrically injected, would be a huge improvement towards the realization of all-optical chips. The intermediate stage of the research is then represented by the realization of CMOS-compatible optical amplifiers, considering materials in which the electrical injection can be realized.

In this chapter, I will present the main results of optical spectroscopic experiments towards the realization of a compact, erbium-based waveguide amplifier, which works in the third telecom window (i.e. around a wavelength of 1550nm). While Erbium-Doped-Fiber-Amplifiers (EDFA) are nowadays an affirmed and widely spread technology, the system has rooms for further improvements [4]. Particularly appealing is the possibility of employing novel, cheaper injection schemes (both optical or electrical), substituting the requirement of powerful, spectrally sharp laser excitation which is currently needed. The introduction of sensitizers is one of the possible route which can be followed to achieve such result. Silicon nanoparticles (Si-np) have been revealed to be a good candidate for this, producing an enhancement of erbium effective absorption cross section of several orders of magnitude when the ions are placed in close proximity to the semiconductor nanostructures [5]. Moreover, the material can be electrically injected and used as active layer in Silicon-Over-Insulator (SOI) based waveguides.

At first, I will introduce the materials under study separately, especially to understand the role of quantum mechanical effects in optical and electronic properties of nanostructured Si. After that, I will carefully describe spectroscopic experiments which investigates the physics behind the sensitization effect among silicon nanoparticles (Si-np) and  $\text{Er}^{3+}$  ions. The sample chosen for optical characterization has been selected in a wide set for its peculiar properties, which are the large number of  $\text{Er}^{3+}$  fraction coupled to Si-np and the (relatively) low confined carrier absorption related loss which is, up to now, the most important detrimental effect which prevents the achievement of net gain in the optical amplifier. The existence of intrinsic processes which limit the full energy transfer in the material, recently reported in several reports, is not an actual issue in the investigated sample, which shows the largest percent of coupled  $\text{Er}^{3+}$ , i.e. 56% of optically active ions, reported in literature. This promising material has been used to produce optical waveguide, prototypes and

demonstrators of the final device. In the last section of this chapter, I will report experimental results regarding the quantitative characterization of the waveguides, mainly in terms of optical amplification and losses. Finally, I will discuss some issues which prevent to reach net gain in the system, together with the future perspective and feasibility to get a working amplifier device.

## 1.1 Materials under investigation

### 1.1.1 Nanostructured Silicon

Even if considered the key material for integrated circuits, due to its cheap, CMOS compatible fabrication technology, semiconductor silicon has bad light emitting properties. As reported in fig. 1.1, the indirect nature of the electronic band gap (with a minimum of conduction band along the  $\Gamma$ - $X$  direction in the first Brillouin zone), makes necessary the absorption/emission of momentum-conserving phonons for excitons radiative recombinations. The probability associated with this indirect

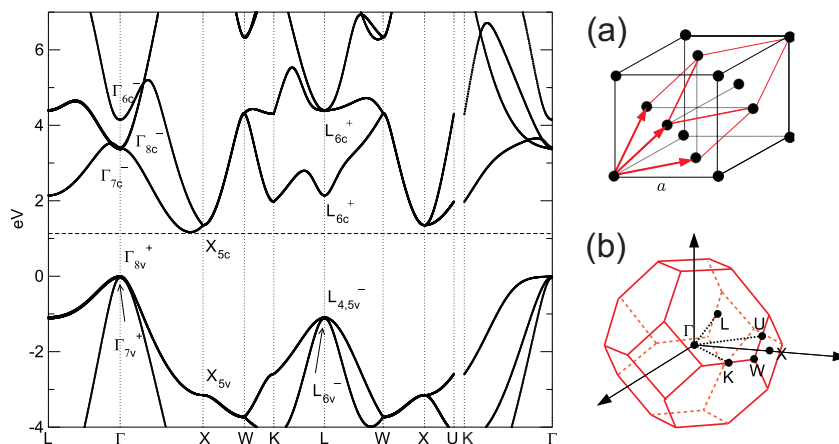


Figure 1.1: Electronic band structure of bulk Si. A schematic of the face centered lattice (fcc) fundamental cell (a) and first-Brillouin zone (b) is reported.

process is of the order of  $10^4 - 10^3 \text{ s}^{-1}$ , which is more than five orders of magnitude lower than the direct radiative recombination rate in III-V semiconductor materials (of the order of  $10^9 \text{ s}^{-1}$ ) [6]. This peculiarity makes non-radiative detrimental processes, such as Auger and Free Carrier Absorption, much more efficient in depleting the excitons population, *de facto* quenching the light emission from the material. Moreover, the large electron mobility ( $\sim 2 \times 10^3 \text{ cm}^2 \text{ V}^{-1} \text{ s}^{-1}$  [7]), makes the non-radiative recombinations, due to electrons encounter with matrix defects, a non-negligible effect which contributes in quenching the radiative recombination intensity.

To improve Si light emission performances, is thus necessary to increase the exciton radiative recombination rate and decrease electrons mobility. A possible route to accomplish such a task is to reduce the semiconductor to nanometric dimensions, where quantum mechanic effects are important and govern the electronic dispersion and, conversely, the light emission.

Silicon nanoparticles (Si-np) are nanometric sized (1 - 10 nm diameters) crystals which maintain the lattice structure of bulk silicon. The most common fabrication techniques are based on the deposition of a non-stoichiometric Silicon-Rich-Silicon-Oxide,  $\text{SiO}_x$  (SRSO). A following annealing step (with annealing temperature of 1000 - 1100°C), separates the Si excess from the Silicon oxide, forming individual, usually spherical, crystalline domains.

A simple model, which qualitatively displays the most important features of nanocrystalline Si, considers the single Si-np embedded in  $\text{SiO}_2$  insulator as a three-dimensional potential well for electronic confinement. Being the wavefunction strongly localized inside the well, electrons mobility is reduced with respect to the bulk Si one. Moreover, according to the indetermination principle, the spatial localization increases the momentum  $\vec{k}$  uncertainty, relaxing the  $\vec{k}$ -conservation rule with a consequent increase in optical transition rates. Figure 1.2 (a), shows an experiment in which

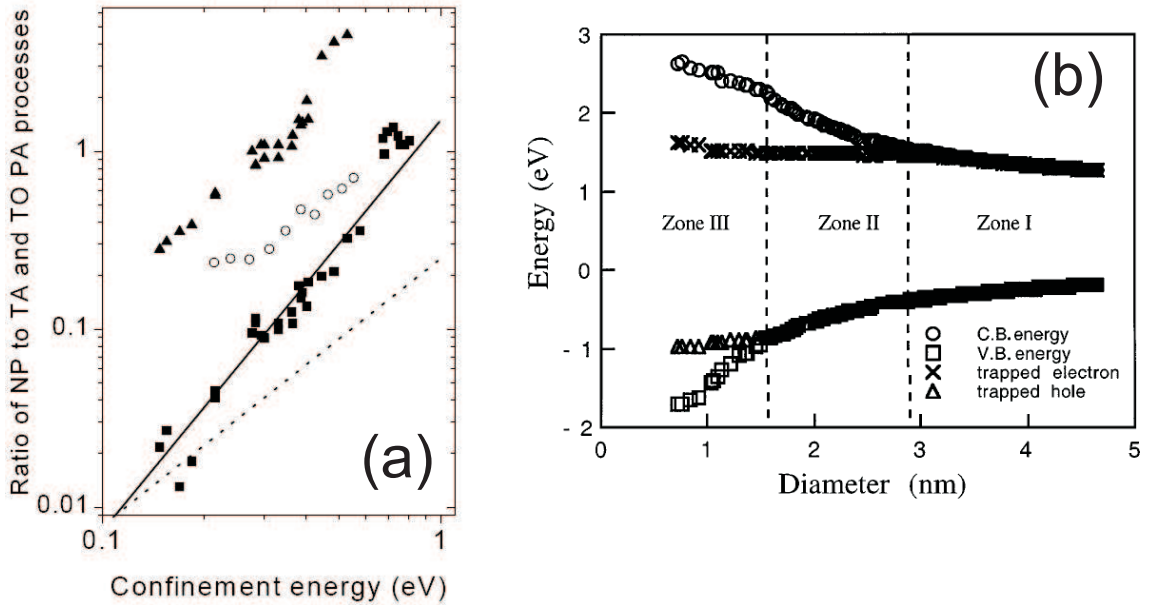


Figure 1.2: (a): Breakdown of  $\vec{k}$ -conservation rule for different Si-np sizes and samples (from [8]). (b): Blue-shift of electronic band gap for different Si-np sizes (from [9]).

the transition rates of No-Phonon (NP) direct transition is compared with Phonon-Assisted (PA) ones for different sample kinds as a function of excitons confinement energy (inversely proportional to the nanoparticle size). The white circles have been measured for Si-np samples and clearly show a progressive breakdown of the selection rule with the size reduction [8].

Even if the potential well model is able to explain the progressive blue-shift of the electronic band gap which is observed when Si-np size is reduced, it fails to re-create features which are related to the physics of Si-np surface, which becomes important especially for few-nm diameter particles. As shown in fig. 1.2 (b), the band gap blue shift effect halts when the excitons Bohr radius becomes comparable with the Si-np geometrical radius. In this region, surface-related recombinations and emission starts to rule out the quantum-confinement based light emission [9].

A simple model describing the whole Si-np physics is still lacking; in sec. 2.1.2 some

issues concerning the determination of Si-np optical constants will be addressed and the light emission properties described in a more detailed way.

### 1.1.2 Rare Earth Erbium

Erbium is a lanthanide trivalent material, 68<sup>th</sup> element in the periodic table of elements. Its electronic configuration is the following:

$$Er = [Kr] 4d^{10} 5s^2 5p^6 4f^{12} 6s^2,$$

with the shells 5s and 5p located more externally with respect to the chemical active electronic level 4f. When the material is embedded in a solid host, 5s and 5p orbitals act as an effective metal sphere, shielding the level 4f from the external environment coulomb interactions. Similarly to an isolated atom, 4f wavefunctions are very localized in close proximity of nuclei, giving rise to sharp absorption/emission lines. In comparison, the wavefunctions of standard semiconductor dopant are very delocalized, giving up electrons or holes as excess charges in the doped material. The electronic crystal field of the host, in which erbium is inserted, acts only as a perturbation on the 4f levels, lifting the orbital angular momentum degeneracy (Stark splitting). This effect is reflected in the optical transitions among levels within the 4f-shell: even if they are dipole-forbidden by parity dipole selection rule, they become quasi-forbidden due to the electric field perturbation, giving rise to very long transition lifetimes. Figure 1.3 reports a schematic of Er<sup>3+</sup> electronic configuration with the energies of the most common radiative transitions. It is worth

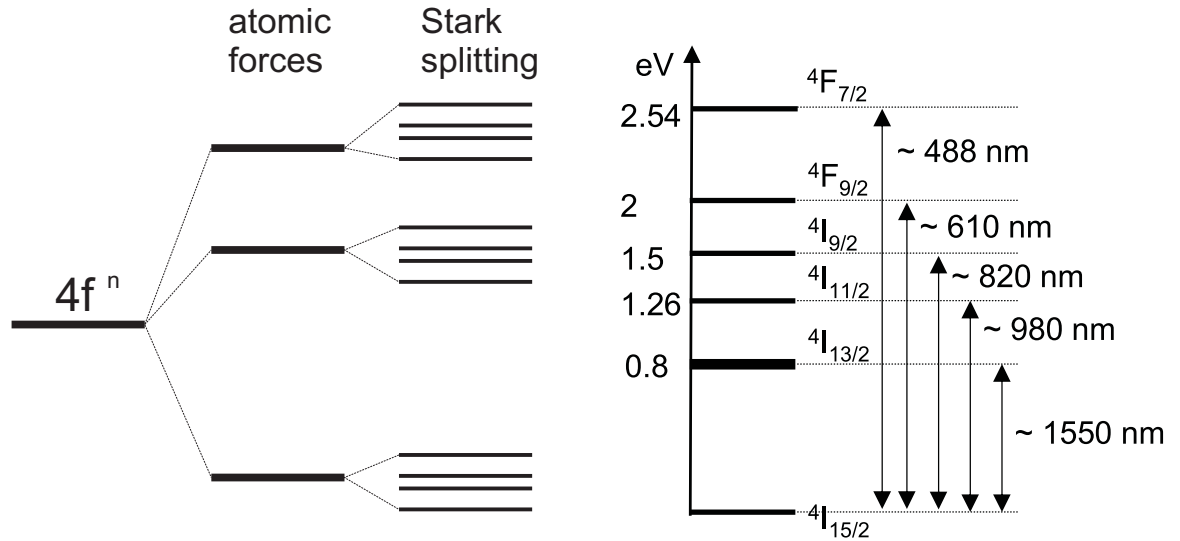


Figure 1.3: 4f levels splitting scheme. Energies and photon wavelengths of the most common radiative recombination transitions are reported.

to note that the  $4I_{13/2} \rightarrow 4I_{15/2}$  transition energy falls exactly in the third telecom window range, which corresponds to the low propagation loss region of optical fibers [4]. Typical lifetimes of this transition are of the order of milliseconds, making the reach of population inversion possible employing resonant optical excitation. Once

this condition is realized, a photon entering the material will be possibly amplified due to stimulated emission processes. This is usually done in long Er-doped optical fiber. Employing a counterpropagating excitation signal (pump laser, usually at a wavelength of 980nm), the probe signal (which in optical fibers can propagate with negligible losses), can be amplified by several dB if the fiber is long enough.

## 1.2 Energy transfer in Si-nc:Er codoped silicon dioxide material

Since the first reports of sensitization among silicon nanoparticles and  $\text{Er}^{3+}$  ions [5] and optical gain in the same system [12], a wide and focused research has started both towards the understanding of the physical mechanisms behind the energy transfer and towards the realization of an optical amplifier device. It is clear that this two approaches are tightly binded and new discoveries in the physical modeling can be efficiently transferred to the optimization of the working devices. Unfortunately, some different hypothesis exist about the energy transfer dynamics. Fujii and later Gregorkiewicz' groups reported the existence of two different energy transfer mechanisms, one slow ( $\sim \mu s$ ), in which high energy  $\text{Er}^{3+}$  levels are excited and one fast ( $\sim ns$ ), direct mechanism which promotes electrons to the first excited  $^4I_{13/2}$  level [13, 14]. It is worth to note that, together with this last one, the same group reported the observation of a fast mechanism (Auger back-transfer), which acts as an efficient de-excitation channel for  $\text{Er}^{3+}$  ions. According to their findings, even if the energy transfer can be very efficient, reaching 70% of inverted erbium ions at large excitation photon fluxes, the net inverted population, just after some nanoseconds from the pump pulsed excitation, is reduced to a few percent due to the back-transfer effect. This has been reported as an intrinsic limit of the system, which can not be overcome by technological advancements. Another model have been reported by Kik's group, which supports the existence of defect-related Luminescent Center (LCs) localized in the silicon dioxide matrix, which are the main responsible for the sensitization mechanism [15]. In fig. 1.4 a brief schematic which includes the

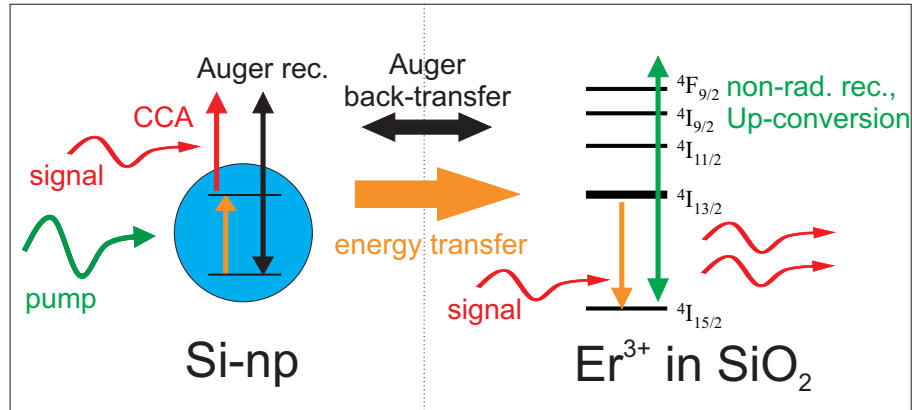


Figure 1.4: Schematic of the relevant physical mechanisms in Si-np and  $\text{Er}^{3+}$  ions regarding the energy transfer effect. All the mechanism here mentioned will be thorough described in the following sections.

relevant physical mechanism for the efficient ions sensitization is depicted. Apart from the debated energy transfer and Auger back-transfer effects, several degrading mechanisms exist which prevents the realization of stimulated emission processes from  $\text{Er}^{3+}$  ions. From Si-np side, intra-particle Auger recombination and Confined Carrier Absorption (CCA) related losses are the main issues to be addressed, while from  $\text{Er}^{3+}$  ions side cooperative up-conversion effects and non-radiative recombina-

tions have to be reduced to negligible contributions. If this is properly done, the achievement of  $\text{Er}^{3+}$  excitation and population inversion through sensitization from Si-np is expected.

In this section, I will report a contribution in understanding and modelling the physics behind the energy transfer within a semiempirical approach, in which the experimental results are used as the starting point for numerical solutions of a system of coupled rate equations, which describe  $\text{Er}^{3+}$  and Si-np population dynamics. Considering some of the features which emerge in the modelling, one expect to be able to couple a large fraction of  $\text{Er}^{3+}$  ions in optimized samples. To check this hypothesis a quantification of coupled  $\text{Er}^{3+}$  ions has been performed, holding the largest value reported so far in the literature ( $\sim 56\%$ ) [16]; in waveguides with active layer made of the same material, a corresponding signal enhancement of 1 dB/cm has been found [17].

### Material fabrication

The Er:Si-np-codoped silicon oxide samples have been fabricated with a radio-frequency (RF) reactive magnetron co-sputtering technique by CIMAP-Ensicaen research institute (Caen - France). The deposition has been performed in a controlled argon-hydrogen mixtured environment employing pure  $\text{SiO}_2$  and  $\text{Er}_2\text{O}_3$  targets. The non-stoichiometric Silicon Oxide deposition made possible the formation of silicon nanoparticles by a post-deposition annealing treatment which has been performed at different temperatures, in order to selectively grow amorphous ( $T_{ann.} \leq 900^\circ$ ) or crytalline nanoparticles ( $T_{ann.} \geq 1000^\circ$ ) [11]. More details on material deposition can be found elsewhere [10]. In order to properly analyze the effects of energy transfer, a wide set of samples has been prepared, modifying the deposition parameters (substrate temperature, RF power on targets and the Hydrogen rate in the Hydrogen-Argon mixture). The Si content and  $\text{Er}^{3+}$  concentration have been chosen in order to minimize Confined Carrier Absorption effect, as will be reported in sec. 1.3. The most promising sample in terms of transfer efficiency has been chosen as active layer in rib or rib-loaded waveguides, which have then been tested in pump & probe experiments. The lithographic processing has been performed by ORC - Optoelectronic Center (Southampton - UK).

Before optical characterization, the deposition technique has been tested for reproducibility and sample homogeneity within the 4-inches wafer. This last check has been performed by multi-points m-line measurements [18], in which ordinary and extraordinary refractive indices and thickness have been checked for consistency.

### Experiments and modeling

To investigate the energy transfer mechanism, a set of SRSO twin samples, of which only one has been Er-doped, has been considered. The sample configuration has been selected as the most efficient in terms of Si-np to  $\text{Er}^{3+}$  coupling. This last has been evaluated employing two figures of merit: the photoluminescence (PL) inten-

sity under non-resonant pumping (i.e. 476nm pumping)<sup>1</sup> and the lifetime of the first excited ( $^4I_{13/2}$ )  $\text{Er}^{3+}$  level. Table 1.1 reports the material composition of the samples under analysis. The active layer thickness is  $1.2\mu\text{m}$  in both samples, estimated

| Sample | Si exc (%)  | $[\text{Er}^{3+}][\text{cm}^{-3}]$ | $T_{ann}[\text{°C}]$ |
|--------|-------------|------------------------------------|----------------------|
| A      | $5 \pm 2$   | $3.38 \pm 0.2 \times 10^{20}$      | 900                  |
| B      | $6.3 \pm 2$ | -                                  | 900                  |
| C      | -           | $0.5 \pm 0.1 \times 10^{20}$       | -                    |

Table 1.1: Set of samples under study. Si excess (Si exc) and  $\text{Er}^{3+}$  concentration have been measured, respectively, by XPS and SIMS technique. The annealing time was of one hour.

with m-line technique. In both samples a bottom,  $5\mu\text{m}$   $\text{SiO}_2$  cladding is present to isolate the active material from the Si substrate on which the samples are grown. As a reference sample, a Er-doped Corning glass (1 mm total thickness), of which the total erbium concentration has been reported in tab. 1.1, has been considered (sample C).

Figure 1.5 reports a typical photoluminescence (PL) spectrum of sample A when excited with a continuous wave (CW) laser source at a wavelength which is non-resonant with any  $\text{Er}^{3+}$  ions internal transition. Several features can be noted in the

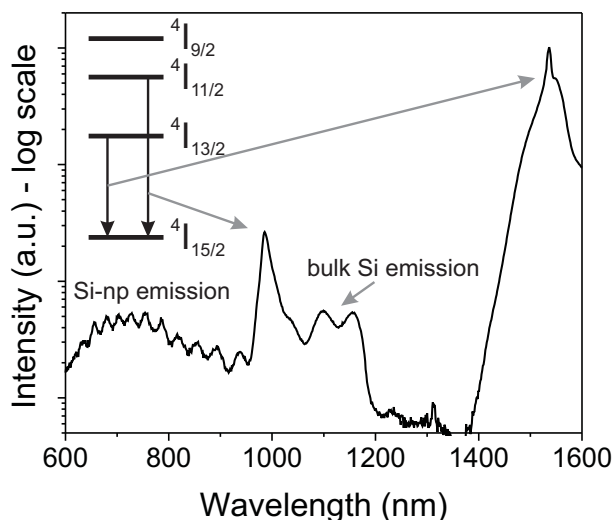


Figure 1.5: Photoluminescence spectrum of sample A under non-resonant pumping (476nm).

picture.  $\text{Er}^{3+}$  radiative transitions from levels  $^4I_{13/2}$  and  $^4I_{11/2}$  to the fundamental  $^4I_{15/2}$ , clearly appear as emission lines centered, respectively, at 1535 and 980nm. Since the excitation is non-resonant, the infrared emission is due to energy transfer among nanoparticles and  $\text{Er}^{3+}$  ions. Despite the low annealing temperature of 900  $^{\circ}\text{C}$ , which is expected to produce amorphous Si-nanoclusters [11], the emission band of Si-np is clearly visible, centered at about 700nm. The interference fringes which

<sup>1</sup>Photoluminescence refers to the process of spontaneous emission (proportional to Einstein's coefficient  $A_{21}$ ), when the sample is excited with optical means.

appear in the band are due to multiple reflections in the SiO<sub>2</sub> bottom cladding. Finally, the small band at about 1100 nm is the emission from the bulk Si substrate. The detailed investigations of the different spectral features which appear in fig. 1.5 allows one to perform an accurate modeling of the system: investigating the infrared (IR) region of the spectrum, that is the region typical of Er<sup>3+</sup> ions emission, it is possible to understand the impact of Auger back transfer mechanism and transfer efficiency in the samples. On the other hand, from visible spectroscopy (VIS), it is possible to study the dynamics of Si-np emission and infer the physics behind the energy transfer itself. When the two results are joined together, a clear picture can be drawn. Therefore, it is possible to model the data using numerical tools.

Unless otherwise stated, the spectroscopic experiments have been performed exciting the sample with the 355nm line of a pulsed Nd:YAG laser in a standard PL setup. The pulse width was of 10 ns, with a repetition rate of 10 Hz. The pump photon flux on the sample was  $1 \times 10^{25}$  ph./cm<sup>2</sup>s. The collection has been respectively performed using a CCD streak camera coupled to a spectrometer, with an overall time-resolution of the order of few picoseconds (VIS range), and a monochromator coupled with a nitrogen-cooled GaAs-PhotoMultiplier (PMT), with a time-resolution of some nanoseconds (IR range).

### Infrared spectroscopy experiments and results

As a starting point, the IR-PL emission from sample A and sample B has been measured in the experimental conditions described above. Fig. 1.6 reports the main results. The 2D maps show both the time evolution (y-axis) and the spectral de-

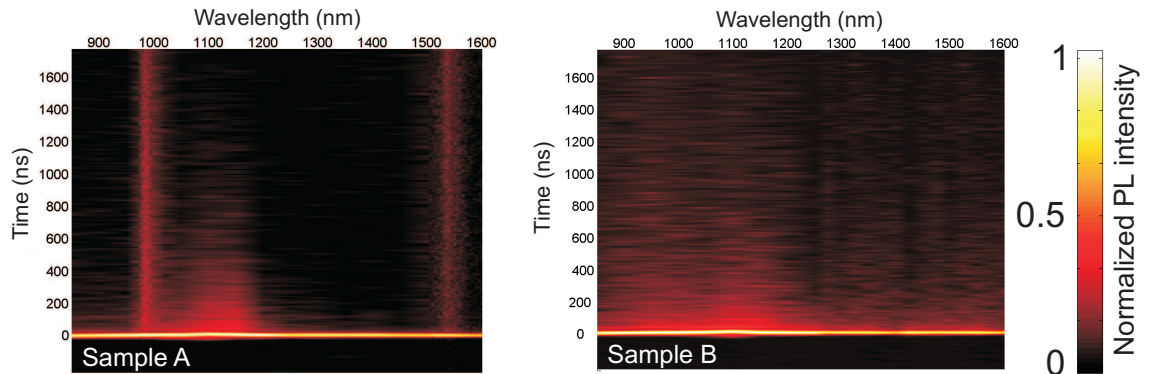


Figure 1.6: Time-Wavelength maps of PL emission from sample A and B. Note that the samples have been independently normalized.

pendence (x-axis) of the PL signals. The color scale from dark to bright colors represent the normalized emission intensity. The most striking feature in fig. 1.6 is the presence of a fast ( $< 100$ ns) decaying component which can be observed in both samples for every detection wavelengths. Moreover, while for sample A it is possible to clearly distinguish Er<sup>3+</sup> spectral features in the slow decaying emissions centered at about 980 and 1535nm, sample B shows a broad, weak emission band unrelated to Er<sup>3+</sup> ions emission. According to the observed results, the fast component can not

be attributed to the presence of  $\text{Er}^{3+}$  ions within the sample, since it is shown even in sample B decays. For the sake of clarity, fig. 1.7 (a) reports the single-wavelength decays, at different wavelengths, for sample A and sample B. It is possible to appreciate that the same dynamical features are present in all the decays, with the sole difference being the slow  $\text{Er}^{3+}$  emission at 1535nm in sample A. To get further insights about the origin of the fast lineshape in sample A, time-integrated spectra in a short [0:200ns] and in a long time-window [200ns:2 $\mu$ s] have been analyzed. The results are reported in fig. 1.7 (b). Neglecting the small perturbations in the short

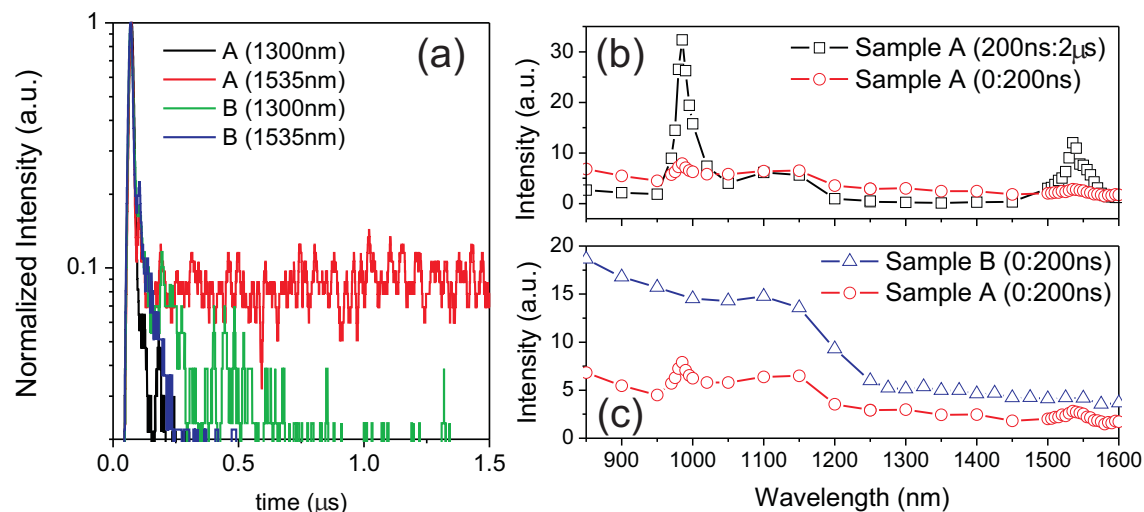


Figure 1.7: (a): Single wavelength decays in sample A and B. The fast lineshape dynamic is qualitatively the same for all the measurements. (b): Comparison of short [0:200ns] and long [200ns:2 $\mu$ s] time integrated spectra in sample A. (c): Comparison of short time integrated spectra in sample A and B

time-window integrated spectrum (red circles), which are due to signals convolution,  $\text{Er}^{3+}$  emission peaks appear only in the long time-window (black squares).

With this last observation, one can thus safely conclude that the fast decaying component is unrelated with the presence of  $\text{Er}^{3+}$  ions in the system. Since a very similar dynamic, observed in different samples, has been attributed to Auger back-transfer effects [14], one can infer that in samples under study no evidences of this kind of phenomenon have been experimentally observed. Finally it is worth to note that, when comparing the short time-window integrals in sample A and B, a non-negligible emission band is found, which intensity is quenched by about a factor 3 when erbium is inserted in the sample. This effect is qualitatively confirmed by independent measurements in different sets of samples. Its origin could be attributed to radiative emitting centers related to Si-np, as the ones reported in [19].

Additional informations can be inferred examining in more details the PL decay signals from level  ${}^4I_{11/2}$  and  ${}^4I_{13/2}$ , which are reported in fig. 1.8. The signal at 980nm ( ${}^4I_{11/2} \rightarrow {}^4I_{15/2}$  transition) after a steep rise is constantly decreasing as a single exponential function, with a time constant of  $4.6 \pm 0.5 \mu$ s. On the other hand, the 1535nm signal ( ${}^4I_{13/2} \rightarrow {}^4I_{15/2}$  transition) is rising with almost the same time constant ( $4.2 \pm 0.5 \mu$ s). It is not possible to compare directly the populations

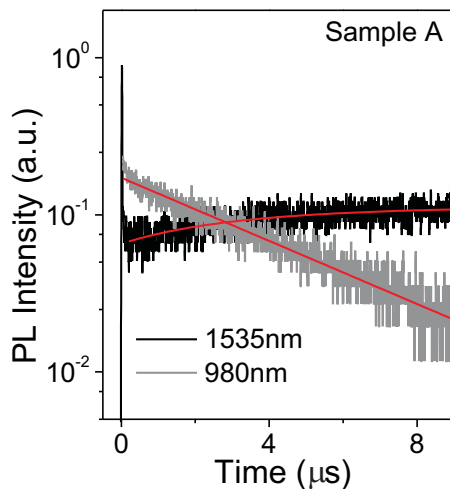


Figure 1.8: Comparison of  ${}^4I_{11/2} \rightarrow {}^4I_{15/2}$  and  ${}^4I_{13/2} \rightarrow {}^4I_{15/2}$  transition after the pump pulse in sample A. In red, single exponential fitting are reported, holding a decay time of  $4.6 \pm 0.5 \mu\text{s}$  (980nm signal) and a rise time of  $4.2 \pm 0.5 \mu\text{s}$  (1535nm signal).

in the two levels, since the PL intensities are inversely proportional to the unknown radiative lifetimes. If most of the energy transfer process involves the level  ${}^4I_{11/2}$ , one can assume that the level  ${}^4I_{13/2}$  is populated only through internal relaxation processes. In this case, the first excited state population  $N_{Er,2}$  temporal dependence can be extracted as:

$$N_{Er,2}(t) = N_{Er,3}(0) [e^{-t/\tau_{21}} - e^{-t/\tau_{32}}], \quad (1.3)$$

where  $\tau_{21}$  and  $\tau_{32}$  are respectively the PL lifetimes of the first (5.5ms) and second ( $\sim 4 \mu\text{s}$ ) excited state population, while  $N_{Er,3}(0)$  represents the second excited state population just after the laser pulse.

From eq. (1.3), one can get the relationship  $N_{Er,2}(t) < N_{Er,3}(0) \forall t$ , which is well verified in the experimental data reported in fig. 1.8. Moreover, the single exponential function observed in the decay suggests that no level energetically higher than  ${}^4I_{11/2}$  is excited during the transfer process. A stretched exponential function should be observed if that was the case [20].

Indeed, it is not possible to totally exclude an energy transfer mechanism which excites electrons directly to the  $\text{Er}^{3+}$  first excited state, since experimentally the first nanoseconds of PL dynamics are hidden by the fast decaying emission. Nevertheless, the reasons above mentioned suggest that one can expect that the main transfer contribution should be related to  $\text{Er}^{3+}$  second excited state.

## Visible spectroscopy experiments and results

Even though silicon nanoparticles conserve an amorphous nature, due to the low-temperature annealing treatment (900 °C), a clear emission band in the visible can be observed when the sample is CW-excited at 476nm, as reported for example in fig. 1.5. The amorphous nature of the nanoparticles can be inspected looking at the spectral decays in the visible. In fact, if the sample possesses an high crystalline

quality, a clear exponential spectral trend in the PL lifetimes is expected, due to the different electron-hole wavefunctions overlap in optical recombination processes [13]. Fig. 1.9 (a) reports the PL decay for different detection wavelengths in sample B. The long decay curves can be fitted by a stretched exponential function, which takes into account distribution of lifetimes due to excitonic transport phenomena, like inter-particle hopping [21, 22]. By fitting the data, the average PL lifetime  $\tau_{PL}$  is extracted as the first-order moment of the stretched exponential distribution [23]:

$$f(t) = y_0 + Ie^{-\left(\frac{t-t_0}{\tau}\right)^\beta}, \quad \tau_{PL} = \frac{\tau}{\beta} G\left[\frac{1}{\beta}\right], \quad (1.4)$$

where  $G[\cdot]$  is the Gamma-function. The average PL lifetime calculated with eq. (1.4)

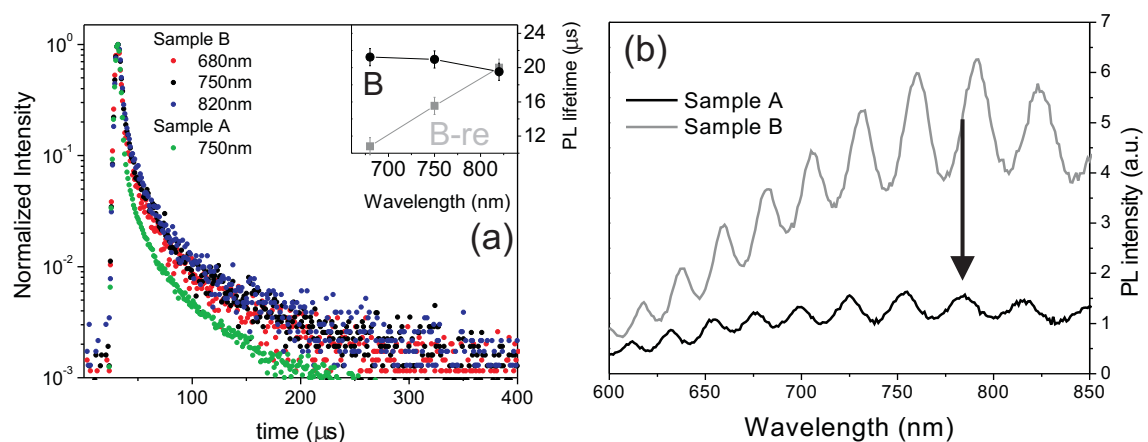


Figure 1.9: (a): Decay curves at different emission wavelengths for sample B. Sample A decay curve at 750nm is added for comparison. In the inset the extracted average PL lifetime is reported. (b): CW PL of sample A and sample B. The excitation wavelength was 476nm.

is reported in the inset of fig. 1.9 (a) and does not show the expected exponential spectral trend, confirming the amorphous nature of the nanoparticles. For comparison, in the same graph is reported the spectral lifetime of sample B-re, described in Appendix, which contains crystalline Si-np. When erbium is inserted in the sample, the PL lifetime is shortened, as can be observed for the 750nm emission of sample A reported in fig. 1.9 (a). The same results hold in all visible range (not shown), suggesting that the presence of  $\text{Er}^{3+}$  ions turns on a recombination mechanism which is directly or indirectly competitive with the radiative one. In particular, this is associated with the energy transfer process itself.

Together with the lifetime reduction it is possible to observe a threefold quenching of the PL intensities obtained under CW pumping (476nm) in sample A with respect to sample B (see fig. 1.9 (b)). The same behaviour is present, with the same qualitative trend, in different sample sets.

Since the radiative recombination probability is of the order of  $1 \times 10^6 \text{ s}^{-1}$ , while the average transfer time in the same excitation condition is of the order of tens of ns, with a corresponding probability of about  $1 \times 10^8 \text{ s}^{-1}$ , it is reasonable to suppose that, if the radiative recombination and the transfer mechanism were directly com-

petitive processes, a whole quenching of the PL emission should appear. Noteworthy is the fact that the PL emission band is quenched as a whole, without any spectral features which would suggest a resonant transfer mechanism. Both these aspects have to be considered in modeling of the system.

It is interesting to note that the same quenching factor has been found when the fast decaying lineshape in the IR was examined (see fig. 1.7). Even if not enough informations are available in order to make any assumptions regarding the origin of the fast component, this last observation allows tentatively to link the fast decaying lineshape emission with the presence of Si-np inside the matrix, strenghtening the hypothesis that this can be originated to the same radiative emitting centers reported in [19].

Inspecting the evolution of the PL intensity as a function of the exciting photon flux, it is possible to get some information about possible Auger effects in the samples.

Auger recombination is a three particles process in which an exciton recombines giving its energy to a nearby electron or hole which is promoted to high energy levels. In most cases, the fast excitation is followed by a fast particle thermalization, making the net results of the process the simple elimination of the exciton itself. Indeed,

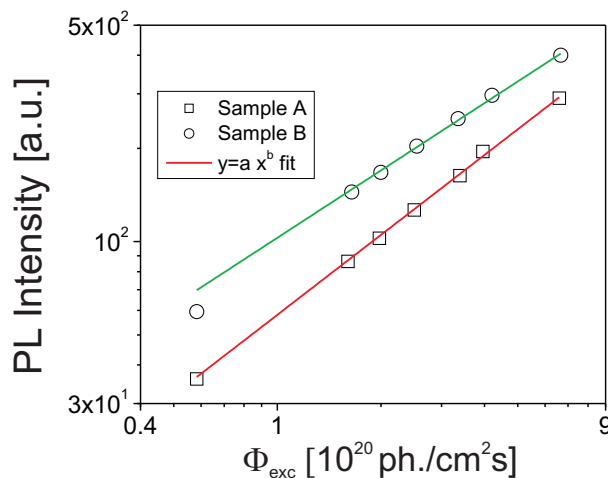


Figure 1.10: Visible CW-PL intensity as a function of pumping power. The integrated intensity over the whole spectrum is fitted with a power-law  $y = a \cdot x^b$  function, obtaining  $b=0.83\pm0.05$  ( $b=0.72\pm0.01$ ) for sample A (sample B).

this kind of mechanism can exist within the Si-np in a multi-excitons regime, in which more than one exciton per nanoparticle is created by the optical pump. Different Auger processes could involve excitons interaction among different Si-np in close proximity; the latter is evidently less probable than the standard intra-particle process and can be safely neglected. Auger can be simply modeled using a rate equation approach:

$$\frac{dN_{exc,1}}{dt} = \sigma_{Si-np} \Phi_{exc} N_{Si-np} - C_A N_{exc,1}^3 - B N_{exc,1}^2 - A N_{exc,1}, \quad (1.5)$$

where the exciton level  $N_{exc,1}$  is populated through an excitation term ( $\sigma_{Si-np}\Phi_{exc}N_{Si-np}$ ) and is depleted by three different recombination mechanisms: Auger recombination within the nanoparticle ( $C_A N_{exc,1}^3$ ), nongeminate radiative recombination ( $BN_{exc,1}^2$ ) and mono-molecular radiative recombination ( $AN_{exc,1}$ ) [24]. For a CW pumping at high fluxes, in which multi-excitons are created, the population recombination is dominated by the Auger term and it is then possible to neglect the last two terms of eq. (1.5). The steady state population is given by  $N_{exc,1} = K(N_{Si-np}\sigma_{Si-np}/C_A)^{1/3}\Phi_{exc}^{1/3}$ , where  $K$  is a constant depending on the sample geometry and absorption coefficient. The number of photons emitted is finally given by:

$$I_{PL} \propto BN_{exc,1}^2 = KB \left( \frac{N_{Si-np}\sigma_{Si-np}}{C_A} \right)^{2/3} \Phi_{exc}^{2/3}, \quad (1.6)$$

where the linear recombination contribution has been neglected. Eq. (1.6) demonstrates that the 2/3 power-law dependence is a clear signature of multi-excitons regime in which Auger effects dominates the steady-state population. As can be inspected in fig. 1.10, the PL intensity of sample B shows a good agreement with this model: the power-law fitting results in a power coefficient of  $0.72 \pm 0.1$ , whereas in dominated Auger-regime, an ideal coefficient of 0.66 is expected. Inter-particles Auger processes would have been characterized by a power coefficient of 0.5, confirming the hypothesis that these last effects have less impact in the samples population dynamics. The same measurements in sample A show an increase of power law coefficient toward the linear dependence (fitting results:  $0.86 \pm 0.3$ ). This can be interpreted considering a decrease of the exciton population, which could be due to the presence of the additional energy transfer recombination channel.

It is worth to conclude this section summarizing the experimental results, which acts as the starting point of the rate equation semi-empirical model which will be described in the nex section.

- When  $Er^{3+}$  is inserted in the sample, the VIS-PL lifetime is reduced with respect to the sample without  $Er^{3+}$  (fig. 1.9 (a)).
- The PL emission band in the visible is quenched as a whole without any apparent spectral features. The quenching is of about a factor 3. Nevertheless, a residual VIS-PL emission is still present in the sample with  $Er^{3+}$  (fig. 1.9) (b).
- Even at moderate pumping power ( $\Phi_{exc} = 1 \times 10^{19} ph.cm^{-2}s$ ), the samples are in good approximation in a multi-excitons regime, in which the population is dominated by Auger recombination (fig. 1.10).

### Rate equation semi-empirical modeling

While the optical properties of  $Er^{3+}$  ions in different matrices are well known, a careful study of the optical properties of Si-np can be performed only with extreme difficulty. The current fabrication processes do not allow a precise control of the

particles geometry at the nanoscale, producing an ensemble of nanoparticles with different sizes and geometries. Moreover a long debate exists about the origin of the luminescence in Si-np: it can originate from intrinsic properties of the nanoparticles (quantum-confinement PL) or from localized recombination at the Si-np surface [25]. All these effects make the modelling of electronic and optical properties of Si-np a very difficult challenge, which can be successfully performed only for an ideal system. For this reason, a more empirical approach has been chosen, in which the optical properties of the system are theoretically described by phenomenological rate equations. The kinetic of the populations is determined by a set of coupled rate equations which has been numerically solved to model the experimental data. Since

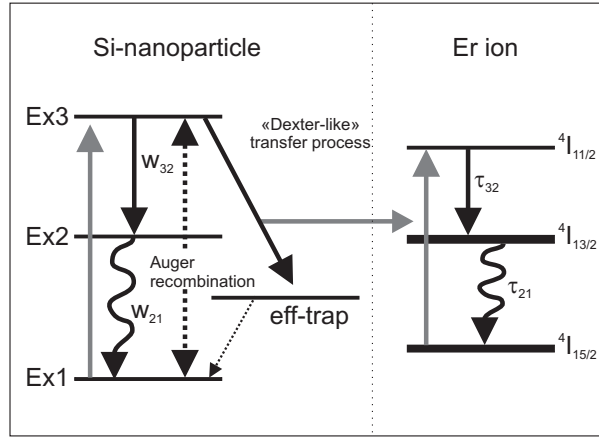


Figure 1.11: Schematic level for the rate equation system (1.7).

the main recombination paths of Si-np are identified as Auger recombination within the nanoparticle and transfer to nearby  $\text{Er}^{3+}$  ions, the fast dynamics of these two processes make necessary a careful investigation of the experimental PL decays in the first few nanoseconds time slot.

The following six coupled-equations system has been considered to model the Si-np/ $\text{Er}^{3+}$  interaction:

$$\begin{aligned}
 \frac{d}{dt}N_{exc,1} &= -\sigma_{Si-np}\Phi_{exc}(t)N_{Si-np} + 0.5C_A(N_{exc,2})^3, \\
 \frac{d}{dt}N_{exc,2} &= w_{32}N_{exc,3} - C_A(N_{exc,2})^3, \\
 \frac{d}{dt}N_{exc,3} &= \sigma_{Si-np}\Phi_{exc}(t)N_{Si-np} - w_{32}N_{exc,2} + 0.5C_A(N_{exc,2})^3 - kN_{exc,3}N_{Er,1}, \\
 \frac{d}{dt}N_{Er,1} &= -kN_{exc,3}N_{Er,1} + 1/\tau_{21}N_{Er,2}, \\
 \frac{d}{dt}N_{Er,2} &= 1/\tau_{32}N_{Er,3} - 1/\tau_{21}N_{Er,2}, \\
 \frac{d}{dt}N_{Er,3} &= kN_{exc,1}N_{Er,3} - 1/\tau_{32}N_{Er,3}.
 \end{aligned}
 \tag{1.7}$$

The Si-np excitonic levels are described by a three effective levels scheme (Ex1, Ex2, Ex3, of population  $N_{exc,1}$ ,  $N_{exc,2}$ ,  $N_{exc,3}$  respectively), while for the  $\text{Er}^{3+}$  ions the electronic population of level  ${}^4I_{15/2}$  ( $N_{Er,1}$ ),  ${}^4I_{13/2}$  ( $N_{Er,2}$ ) and  ${}^4I_{11/2}$  ( $N_{Er,3}$ ) has been considered. The corresponding energy level scheme is reported in fig. 1.11. The other symbols in eq. (1.7) have the following meaning:

- $\sigma_{Si-np}$ ,  $\Phi(t)$  and  $C_A$  are, respectively, the Si-np absorption cross section ( $\sim 1 \times 10^{15} \text{cm}^2$ , [26]), the photon flux at excitation wavelength (pump laser - 355nm) and the Auger coefficient. The pump laser temporal shape is a gaussian function with full width at half maximum of 10 ns as used in the experiments.
- $w_{ij}$  is the probability of the  $i \rightarrow j$  transitions while  $\tau_{ij}$  is the lifetime (inverse of the transition probability)<sup>2</sup>.
- $k$  is the distant dependent coupling constant for the energy transfer process among Si-np and  $\text{Er}^{3+}$  ions. Its value is directly proportional to the probability that the energy transfer occurs. More details regarding the physics behind the process will be addressed later.

The *non-geminate* and *geminate* recombination terms (respectively  $\propto N_{exc,2}^2$  and  $\propto N_{exc,2}$ ) have been neglected, since the Si-np excitonic levels population dynamic is dominated by Auger and energy transfer mechanisms in the first tens of nanoseconds after the excitation has been turned off. Moreover, since no sign of cooperative up-conversion mechanism (described in sec. 1.3.2) has been found in the investigated samples, it has been neglected in the model.

Once an exciton has been formed in level Ex3 by absorbing the 355nm photons, it can relax either to level Ex2 with a probability  $w_{32}$  or to an internal effective trap states, by giving back the energy to an  $\text{Er}^{3+}$  ion which gets excited. If relaxation to level Ex2 occurs, the carrier can be re-excited back to level Ex3 by an Auger process (which has been modelled with the terms  $C_A (N_{exc,2})^3$ ) or alternatively can radiatively recombine to the level Ex1, emitting photons responsible for the Si-np emission band reported, for example, in fig. 1.9.

The energy transfer process is accompanied by the promotion of one electron from the  $\text{Er}^{3+}$  fundamental state  ${}^4I_{15/2}$  to the second excited state  ${}^4I_{11/2}$  from which it can relax to level  ${}^4I_{13/2}$  through  $\text{Er}^{3+}$  internal recombination channels with a time  $\tau_{32}$ , as reported in [31].

It is worth to note the importance of Auger process in 'recycling' the electrons to high lying Si-np levels, from which they have again the chance to transfer their energy to nearby  $\text{Er}^{3+}$  ions. In this scheme, radiative recombination of population  $N_{exc,2}$  and energy transfer can be seen as indirectly competing mechanisms.

Excitons from the effective trap level cannot recombine radiatively so they are considered totally inactive in terms of VIS-PL emission (this is indicated by a dotted arrow for the relaxation path in fig. 1.11). The existence of this level is necessary to explain the decrease of the whole VIS-PL spectra when erbium is added in the SRSO matrix, as reported in fig. 1.9 (b). In fact, a pure resonant transfer model

---

<sup>2</sup>To have a clearer notation, the relaxation terms have been indicated employing the decay probability ( $w_{ij}$ ) for the Si-np and the lifetimes ( $\tau_{ij} = w_{ij}^{-1}$ ) for the  $\text{Er}^{3+}$  ions.

would imply important differences in the spectral shape of visible emission comparing samples with and without  $\text{Er}^{3+}$ , since depletion of emission should occur at the energy of the resonant levels. The introduction of the effective trap level poses the transfer mechanism (resonant process) competitive with the radiative recombination through Auger effects (non-resonant process), realizing a broad band quenching of the whole visible PL emission. The physical origin of the effective trap level is not clear and still under debate: one reasonable hypothesis is that it can be the analogous of the donor level which is formed in Er-doped bulk silicon [32].

It is worth to note that some other works [15, 20], support the existence of "luminescent centers" (LCs) which are related to the energy transfer mechanism among Si-np and  $\text{Er}^{3+}$  ions. The LC derived transfer scheme is different from the excitonic related one which is discussed in this thesis. Indeed, the observed VIS-PL spectroscopic data strongly differ from the one attributed in literature to LCs. On one side, none luminescent band centered at 550nm, which could be attributed to LC mediated PL [15], has been measured in samples under investigation; on the other side a long PL recombination lifetimes ( $\sim 10 - 40 \mu\text{s}$ ) it is always detected, at odds with the very fast one attributed to LC (tens of ns, as reported in [15, 20]). Moreover, both the PL lifetime shortening (fig. 1.9 (a)) and the reduction of Auger related power-law coefficient (fig. 1.10) when erbium is inserted in the samples point towards an energy transfer process which has to compete, at least indirectly, with the Si-np excitonic radiative recombination. For all these reasons and having not found any evidence of the presence of LCs in the investigated samples, the main role of energy transfer is then attributed to Si-np.

To correctly model the energy transfer it is necessary to understand the physical mechanism behind. Standard theory of sensitization in solid hosts provide three different mechanisms to describe this kind of interaction [27]:

- **Emission-Reabsorption excitation:** this mechanism considers the possibility that the photon emission from an excited sensitizer could be absorbed by the sensitized particle. It is worth to note that this process is less efficient than direct absorption, since it has to take into account the quantum efficiency of sensitizers, which is always less than unity.
- **Förster transfer - dipole-dipole interaction:** the energetic exchange among sensitizers (donor) and sensitized (acceptor) elements is done through coulomb-based dipole-dipole interaction. From classical electromagnetic theory it is possible to determine the transfer probability as a function of the distance  $r$  between the particles as [28]:

$$k_{\text{Förster}} = w_{21} \left( \frac{R_F}{r} \right)^6 \quad (1.8)$$

where  $w_{21}$  is the rate of radiative emission of the sensitizer and  $R_F$  is a parameter of the system under consideration.

- **Dexter transfer - electronic exchange interaction:** the transfer effect is given by an electronic exchange between the partially overlapping donor and acceptor wavefunctions. Due to the evanescent tail of the wavefunction, Dexter energy transfer probability depends on particles distance with an exponential decay law:

$$k_{Dexter} = k_0 e^{-\frac{r}{R_D}} \quad (1.9)$$

where  $k_0$  is the transfer probability on the sensitizer surface, while  $R_D$  is the characteristic interaction distance.

Some important insights can be extracted from the determination of effective absorption cross section ( $\sigma_{eff}$ ) of the process which includes Si-np absorption at 476 nm and energy transfer to nearby  $\text{Er}^{3+}$  ions, which consequently emit at 1535nm ( ${}^4I_{13/2} \rightarrow {}^4I_{15/2}$ ). It is worth again to remember that 476 nm wavelength is not resonant with any  $\text{Er}^{3+}$  internal transitions and the final ions excitation is performed exclusively via energy transfer effect. The rate equation for  $\text{Er}^{3+}$  first excite state in these effective process scheme are given by:

$$\frac{dN_{Er,2}}{dt} = \sigma_{eff} \Phi_{exc} N_{Er,1} - \frac{N_{Er,2}}{\tau_{decay}}, \quad (1.10)$$

where  $\tau_{decay}$  is the total lifetime of the level, which can de-excite both through radiative or non-radiative recombination. Solving the differential equation (1.10), it is possible to combine  $\sigma_{eff}$ ,  $\Phi_{exc}$  and  $\tau_{decay}$  to get the population rise time, which is the time constant needed to reach steady state condition under CW excitation ( $\tau_{rise} = \tau_{decay} + (\sigma_{eff} \Phi_{exc})^{-1}$ ). Then,  $\sigma_{eff}$  can be extracted by a time-resolved measurement of the rise and decay time of 1535 nm signal, in a non-saturation excitation regime, as:

$$\sigma_{eff} \Phi_{exc} = \frac{1}{\tau_{rise}} - \frac{1}{\tau_{decay}}, \quad (1.11)$$

where  $\tau_{rise}$  ( $\tau_{decay}$ ) is the single exponential growth (decay) characteristic time of the signal [4]. Fig. 1.12 (a) reports the TR measurements for different excitation fluxes at 476 nm in sample A. The excitation has been performed modulating the laser beam through a mechanical chopper (dashed curve in fig. 1.12 (a)). The resolution of the measurements was of tens of microseconds, while the modulation frequency ( $\sim 10$  Hz) has been chosen to guarantee the attainment of steady-state condition. The extracted effective cross section is portrayed in fig. 1.12 (b). The most striking feature is the enhancement of  $\text{Er}^{3+}$  effective cross section with respect to the non-sensitized material ( $\sigma_{direct} \sim 10^{-21}$  cm<sup>2</sup>) [29]. This fact rules out the Emission-Reabsorption sensitization mechanism as the main energy transfer channel in the sample. Since  $k(r)$  is a decreasing function of the distance among Si-np and  $\text{Er}^{3+}$  ions in both Förster and Dexter mechanisms, it is expected that the transfer efficiency, which is proportional to  $\sigma_{eff}$ , showed the same monotonic decrease with the interaction distance. It is worth to note that an increase of the excitation photon flux can be correlated to the reaching of  $\text{Er}^{3+}$  ions placed farther from the Si-np surface. This poses the value of  $\Phi_{eff}$  directly proportional to the distance from Si-np at

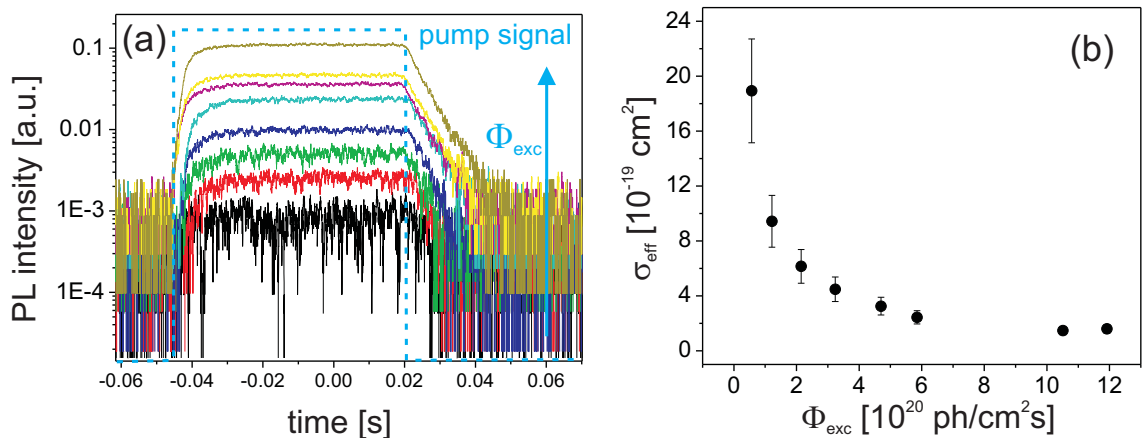


Figure 1.12: (a): TR-PL signal at 1535nm for sample A when excited at different pump fluxes ( $\lambda_{exc}=476\text{nm}$ ). (b) Effective cross section  $\sigma_{eff}$  extracted from the result.

which  $\text{Er}^{3+}$  ions can be possibly excited. From fig.1.12 (b), it can be seen that  $\sigma_{eff}$  is a decreasing function of the photon flux, confirming the hypothesis that Förster and/or Dexter mechanisms are the main responsible for the sensitization effect.

Both transfer mechanism probabilities are inversely proportional to the interaction distance; one can safely assume that the first ions to be excited are the ones closer to the Si-np surface. When all these are saturated, the energy transfer acts on the ions which are placed in regions slightly more distant from the nanoparticle. It is indeed natural to model the interaction considering shell-shaped regions in which it is possible to assume the  $\text{Er}^{3+}$  ions at a fixed distance from the nanoparticle, and thus with the same probability to be excited during the transfer process. Combining the results of fig. 1.12 (b) with quantitative measurements of the coupled  $\text{Er}^{3+}$  ions (which will be described in sec. 1.3.1) and with the known total ion concentrations in the samples (see tab. 1.1), it is possible to express  $\sigma_{eff}$  as a function of the Si-np to  $\text{Er}^{3+}$  ions distance [30, 44]. The obtained data can then be well fitted using an exponential decay curve, which suggests the existence of a dominating Dexter transfer mechanism in the sample. From the fit it is possible to extract  $R_D$ , which has been found to be in a range between 0.5 to 1 nm [30, 44]. The same results have been found in multilayer samples made of similar materials. In this configuration, it is possible to precisely control  $\text{Er}^{3+}$  to Si-np distance during material deposition [33]. This result further confirms the Dexter transfer hypothesis.

The probability that a transfer occurs, as reported in eq. (1.7), is proportional to the coupling constant  $k$ , which itself is strongly dependent from the distance between  $\text{Er}^{3+}$  ions and Si-np. A shell-model has then been considered, under the assumptions of spherical nanoparticles surrounded by an homogeneous distribution of  $\text{Er}^{3+}$  ions. For a fixed distance between the Si nanoparticle and  $\text{Er}^{3+}$ ,  $r_i$ , an interaction shell has been defined, characterized by a coupling constant  $k_i$ , which depends on the distance according to:

$$k_i = k_0 e^{-\frac{r_i - R_{Si-np}}{R_{int}}}, \quad (1.12)$$

where  $k_0$  represents the maximum coupling constant value, when the ion is placed exactly on the Si-np surface and  $R_{Si-np}$  is the Si-np radius. Clearly, this simple model can be applied reliably only for Er-Si-np distances smaller than some nanometers, where it is possible to consider interaction among only one *single* Si-np and many  $Er^{3+}$  ions.

The high pumping fluxes used in the TR-PL experiments lead to a regime in which multi-excitons have been created inside the nanoparticles (this is confirmed by the power-law fits in fig. 1.10). In fact, the maxima of the curves reported in fig. 1.14 correspond to a local excitonic density of about  $1 - 2 \times 10^{20} \text{cm}^{-3}$  ( $\sim 4$ -5 excitons within the nanoparticle, where an average nanoparticle size of 4 nm diameter has been assumed). In this situation, which lasts for few nanoseconds before relaxing to single-exciton regime, it is possible to correlate the PL intensity with the square of the Si-np electronic population which can be obtained from numerical solutions of eq. (1.7) [24]. Even as a rough approximation, it is interesting to try

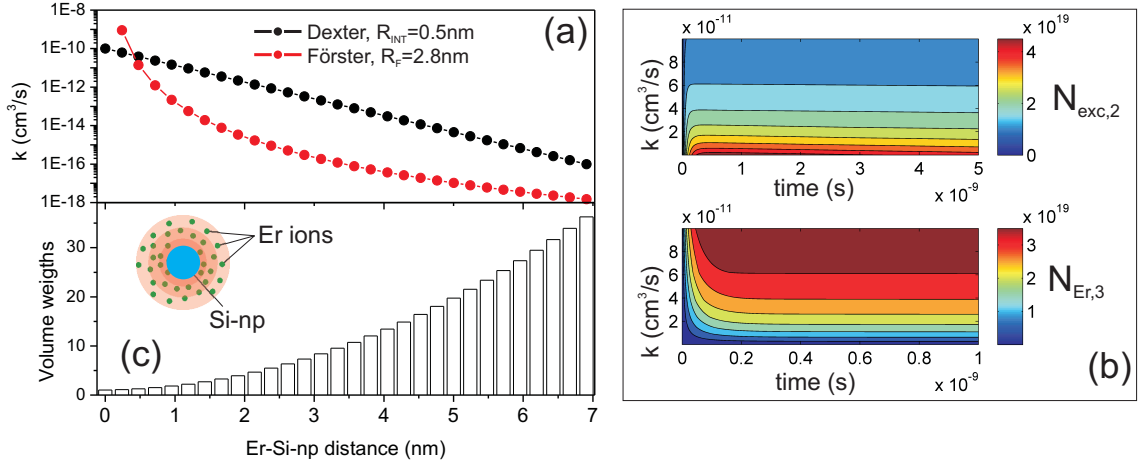


Figure 1.13: (a): Dexter transfer probability  $k$  and volume weight  $V_i$  with which sample A decay of fig. 1.14 has been fitted. For the same distances, the transfer probability of Förster sensitization is reported for comparison. (b): Simulated decay curves of respectively  $N_{Er,3}$  and  $N_{Exc,2}$  for an initial fixed exciton population  $N_{exc,3}(t=0) = N_0$  for different transfer probabilities. Note that while for the largest  $k$  values  $N_{exc,2}$  population is totally depleted, quenching the VIS-PL and the transfer is almost immediate, for the smallest  $k$  a residual population can be appreciated, together with a slower transfer time.

to evaluate the average distance among neighboring Si-np, which can be calculated considering a homogeneous distribution of spherical particles with a concentration of  $1 \times 10^{19} \text{cm}^{-3}$ . Indeed, an average distance of 6 nm has been found, which can be easily compared with the maximum interaction distance used in the simulation of 7 nm (see the following discussion). It is important to stress out that, due to the low annealing temperature, the investigated Si-np likely possess a non-spherical shape with a corresponding non-homogeneous distribution: nevertheless, it is reasonable to expect that the average interparticle distances are of the same order of magnitude of the ideal case and quite in agreement with the simulated ones.

The procedure used for the fit of experimental data is based on the assumption that,

apart from the transfer, the recombination dynamics of Si-np is not affected by the presence of erbium. Thus the luminescence decay for the sample without  $\text{Er}^{3+}$  (sample B) has been initially fitted with the constraint  $k = 0$ . In this way it is possible to determine the parameters  $w_{ij}$  and  $C_A$ . Then, the transfer process is considered by using these values as starting guesses for the Si-np recombination dynamics, while sample A decay curve has been fitted to determine the transfer properties.  $\text{Er}^{3+}$  recombination parameters ( $\tau_{32}$  and  $\tau_{21}$ ) have been taken from experimental data and are equal respectively to  $4.2\mu\text{s}$  and  $5.5\text{ms}$ . To take into account the distance dependent coupling constant, a sum-up weighted average of the solutions at each interaction distance is evaluated. To this end, the  $i^{\text{th}}$ -shell which is distant  $r_i$  from the Si-np, and thus characterized by a coupling constant  $k_i$  has been considered. To take into account the different numbers of  $\text{Er}^{3+}$  ions in shells of different volumes, the solutions  $N_{exc,2}^i(t)$  for each shell  $i$  have been weighted:

$$N_{exc,2}^{tot}(t) = \frac{\sum_{i=1} N_i \cdot V_i}{\sum V_i}, \quad (1.13)$$

to yield the value  $N_{exc,2}^{tot}(t)$ . The weight  $V_i$  represents the different number of ions accessible for different Er-Si-np distances (different shell volumes, proportional to  $r_{i+1}^3 - r_i^3$ ).

The values of coupling constants  $k_i$  which fit the experimental decay curve of sample A in a 140 ns time window are reported in fig. 1.13 (a) (black circles), as a function of Er-Si-np distances  $r_i$  ( $k_i = [0.1 \times 10^{-16} - 0.8 \times 10^{-10}] \text{ cm}^3/\text{s}$ ). The interaction distance corresponding to the lowest  $k_i$  is equal to about 7 nm. In the same figure the  $V_i$  values estimated for this specific case are reported. As additional information, fig. 1.13 (a) reports the expected coupling constants of a Förster-type transfer process ( $k_F$ ) for the same interaction distances and initial exciton populations. The value has been calculated with the formula [28],  $N_{exc}k_F = w_{21} (R_F/r)^6$ , where the parameter  $R_F$  has been taken from known values for similar rare earth elements [34]. It is clear that in the model the ions placed at moderately far distance from the sensitizer (from 0.5 nm to 5 nm) play a fundamental role in the energy transfer mechanism. Even if for the shortest  $\text{Er}^{3+}$  to Si-np distances the Förster mechanism dominates over the Dexter one in the intermediate and long ranges, Dexter transfer probability is at least two orders of magnitude larger than the Förster one, making the latter negligible. To clarify the shell effect in the population dynamics, fig. 1.13 (b) reports the first nanosecond time slot of decay curves of population  $N_{exc,2}$  and  $N_{Er,3}$  for an initial, fixed exciton population  $N_{exc,3}^0$ . In the y-axis the different interaction shells (whose transfer constants and volume weights are in fig. 1.13 (a)) are considered. For the largest  $k_i$  values, the population  $N_{exc,2}$  is depleted while a sharp rise can be observed for the  $N_{Er,3}$  population. On the other hand, a slow rise in  $N_{Er,3}$  population and a residual  $N_{exc,2}$  population for the lowest  $k_i$  values can be appreciated.

Figure 1.14 reports the final results of the fits. The intraband recombination probability has been found to be  $w_{32} = 1 \pm 2 \times 10^{10} \text{ s}^{-1}$ , while the Auger coefficient

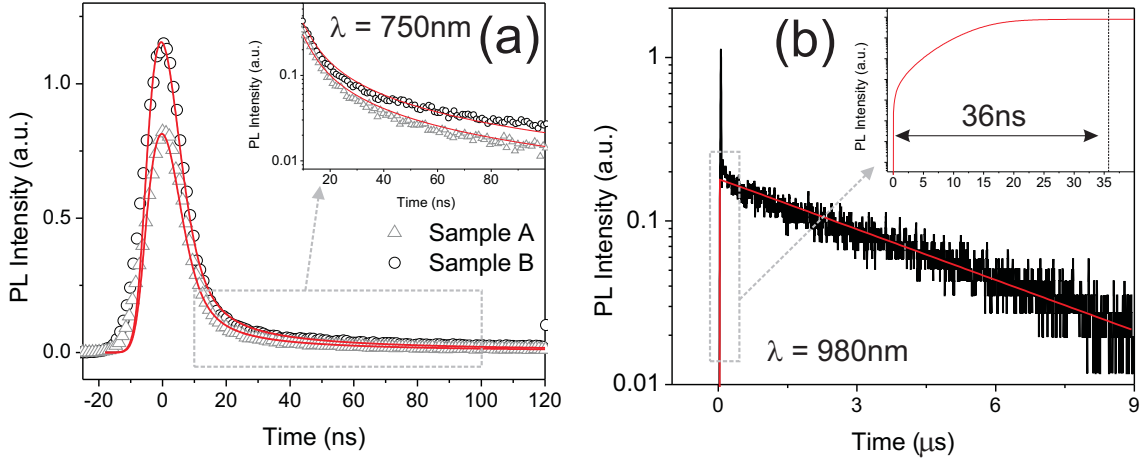


Figure 1.14: (a): Comparison of experimental and simulated decays for sample A and B. The parameter used to fit the experimental data are discussed and reported in the text. (b): Fit of  ${}^4I_{11/2}$  experimental decay. From the fit a transfer time of 36.6 ns can be extracted.

$C_A = 2 \pm 3 \times 10^{-32} \text{cm}^6/\text{s}$ . Even with this simple model, the numerical results reproduce qualitatively the experimental data, being the correlation coefficient of the fitting,  $R^2$ , of 0.99 for both samples A and B decays. This model allows to explain most of the experimental data such as the reduction of the whole Si-np emission band or the lifetime shortening of the PL visible emission, when  $\text{Er}^{3+}$  is inserted in the samples. This last phenomenon can be understood by the role of Auger processes. The energy transfer becomes an indirect competing mechanism with the radiative recombination of the level Ex2, due to Auger carrier "recycling" from level Ex2 to level Ex3. Excitons in this last level can eventually relax very fast in the effective trap level, exciting an  $\text{Er}^{3+}$  ion without relaxing again to the level Ex2, contributing to a fast level depletion mechanism. Without changing any parameter it is possible to fit the  ${}^4I_{11/2}$  decay, as reported in fig. 1.14 (b). Apart from the fast lineshape which is unrelated to the transfer model, a good fit of the experimental data is obtained, from which a transfer time of 36.6 ns can be extracted. Concluding, it was found also that, while the fit parameters  $C_A$  and  $k$  are strongly dependent from the number of excitons within the nanocrystal after the laser excitation, the transfer time itself has revealed to be quite robust with respect to different initial conditions, such as different Si-np diameters or average concentrations. In tab. 1.2 the transfer time found is compared with the ones of other models proposed in literature. As discussed, the model here presented is qualitatively similar to the one presented in [15], yet different in attributing the role of sensitizers to Si-np instead of LCs. Moreover, a single kind of transfer mechanism is proposed. On the other hand, the absence of Auger back-transfer, key feature of the model proposed in [14], completely rules out the possibility to use that model to interpret the physics of the samples here investigated.

With the validation of the model proposed, it has been verified that the system under investigation lacks any intrinsic limit, with absence of Auger back-transfer. The only limit to achieve a full sensitization is indeed represented by the distance-

|           | Transfer time                    | Role of sensitizer  |
|-----------|----------------------------------|---------------------|
| This work | <100 ns (exp) $\sim$ 40 ns (sim) | Si-np               |
| Ref. [15] | < 80 ns                          | Luminescent centers |
|           | 4 - 100 $\mu$ s                  | Si-np               |
| Ref. [14] | $\sim$ ns                        | Si-np               |
|           | 1 - 5 $\mu$ s                    | Si-np               |

Table 1.2: Comparison of average energy transfer time and mechanisms for the different models proposed in the literature.

dependent interaction. While it is not possible to increase more the number of  $\text{Er}^{3+}$  ions in the material to avoid clusterization effects, the possibility to place all the ions in close proximity to the Si-np becomes an essential technological issue to be addressed.

### 1.3 Quantitative optical characterization of waveguide amplifiers

A definitive proof of the feasibility of the model developed in the last section is the quantification of the fraction of coupled  $\text{Er}^{3+}$ , that is the number of ions that can be excited by a nearby nanoparticle. In fact, if the distance-dependent interaction is the main (if not only) limit to achieve a fully sensitized system, it should be possible to get a large number of coupled ions in sample where many, small nanocrystals are homogeneously distributed. By means of quantitative PL experiments, the largest concentration of active  $\text{Er}^{3+}$  ions coupled to Si-np reported so far in the literature has been found ( $\sim$  56%) [16]. Unfortunately, the investigation of PL is not enough to address the topic of optical amplification in waveguide systems. Some additional factors have to be taken into account when the signal propagation and amplification in dielectric waveguides are investigated: detrimental effect such as Confined Carrier Absorption and the fact the some  $\text{Er}^{3+}$  ions are not optically active<sup>3</sup>, heavily influences the signal propagation and make the reach of net gain in the system a though task, which has still to be solved.

In the next section, I will report quantitative experiments where the concentration of optically active and Si-np-coupled  $\text{Er}^{3+}$  ions are evaluated. Since sample A represents a good candidate for obtaining optical amplification, I will show the optical characterization experiments in waveguide samples where the active material has been obtained with the same recipe of sample A. In the first stage, slab waveguides, in which light undergoes a planar confinement, are used to asses material amplification and losses by means of dedicated experiments, such as Shift of Excitation Spot (SES) and Variable Stripe Length (VSL) technique. Experiments in slab waveguide does not allow a reliable estimation of amplification/losses in material with a small oscillator strength (small gain coefficient); a more detailed analysis can be performed

---

<sup>3</sup>An ion is considered optically active if it is capable to absorb and re-emit light. Conversely an optical inactive ion is assumed to neither absorb or emit light.

in channel-waveguide amplifiers, where the light is confined in small spatial regions and can be precisely controlled and measured. A brief discussion of the main detrimental effect in such configuration, that is Confined Carrier Absorption mechanism, is finally reported.

### 1.3.1 Quantitative photoluminescence analysis: coupled and active $\text{Er}^{3+}$ fraction

Quantification of coupled and optically active  $\text{Er}^{3+}$  ions has been performed analyzing PL emission in different excitation conditions. Even if this procedure has been applied to different samples, for the sake of discussion I will report the experiments which deals with sample A (see tab. 1.1), which has been widely investigated in sec. 1.2.

Essentially, the experiment concerns a comparison between PL spectra of sample A and reference sample C, of which all the optical constants are well known. This technique reveals to be much more reliable with respect to different estimations in which the PL spectra under non-resonant (476nm) and resonant (488nm) excitation were considered. In this last method, assuming a negligible change of  $\text{Er}^{3+}$  effective absorption cross section at 476 and 488nm, any modification of PL intensity ( $\Delta I_{PL} = I_{PL}(488) - I_{PL}(476)$ ) is attributed to the direct excitation of  $\text{Er}^{3+}$  ions, as reported in the following:

$$\Delta I_{PL} = I_{PL}^{ind}(488) + I_{PL}^{dir}(488) - I_{PL}^{ind}(476) \sim \sigma_{dir}(488)\tau_{PL}\Phi_{exc}N_{Er,2} \quad (1.14)$$

where the superscript *dir.* and *ind.* indicates, respectively direct and indirect excitations,  $\sigma_{dir}$  is  $\text{Er}^{3+}$  direct absorption cross-section and the number in the round brackets represents the excitation wavelength. The problem with this method lies in the huge difference between the indirect and direct process cross sections. The expected PL modification due to directly excited  $\text{Er}^{3+}$  ions is of the order of 0.01 - 0.001%. Such small values, apart being at the limit of detection in room temperature experiments, are of the same order of magnitude of the expected modification of Si-np cross sections at the two different excitation wavelengths. Indeed, this cancels the initial assumption which has been done, nullifying the validity of the technique.

In principle, the estimation of optically active  $\text{Er}^{3+}$  can be alternatively performed by absorption measurements. However, in this case an exact value of  $\text{Er}^{3+}$  absorption cross section in SRSO is required, since the technique allows one to obtain the product  $\sigma_{dir}N_{Er}$ , being the latter the active ions concentration.  $\text{Er}^{3+}$  optical transitions are controlled by the host crystal field (as explained in sec. 1.1), and a modification of  $\sigma_{dir}$  is expected in SRSO material with respect to pure  $\text{SiO}_2$ . Only if  $\sigma_{dir}$  can be determined with different means, the technique sounds suitable for the determination of active ions.

It would be interesting to compare the optically active ions estimation obtained with PL-related and absorption related experiments. A real interesting possibility concerns the fact that some of the  $\text{Er}^{3+}$  ions could absorb light and recombining non-radiatively, being totally quenched in terms of PL emission. This particular

ions could be considered "half-active" and could redraw the picture of optical amplification in the system. Since this is only a theoretical hypothesis, in this thesis only the possibilities of fully-active or de-active ions have been considered.

### Er<sup>3+</sup> ions concentration coupled to Si-np

At first, the optically active Er<sup>3+</sup> ion fraction which is coupled to Si-np has been determined. Using sample C as a reference, the measured emitted photon flux ( $\Phi_{emitt}$ ) can be expressed as a function of Er<sup>3+</sup> excited population  $N_{Er,2}$ , created employing a resonant excitation ( $\Phi_{exc}$ ), by the formula:

$$\Phi_{emitt} = \frac{V}{\tau_{rad}} N_{Er,2}, \text{ with } N_{Er,2} = \sigma_{dir}(488) \Phi_{exc} \tau_{PL} N_{Er}, \quad (1.15)$$

where  $V$  is the excited sample volume and  $N_{Er}$  is total ions concentration. In Corning glass doped Er<sup>3+</sup> material (sample C), all Er<sup>3+</sup> ions are considered optically active. PL lifetime ( $\tau_{PL} = 7.7$  ms), radiative lifetime ( $\tau_{rad} = 18$  ms) and absorption cross section ( $\sigma_{dir}(488) = 2 \times 10^{-21}$  cm<sup>2</sup>) have been measured or taken from the literature [29]. Once the system has been calibrated using sample C, PL intensity of sample A has been measured for different excitation fluxes at non-resonant wavelength (476 nm) and then the number of Er<sup>3+</sup> ions involved in the emission process has been evaluated. It is possible to relate this value to the number of coupled ions ( $N_{coupl}$ ), using standard rate equations, as:

$$N_{Er,2} = N_{coupl} \frac{\sigma_{eff} \Phi_{exc}}{\sigma_{eff} \Phi_{exc} + \tau_{PL}^{-1}} \quad (1.16)$$

where  $\tau_{PL}$  has been directly measured and found equal to 5.5 ms.  $\sigma_{eff}$  has been estimated employing eq. (1.11), where the difference  $1/\tau_{rise} - 1/\tau_{decay}$  was evaluated. Both results are shown in 1.15 (a). Figure 1.15 (b) reports the final results for  $N_{Er,2}$  determination. With the sigmoidal fit of eq. (1.16) a number of  $3.6 \pm 1 \times 10^{19}$  cm<sup>-3</sup>

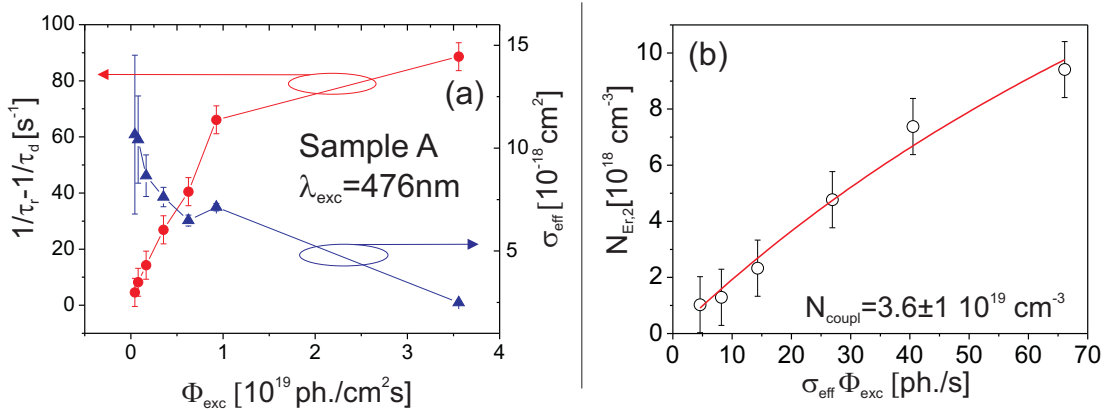


Figure 1.15: (a): Difference of the rise and decay time inverse and effective cross section in sample A. (b): Excited Er<sup>3+</sup> population as a function the resonant pump photon flux (476nm) times the effective cross section in sample A. From the sigmoidal fit (1.16) the coupled Er<sup>3+</sup> concentration is obtained.

coupled  $\text{Er}^{3+}$  ions has been found, which is roughly 11% of the total  $\text{Er}^{3+}$  concentration reported in tab. 1.1.

### Optically active $\text{Er}^{3+}$ ions concentration

The coupled ions estimation gains significance only when compared with the number of active ions in the sample. The experiments regarding the determination of the latter are very similar to the ones reported above: even in this case the PL detected signal has been correlated with the number of excited ions ( $N_{Er,2}$ ) in the system. When the material is excited at 980 nm it is assumed that the Si-np has a negligible role in the absorption-emission processes, which can be totally imputed to the presence of  $\text{Er}^{3+}$  in the material. The number of excited  $\text{Er}^{3+}$  ions has been evaluated with the following formula both for reference sample C and sample A:

$$\Phi_{emitt} = \frac{V}{\tau_{rad}} N_{Er,2}, \text{ where } N_{Er,2} = \sigma_{dir}(980) \Phi_{exc} \tau_{PL} N_{Er} \quad (1.17)$$

where the notation used is the same of eq. (1.15). As before, the direct absorption cross section value for sample C ( $\sigma_{dir}(980) = 1.02 \times 10^{-21} \text{ cm}^2$ ) has been taken from the literature [29]. Using the results of sample C as a calibration constant of the system, eq. (1.17) has been inverted to obtain  $N_{Er}$  in sample A. In this case,  $\tau_{rad}$  has been evaluated considering the relative refractive index change in the material with respect to pure  $\text{SiO}_2$ , while  $\sigma_{dir}(980)$  has been determined employing eq. (1.11) in a dedicated micro-PL experiments and have been found to be equals to  $9.0 \pm 1.5 \times 10^{-21} \text{ cm}^2$  [16].

Figure 1.16 (a) reports the PL spectra as a function of increasing excitation photon flux, from which the values of  $N_{Er,2}$ , reported in panel (b), can be extracted employing the procedure just described. From eq. (1.17), it is possible to extract  $N_{Er}$

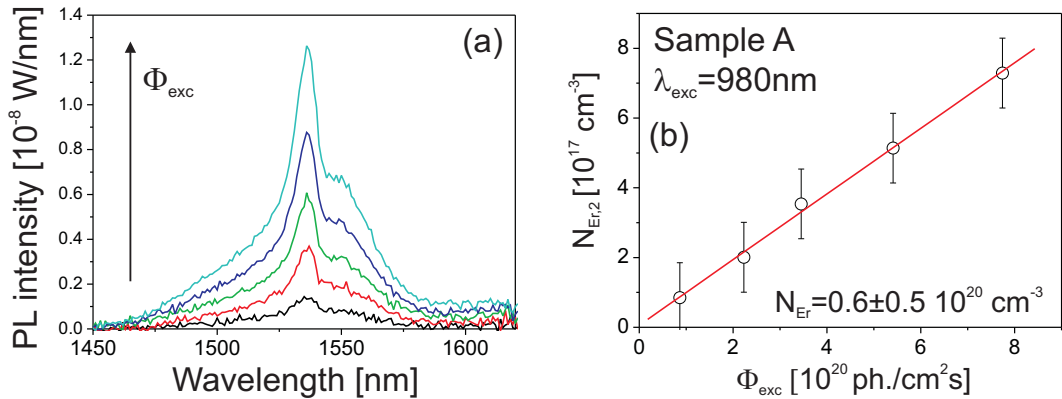


Figure 1.16: (a): PL spectra for different excitation photon fluxes at resonant wavelength (980nm). (b): Excited  $\text{Er}^{3+}$  population as a function the resonant pump photon flux (980nm) in sample A. From the slope of the linear fit of the data the optically active  $\text{Er}^{3+}$  concentration is obtained.

from the linear fit slope of the experimental results. The value found,  $0.6 \pm 0.5 \times 10^{20} \text{ cm}^{-3}$ , roughly corresponds to 19% of the total  $\text{Er}^{3+}$  concentration reported in tab.

1.1. Different samples have produced similar results, with a maximum active concentration of 25 - 30%.

Indeed, it would be interesting to understand the role of de-active ions. As briefly discussed, if they are not-active both in terms of absorption and emission, they can be safely neglected since do not contribute to the system optical amplification nor losses. On the other hand, if they should be able to absorb and relax without any radiative recombination, the low percentage of optically active ions in these systems should be the first issue to be addressed to improve the overall amplifier performance. Additional studies to understand this issue are ongoing, while in this work the de-activated ions are merely considered as background terms which do not contribute to amplifier optical characterization.

Finally, it is worth to note that the evaluated fraction of coupled  $\text{Er}^{3+}$  ions (11% of the total  $\text{Er}^{3+}$  concentration) has to be reconsidered in terms of the optically active value which has been just reported (19% of the total  $\text{Er}^{3+}$  concentration). In this sense, a 56% of erbium ions which emit light are coupled to the Si-np, i.e. can be excited through non-resonant pumping sensitization processes. This is at least one order of magnitude larger with respect to the best values of coupled ions reported in the literature ( $\sim 3\%$ ) [30]. The hypothesis that, at least in the samples under investigation, no intrinsic limit in achieving the full sensitization of the ions, such as Auger back-transfer, is present is thus confirmed.

### 1.3.2 Enhancement and losses in slab and channel waveguides

To get a working amplifier device it is necessary to insert the active material in dielectric waveguide structures, where the propagation of light can be controlled and addressed. Entering too much into the details of light guiding in dielectric waveguides is out of the scope of this thesis, whereas full details can be eventually found in many textbooks (see, for example, [36]). Thus, a more intuitive approach to the problem of photon localization in such structures is presented, considering the theoretical framework of the well-known quantum-mechanical Schrödinger equation for a particle in a potential well.

For the sake of discussion, consider the one-dimensional potential well problem along the  $\hat{y}$  direction: with some basic algebra, starting from the Maxwell equation and considering a time-harmonic dependence of the electric field, it is possible to write an eigenvalue equation for the electric field with the same mathematical structure as the Schrödinger one (Helmholtz equation):

$$\begin{aligned} \left[ -\frac{\hbar^2}{2m} \frac{\partial^2}{\partial y^2} + V(y) \right] \Psi(y) &= \eta \Psi(y) && \text{Schrödinger equation,} \\ \left[ \frac{1}{k^2} \frac{\partial^2}{\partial y^2} + \epsilon(y) \right] E_x(y) &= \frac{\beta^2}{k^2} E_x(y) && \text{Helmholtz equation,} \end{aligned} \tag{1.18}$$

whereas similar equations can be obtained for the different field components. In the electromagnetic case, the potential profile  $V(y)$  is substituted by a scalar potential which depends on the material dielectric constant  $\epsilon = n^2$ , where  $n$  is the material refractive index. In this sense, a high refractive index material (of index  $n_H$ ) sandwiched between low refractive index media (of index  $n_L$ ) acts exactly as a 1-D potential well in quantum mechanics. It is then expected that the eigenfunctions of the system were  $L^2$  functions with an increasing number of nodes from the fundamental state (no nodes). The eigenvalues of eq. (1.18) are called propagation constants of the mode ( $\beta$ ). It is instructing to define a mode effective index as  $n_{eff}^2 = k^2/\beta^2$ , with  $k$  light wavenumber. In order to have a  $L^2$  wavefunction, which is a guided mode in the system, the following condition on  $n_{eff}$  should hold:

$$n_L^2 < n_{eff}^2 \leq n_H^2; \quad (1.19)$$

if the left hand side of this equation is not verified, then the light can not propagate by means of total internal reflection into the waveguide.

In a more detailed analysis concerning a closer inspection of Maxwell's equations, more differences between the solutions of Schrödinger and Helmholtz equations can be appreciated. In particular, for the problem here discussed, it is possible to consider two basis in which a general electromagnetic wave can be decomposed, with reference to the coordinate system reported in fig. 1.17:

$$\{E_x, H_y, E_z\} \rightarrow \text{TE polarization} \quad (1.20)$$

$$\{H_x, E_y, H_z\} \rightarrow \text{TM polarization.} \quad (1.21)$$

The boundary condition of the fields at the dielectric interface has to be coherent with the electromagnetic theory: considering only the electric fields for TE and TM polarization,  $E_x$  and  $E_y$ , from which all the other components can be derived, the following conditions should be verified at the interface along the  $\hat{x}$  direction between a low and high refractive index material:

$$E_x^L = E_x^H \quad (1.22)$$

$$E_y^L = \left(\frac{n_H}{n_L}\right)^2 E_y^H, \quad (1.23)$$

where the subscripts  $H$  and  $L$  indicate, respectively, the field in the high and low refractive index material. Figure 1.17 reports, as an example, the field eigenfunction solutions of Helmholtz equation (1.18) for a 500nm thick Si-slab waveguide ( $n_H = 3.5$ ) surrounded by air ( $n_L = 1$ ) at a wavelength of 1500 nm. Three TE modes (panel (a)) are supported and, as expected, they have respectively zero (fundamental mode), one (first excited state) and two nodes (second excited state). On the other hand (panel (b)), only two TM modes are supported. Note that the field amplitude are independently normalized.

The situation becomes more complicated when the dimensionality of the waveguide is increased. Helmholtz's equation in 3D dielectric systems has no analytical

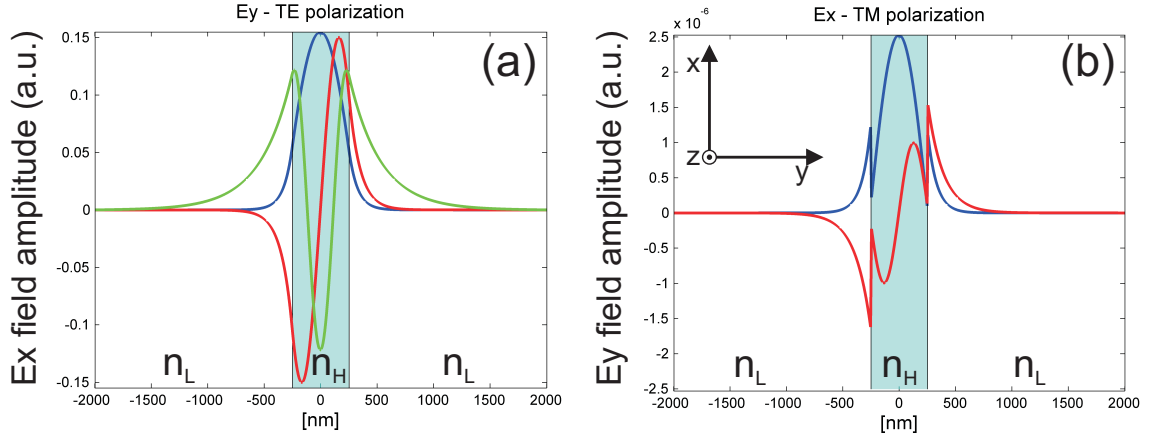


Figure 1.17: (a): Electric field amplitude for TE polarization eigenfunctions in 500nm Si-slab surrounded by air at a wavelength of 1500nm. Note the number of increasing nodes from fundamental (blue) to higher order solutions (red, 2<sup>nd</sup> order and green, 3<sup>rd</sup> order). (b): Same results for TM polarization. Note the discontinuity at the slab border.

solution and guided modes can not be expressed in the TE-TM polarization basis anymore. Nevertheless, in many cases it is still possible to define a *majority* triplet of field components among the ones of eq. (1.20) and (1.21). Even if the guided modes are not purely polarized, they are called quasi-TE (quasi-TM) if the dominant field components are the one of eq. (1.20) ((1.21)). In 3D waveguides, solutions of eq. (1.18) can be obtained using numerical algorithms, such as the effective index method [36] or wave-matching-mode method [37].

For practical purposes, it is worth to show some of the light-guiding properties of the SRSO:Er waveguides which will be investigated in the following sections. Figure 1.18 summarizes the dispersion relation of both slab (panel (a)) and channel waveguides (panel (b), (c) and (d)). The slab waveguide is composed by a 1.2  $\mu\text{m}$  active layer of SRSO:Er composite material (refractive index  $n \sim 1.52 - 1.58$  at 1500nm) deposited on a 5  $\mu\text{m}$  thick silicon oxide cladding layer. The TE and TM mode effective indices are reported in fig. 1.18 (a). These waveguides have been investigated to check the reproducibility and homogeneity of the deposition technique by m-line measurements [18]. Moreover, the losses and amplification properties of the material have been addressed, respectively, employing Shifting of the Excitation Spot (SES) [38] and Variable Stripe Length (VSL) [39] techniques, which will be described in next section.

Rib-channel waveguide is the configuration chosen for the final amplifier device. In fig. 1.18 (b) the dispersion relation, for a typical 5  $\mu\text{m}$  wide waveguide (of which a schematic is reported in fig.1.18, (d)), is reported. The gray-shaded zones represent regions in which the optical modes can not propagate, as shown by eq. (1.19). Noteworthy, the number of optical modes increases with the photon frequency. The fundamental and first excited quasi-TE modes, can be better inspected in fig.1.18 (c), in the spectral region of interest for  $\text{Er}^{3+}$  emission. Finally, fig. 1.18 (d) reports the electric field amplitude of the first guided TE-mode at a wavelength of 1.55  $\mu\text{m}$ . A particularly useful parameter, in this context, is the fraction of optical

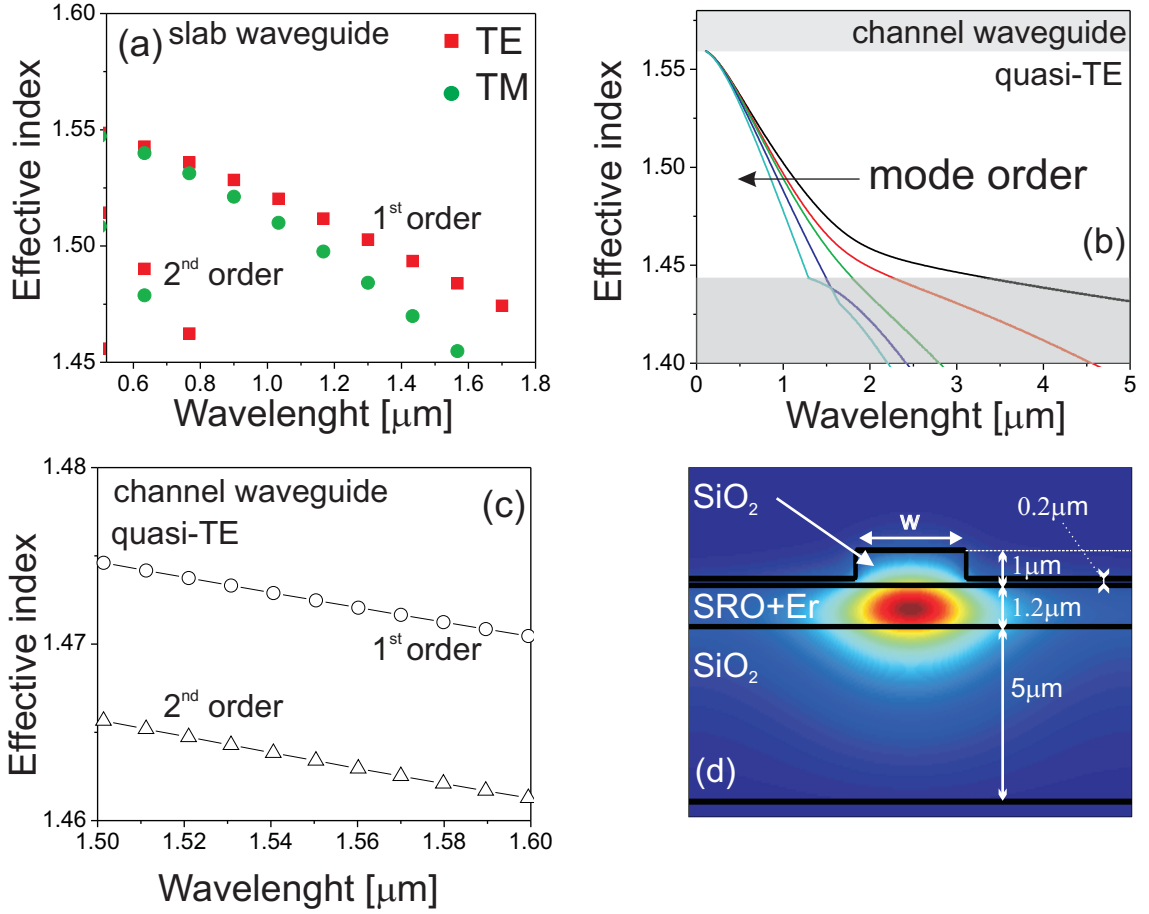


Figure 1.18: (a): Effective index for the Er:SRSO slab waveguide under study (structure details in text). (b): Dispersion relation ( $n_{eff}(\lambda)$ ) for rib-channel waveguides under study (structure details in the text). (c): Effective indices of the fundamental and first excited quasi-TE modes in the  $\text{Er}^{3+}$  emission spectral region. (d): Electric field amplitude of the fundamental quasi-TE mode at a wavelength of 1550 nm. Some geometrical parameters of the waveguide are added for completeness.

power which is localized in the active material (confinement factor  $\Gamma$ ), which can be obtained evaluating the following integrals:

$$\Gamma = \frac{\int_{AL} \Re(\vec{P}_z(\vec{r})) d\vec{r}}{\int_V \Re(\vec{P}_z(\vec{r})) d\vec{r}}, \quad (1.24)$$

where  $\vec{P}_z$  is the Poynting vector ( $\vec{P}_z = \vec{E} \times \vec{H}$ ) and the integration domains are over the active layer (AL) and in the whole space (V). While slab waveguides hold an average confinement factor of 0.85, this reaches an average value of 0.7 in channel waveguides, where a range of channel widths from 5 to 10  $\mu\text{m}$  has been considered. Channel waveguides have been at first passively characterized employing transmission cut-back measurements. Active characterization has been carried out by means of pump & probe experiments. Both measurements will be detailed in next sections.

## Amplification and losses in slab waveguides

Active slab waveguides optical characterization can be performed employing particular experimental techniques. In these, spontaneous emission is exploited to probe the light-guiding properties of the dielectric. A brief schematic of both SES and

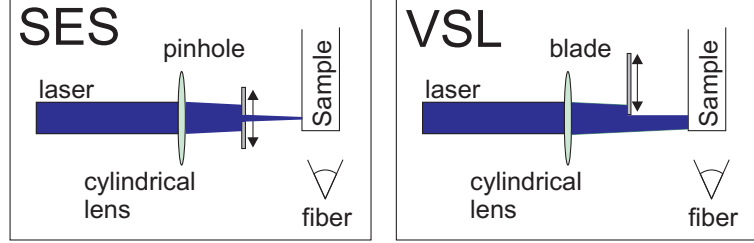


Figure 1.19: Schematics of SES and VSL experiments.

VSL experimental setups is depicted in fig. 1.19. In SES, the excitation source is focused in a small spot which can be moved at different distances from the sample edge. Since the material under investigation is active, the excited region emits light itself, which is then collected from the sample edge with an optical fiber bunch and analyzed with a monochromator coupled to a IR-PMT. In practice, a movable, isotropic, light emitting source is realized. It is a well known fact that the light intensity which propagates in a dielectric waveguide of length  $L$  follows the Beer's law [36]:

$$I(L) = I_0 e^{-\alpha \Gamma L} \quad (1.25)$$

where  $I(L)$  ( $I_0$ ) is the intensity at the edge (input) of the waveguide,  $\Gamma$  is the optical confinement factor and  $\alpha$  is the loss coefficient, which gathers the information about all the possible loss channels within the guiding structure. By translating the pinhole

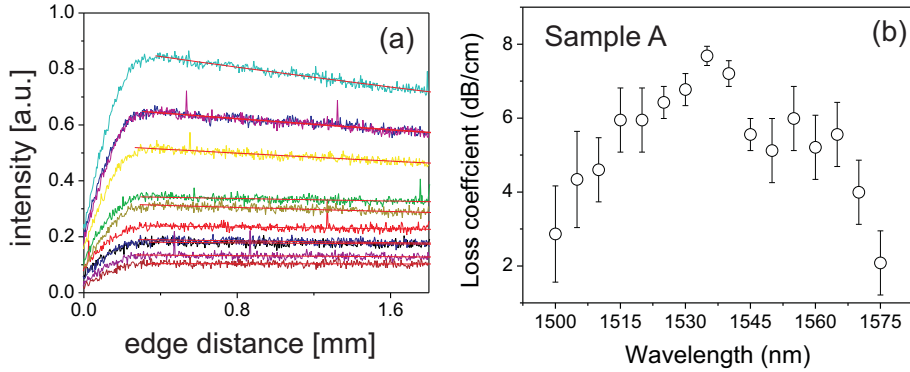


Figure 1.20: (a): Results of SES measurements of sample A (see tab. 1.1). A CW excitation source was used at a wavelength of 488nm.

position, the excitation spot is moved at different distances  $L$  from the sample edge. Then,  $\alpha$  can be determined by fitting the collected signal as a function of  $L$ . Figure 1.20 (a) reports typical signals collected from the sample edge, while in panel (b) the results extracted from the fits for sample A are shown. Here, a 488 nm excitation wavelength has been employed. It is worth to point out that the results have been

corrected to take into account the gaussian-shaped intensity of the excitation laser beam.

In SES experiments, only a finite percentage of optical radiation (which value depends from the spot-sample edge distance) can be collected by the fiber. This causes a slight overestimation of the real material losses. Nevertheless, the results clearly depict  $\text{Er}^{3+}$  absorption spectrum, showing a peak of losses at 1535nm. Neglecting absorption effects, propagation losses (that is, all the other losses contribution which depends on waveguide length) as low as 2 dB/cm have been found, considering the longest wavelength result obtained at 1575nm. Similar results have been found in most of the samples under analysis.

In VSL technique (which setup configuration is represented in fig. 1.19) the excitation beam forms a stripe, some centimeters long and few microns wide. This is used to assess amplification properties of the material. If the population is inverted along the stripe channel, it is possible to observe Amplified Spontaneous Emission (ASE) of the photons emitted along the excitation line. The detected signal is then given by the integral along the stripe of light intensity, which is subjected both to the Beer law (1.25) and to exponential amplification effects,

$$I(L) = \int_0^L I_0 e^{\alpha^* \Gamma l} dl = \frac{I_0}{\alpha^*} (1 - e^{\alpha^* \Gamma L}). \quad (1.26)$$

$\alpha^*$  is the material net gain, which can be decomposed in a positive, amplification term (internal gain  $g_{int}$ ) and a negative, lossy one ( $\alpha$ ), which includes absorption, propagation and excitation-induced losses ( $\alpha^* = 2g_{int} - \alpha$ ). The maximum value of  $g_{int}$  is given by  $|\alpha|$ , for a complete population inversion. In this case, it is straightforward to get  $\alpha^* = \alpha$ , which represents the maximum material gain. Conversely, when the sample is not excited,  $g_{int} = 0$  and  $\alpha^* = -\alpha$ , which clearly reproduces the material absorption. Actually, the term net gain can sound misleading, since it represents a real, physical gain only when population inversion is reached: nevertheless, this is the traditional nomenclature in VSL experiments, and has been used without forget its true meaning.

Indeed, to integrate eq. (1.26),  $I_0$  has been approximated as independent from the sample edge distance. Experimentally this can be done with a beam expander, which allows one to obtain a flat excitation beam intensity profile. Again, realizing different measurements as a function of the stripe length  $L$ , it is possible to extract the material net gain  $\alpha^*$ . Figure 1.21 reports the experimental results on sample A (panel (a)) and on Sample D (panel (b)). This last sample reproduces the typical behavior of most of the samples under study; its deposition parameters are reported in tab. 1.3. Sample A deposition parameter (reported in tab. 1.1) are restated here to allow an easy comparison between the samples.

It is worth to note the different trend of  $\alpha^*$  in the two samples: for clarity, the results obtained at 1535nm are reported in the right panel of fig. 1.21. While in sample D, increasing the excitation flux, the losses contribution increases more than the amplification one, indicating a predominant excitation pump induced losses mechanism (such as Confined Carrier Absorption, which will be described in more detail

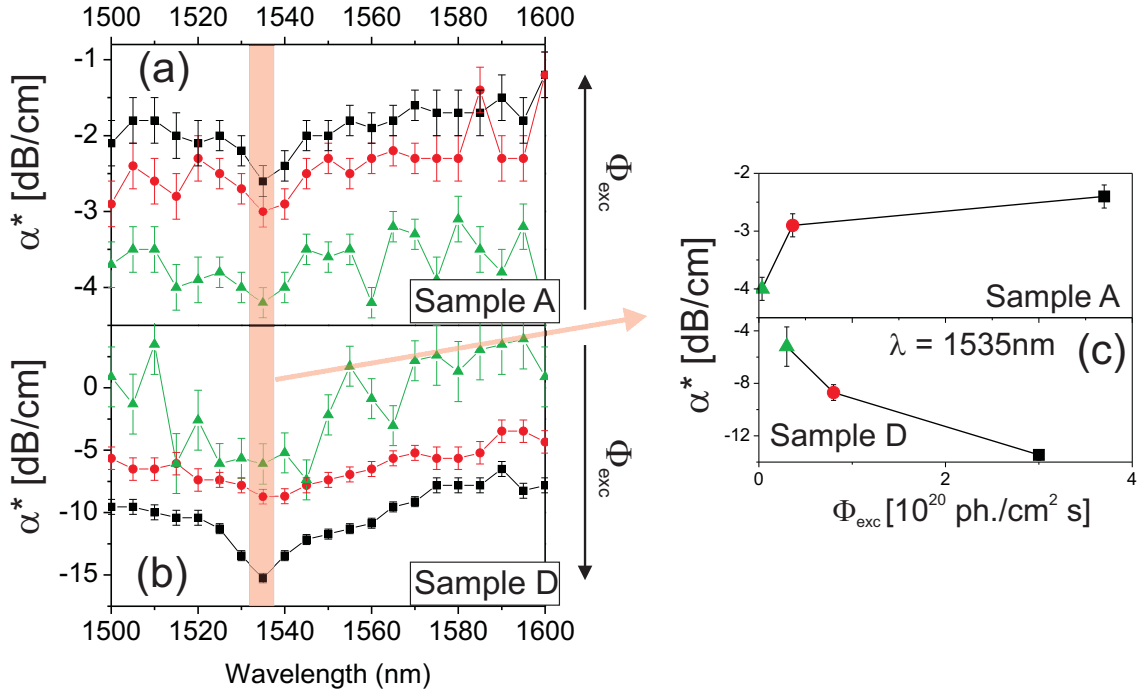


Figure 1.21: (a): Sample A  $\alpha^*$  obtained with the VSL technique at different excitation fluxes ( $\lambda_{exc}=488$ nm), reported in panel (b) with the same symbol notation.(b): Same results for sample D. (c): Comparison of  $\alpha^*$  at  $\text{Er}^{3+}$  peak emission wavelength (1535nm) in sample A and D as a function of excitation flux. Note the opposite trend for the two samples.

| Sample | Si exc (%)  | $[\text{Er}^{3+}][\text{cm}^{-3}]$ | $T_{ann}[\text{°C}]$ |
|--------|-------------|------------------------------------|----------------------|
| D      | $8.5 \pm 2$ | $3.4 \pm 0.2 \times 10^{20}$       | 900                  |
| A      | $5 \pm 2$   | $3.38 \pm 0.2 \times 10^{20}$      | 900                  |

Table 1.3: Sample D and A compositions. The annealing time was of one hour.

in the next section), in sample A the negative  $\alpha^*$  decreases with the excitation flux, indicating a larger contribution of optical amplification phenomena with respect to sample D.

It is important to point out that, even for sample A,  $\alpha^*$  is always negative, showing that, even if reduced, losses are still present in the sample and should be addressed in order to exploit the amplification properties of the material.

### Passive losses: cut-back technique

The results of VSL and SES measurements represent an estimation of optical properties of the SRSO:Er active material. When this is employed in a real working device, additional issues have to be addressed in order to get net gain. Similarly to a laser cavity, if the light amplification does not overcome the passive losses of the system, the net result will be a decrease of the signal which has been injected in the device in order to be amplified. The term passive losses includes the contributions of all loss channels which do not depend on sample active layer excitation (i.e. losses due to

non-perfect dielectric structure, material absorption losses, ecc...). The light-guiding properties of rib-channel waveguides have thus been analyzed by performing optical transmission experiments. The obtained value represents a key value to understand the minimum amplification needed to obtain net gain in the system.

To evaluate passive losses, a probe signal is injected into the waveguide channel employing a tapered optical fiber, mounted on a piezo-electric stage with nanometric resolution. At the opposite edge of the waveguide, the transmitted signal is then collected and can be analyzed by using a CCD camera to evaluate the far-field mode profile. Since the amplifier works in the spectral region of  $\text{Er}^{3+}$  ions emission, optical propagation has been studied employing a tunable IR-laser source (tunable range 1500 - 1600nm, with a maximum power of 10 mW) as a signal.

The light intensity at the output facet of the waveguide ( $I_{out}$ ) can be expressed as:

$$\frac{I_{out}}{I_0} = A_0 \cdot e^{-\alpha_{prop}L}, \quad (1.27)$$

where  $I_0$  is the intensity at the waveguide input. From inspection of eq. (1.27) it is possible to recognize two different kinds of losses, considering the different relation with the waveguide length  $L$ . Propagation losses have an exponential dependence from  $L$ , following Beer's law (1.25), with a characteristic loss coefficient  $\alpha_{prop}$ . This definition can include losses due to guided mode coupling with radiative modes, scattering losses due to inhomogeneity or imperfection of the dielectric structure and/or absorption losses due to the employed material. All the other losses can be represented by a constant factor  $A_0$  independent from  $L$ . The main contribution to this class is given by the mismatch between the input beam and the waveguide field modal shape (coupling losses).

Employing waveguides of different lengths it is possible to separate propagation and coupling losses contributions. Using this technique (cut-back technique [40]), rib-waveguide samples with SRSO:Er active layer have been characterized. The waveguide containing an active layer with the same composition and deposition parameters of sample A (see tab. 1.1) has been labeled A-wg and possesses the geometrical structure sketched in fig. 1.18 (d). Several sets of waveguide with different rib width (from 3 to 10  $\mu m$ ) have been checked, producing within error the same results, which are reported in fig. 1.22 (a), (b) for a  $w=5 \mu m$  waveguide. Within a good approximation, it is possible to completely associate  $A_0$  with the coupling losses in the system. The obtained value for this loss contribution ranges from 3 to 5 dB for every Er:SRSO waveguide with high quality facets (such as sample A). Outside  $\text{Er}^{3+}$  absorption peak, average propagation losses of  $3 \pm 0.5$  dB/cm have been found. Considering this result, it is possible to extract  $\text{Er}^{3+}$  ions absorption spectrum, which is reported in fig. 1.22 (c), where a maximum absorption of 4 dB/cm can be observed.

Then, if all  $\text{Er}^{3+}$  population is inverted, a maximum gain of 4 dB/cm is expected, which is enough to overcome propagation loss of 3 dB/cm, with a net gain of 1 dB/cm. Indeed, with industrial packaging technique it is possible to lower the coupling losses to value less than 1 dB per waveguide facet, allowing the possible production of optical amplifiers for telecom applications with few dB of gain maintaining at the same time a compact size of few centimeters.

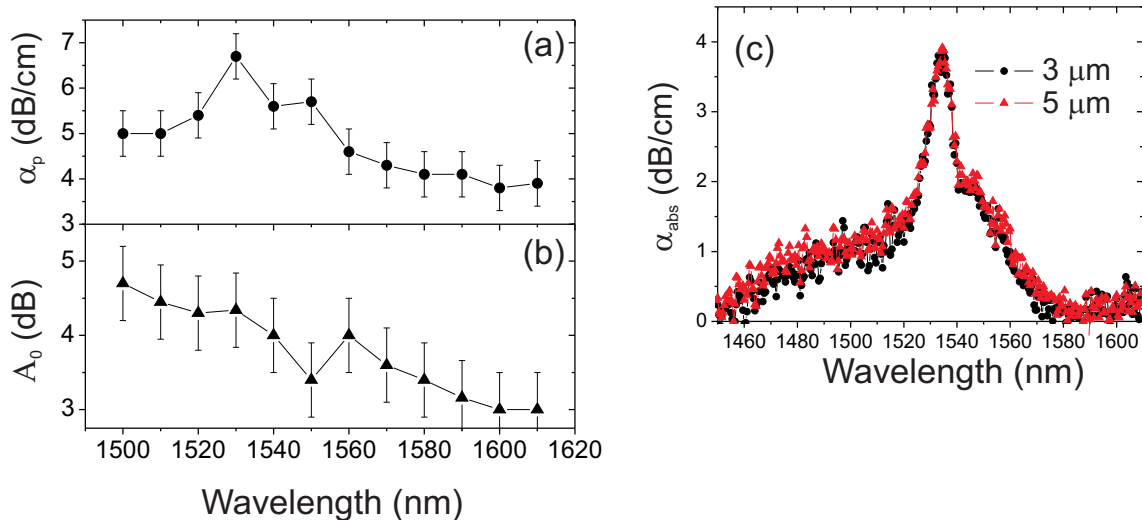


Figure 1.22: Propagation losses  $\alpha_p$  (panel (a)) and length independent losses  $A_0$  (panel (b)) obtained with the cut-back technique in sample A-wg. (c): Extracted absorption losses for two different channel widths in sample A.

Even if the possibility to get net gain in the waveguides has been discussed, the excitation induced material losses have still to be properly addressed and possibly reduced to negligible contributions. In fact, slab waveguides characterization of the previous sections clearly depict the existence of pump induced losses in the samples under analysis. In the following, the possible physical mechanisms related to these effects, that is cooperative up-conversion and confined carrier absorption, will be described and investigated.

### Cooperative Up-Conversion

The possibility to have strong cooperative-up-conversion effect in the samples can be investigated by means of PL related experiments. This phenomenon is an excitation induced losses in  $\text{Er}^{3+}$  systems: physically, when two excited ions are placed close enough, it is possible that one of them recombines exchanging its energy to the other one. Even if the electrons of the latter, which have been excited to high lying levels, quickly recombine to the first excited state, the net results obtained is to pass from two excited ions to a single excited ion, fastly depleting the inverted population [4]. Experimentally, the existence of such an effect can be proven by looking at Er-related PL lifetime reductions when excitation fluxes are progressively increased. As depicted in fig. 1.23 (a), the sets of sample described in this thesis show no modification of PL lifetime under resonant excitation, both considering the maximum and minimum available CW excitation fluxes. In this case it is difficult to estimate an up-conversion probability coefficient  $C_{up}$ . As a reference, it is possible to consider the coefficient  $C_{up}$  which has been derived in a typical samples belonging to an old set<sup>4</sup>. In particular, the found value of  $2 \times 10^{17} \text{ cm}^2/\text{s}$  represents an upper

<sup>4</sup>In particular, the PL lifetime reported in fig. 1.23 (b) have been measured in a sample with 7% Si excess,  $5.4 \pm 0.2 \times 10^{20} \text{ cm}^{-3}$   $\text{Er}^{3+}$  concentration, annealed at  $900^\circ$  for 30 minutes.

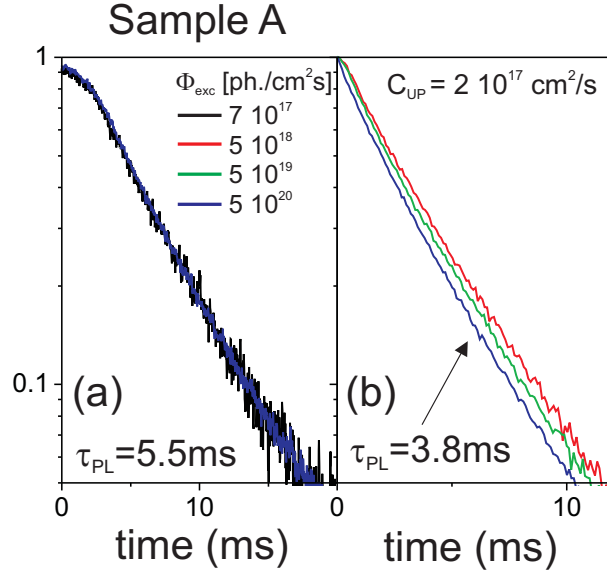


Figure 1.23: PL lifetime as a function of resonant excitation flux in sample A (a) and in an Er-doped SRSO sample which does not belong to the set here described (b). Note the lifetime decrease in panel (b), showing cooperative-up-conversion mechanisms.

limit to the up-conversion coefficient in the set of samples under investigation.

### Carrier absorption and signal enhancement in rib waveguides

Alternatively, the source of excitation power-dependent losses described in the previous sections can be attributed to Confined Carrier Absorption mechanism (CCA) [41, 42]. CCA is the analogous (for confined electron) of Free Carrier Absorption (FCA), which is one of the main effects which prevents efficient light emission in bulk Si [43]. When excitons in Si-np are created by optical injection, both electrons or holes separately can absorb light propagating in the structure, with the results of being promoted to very high levels. A very fast thermalization allows the particles to return to their original level. In a first approximation, it is assumed that CCA effects do not impact on excitons population, yet represent an additional, pump-induced, source of optical losses in the material.

Since it represents a hindrance to reach net gain in  $\text{Er}^{3+}$  doped SRSO amplifiers, CCA mechanism in the IR has been addressed in multi-layer (ML) SRSO/ $\text{SiO}_2$  samples without  $\text{Er}^{3+}$ .

Noteworthy, typical Er:SRSO samples show a great contribution of excitation-induced losses. To address the CCA behaviour in presence of  $\text{Er}^{3+}$  ions, a preliminar set of samples, with different Si-np and  $\text{Er}^{3+}$  concentrations, has been investigated. Once the mechanism is understood, the optimum material composition in terms of CCA-related losses can be achieved. Table 1.4 reports the characteristic of some of the samples under study. Optical active characterizations have been performed with the pump & probe technique [44]. In this method, different transmission measurements are compared, where the optical excitation of the sample is respectively turned on

| Sample | Si-np conc. [ $\text{cm}^{-3}$ ] | $[\text{Er}^{3+}][\text{cm}^{-3}]$ | annealing T [ $^{\circ}\text{C}$ ] and time [min] |
|--------|----------------------------------|------------------------------------|---|
| ML-A   | $3.5 \pm 1.2 \times 10^{18}$     | -                                  | 1080, 60  |
| Sample | Si exc (%)                       | $[\text{Er}^{3+}][\text{cm}^{-3}]$ | annealing T [ $^{\circ}\text{C}$ ] and time [min] |
| CA1    | $7 \pm 1$                        | $4.5 \pm 0.1 \times 10^{19}$       | 900, 60   |
| CA2    | $7 \pm 1$                        | $4 \pm 0.1 \times 10^{20}$         | 900, 60   |
| CA3    | $7 \pm 1$                        | $5.4 \pm 0.1 \times 10^{20}$       | 900, 30   |
| CA4    | $7 \pm 1$                        | $5.4 \pm 0.1 \times 10^{20}$       | 900, 10   |

Table 1.4: Sets of sample under study for CCA characterization.

or off. Figure 1.24 reports an optical photograph of the pump & probe setup.

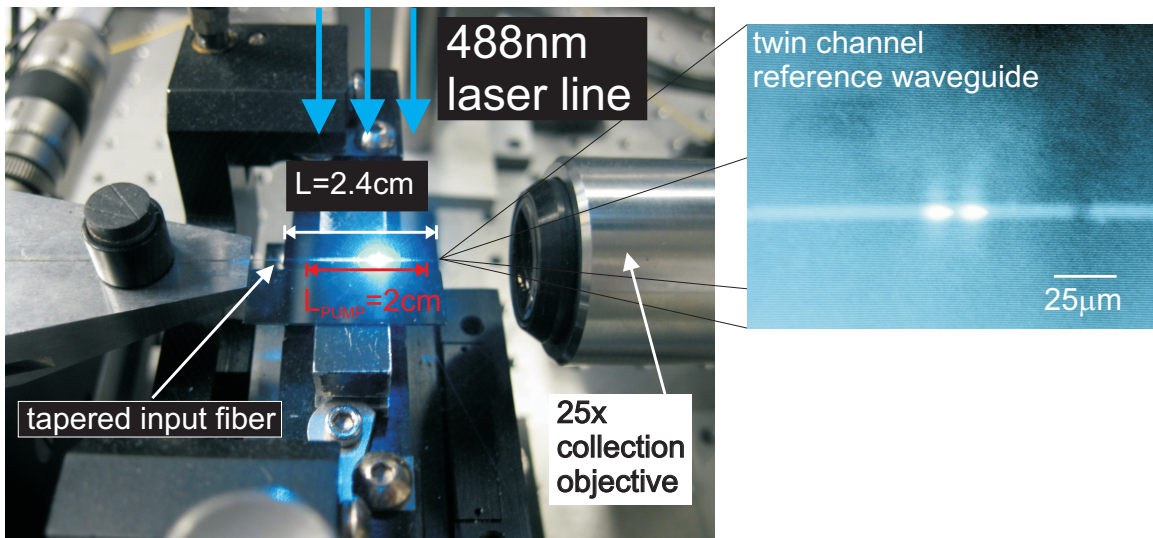


Figure 1.24: Optical photograph of pump & probe setup. Note the excitation stripe (2cm long) focused along the 2.4cm waveguide under study. The good alignment of the stripe can be checked from the top with a zoomed CCD camera. Moreover a different CCD camera is placed at the waveguide output, where the guided mode excited by active layer spontaneous emission and ASE can be controlled. The zoomed image reports an optical photograph of the waveguide mode when a twin-reference  $10\mu\text{m}$  channel is excited.

The optical excitation is performed through top-focusing the  $\text{Ar}^+$  laser excitation by means of a cylindrical lens. The beam is focused in a long stripe on top of a single channel waveguide, as reported in fig. 1.24. The standard stripe is 1 - 2 cm long, with a maximum width of about  $10\mu\text{m}$ , as measured employing a zoomed top-view CCD camera. The inset of fig. 1.24 shows a cross-view image of the optical mode at the waveguide output, which has been obtained through spontaneous emission of  $\text{Er}^{3+}$  when the active material is excited with the pump stripe. The clear modal shape is a proof of the good optical pump alignment. Note that in this case the waveguide is composed by twin  $10\mu\text{m}$  wide rib channels which are used for reference and are very spaced from the single rib waveguides which have been considered in the measurements.

The probe input (1500 - 1600 nm wavelength) is injected into the waveguide with a tapered fiber. The collection is performed, at the opposite edge, using a  $25\times$  micro-

scope objective and analyzed with a IR-detector.

Two-steps measurements have been performed:

$$\begin{cases} I_{out}^p = I_{in}e^{-\alpha\Gamma L} & \text{probe on - pump off} \\ I_{out}^{P\&p} = I_{in}e^{[-\alpha L + \alpha^*(\Phi_{pump})L_{pump}]\Gamma} & \text{probe on - pump on} \end{cases} \quad (1.28)$$

where the symbol notation is the same as before. The term  $\alpha^*(\Phi_{pump})$  is a loss/gain coefficient which depends from the excitation photon flux. The ratio of  $I_{out}^{P\&p}$  and  $I_{out}^p$  in (1.28) is called, for historical reason, signal enhancement (SE). From SE measurements, it is possible to extract  $\alpha^*$ , employing the formula:

$$\frac{I_{out}^{P\&p}}{I_{out}^p} = SE = e^{\alpha^* L_{pump}\Gamma} \rightarrow \alpha^* = \frac{\ln SE}{\Gamma L_{pump}} \quad (1.29)$$

If the CCA mechanism is investigated,  $\alpha^*$  is given by the product  $(-N_{exc,2} \cdot \sigma_{CA})$ , where  $N_{exc,2}$  has the same meaning as before, and  $\sigma_{CA}$  is the cross section of the process.

CCA-losses have been quantified for samples in tab. 1.4. Sample ML-A contains only Si-np and the CCA losses related to this one can be important to understand the difference with the FCA mechanism in bulk Si.  $\alpha^*$  has been evaluated at 1550nm, considering different excitation fluxes: a particular of one typical pump-on, pump-off measurement has been reported in the inset of fig. 1.25 (a). Due to the closely spaced nature on the Si-np layer, dominating inter-particles Auger processes are expected. These scale with excitation flux with a characteristic power law ( $y = a \cdot x^b, b=0.5$ ), which is well reproduced by the data fit of fig. 1.25 (a) ( $b_{fit} = 0.49 \pm 0.02$ ) [41]. The maximum CCA-losses have been found to be as high as 6 dB/cm. Assuming that at larger fluxes Auger dynamics completely dominates excitons population (i.e.  $N_{exc,2} = N_{Si-np}$ ), it is possible to extract  $\sigma_{CA}$ . This has been found to be  $4 \times 10^{-19} \text{ cm}^2$ : it is worth to note this is one order of magnitude lower than the FCA cross-section in silicon ( $\sigma_{FCA} \sim 10^{-18} \text{ cm}^2$  at 1535nm [45]).

Even if, when  $\text{Er}^{3+}$  is inserted in the samples, stimulated emission phenomena are expected, measured  $\alpha^*$  values were negative and decreasing with excitation flux for every sample of tab. 1.4. Although a simple model can not be easily extracted from the data, some qualitative results can help in getting some insights of the detrimental processes in presence of transfer mechanism among  $\text{Er}^{3+}$  ions and Si-np. Figure 1.25 (b) reports the pump & probe measurements comparison for the investigated samples. The most significant result is the effect of energy transfer on CCA-related losses. It is assumed that the Si-np contained in the last four samples of tab. 1.4 differ only for the different sizes<sup>5</sup>. It is possible to appreciate the reduction of CCA-losses in sample CA2 with respect to sample CA1. These two samples

<sup>5</sup>While the number of Si-np is essentially given by the number of nucleation centers, which itself depends on the Si-excess, the size of Si-np depends on the annealing time, resulting in larger particle for longer annealing times

posses the same kind of Si-np yet different  $\text{Er}^{3+}$  concentration. Noteworthy, larger losses are observed for the sample with less  $\text{Er}^{3+}$  content. If one correlates the larger

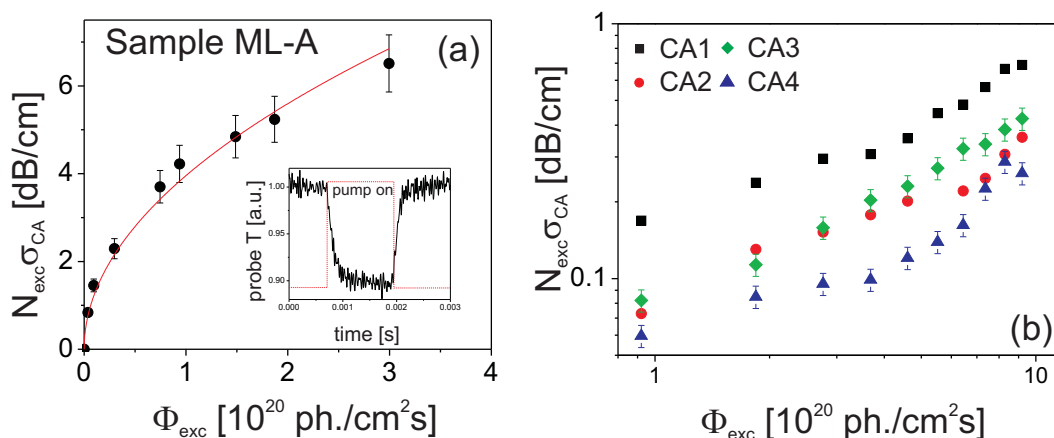


Figure 1.25: (a): CCA losses evaluated with pump & probe technique for sample ML-A. The solid line is a power-law fit  $y = a \cdot x^b$ , where  $b=0.48 \pm 0.02$  has been found, hinting toward inter-particles Auger dominating mechanism. In the inset a typical pump-on pump-off measurements is reported, where it is possible to appreciate the signal decrease when excitation is turned on. (b): The same measurements for samples with different kinds of Si-np and  $\text{Er}^{3+}$  concentration is reported.

number of  $\text{Er}^{3+}$  ions to a larger energy transfer effect, the reduction of CCA can be interpreted considering that the energy transfer itself contributes in the depletion of population  $N_{exc,2}$ , through indirect Auger recirculation, as reported in sec. 1.2. The more the ions are coupled, the larger the depletion in the exciton population, realizing a decrease of CCA losses. More difficult is an easy interpretation of the results for samples CA2, CA3 and CA4. They have the same Si content but the annealing duration has been shortened progressively while keeping the same annealing temperature. This results in smaller Si-np from CA2 to CA4, having CA4 the shortest annealing time. Thus, some insights can be obtained from the steady-state exciton population, which can be evaluated as:

$$N_{exc,2} = \sigma_{Si-np} \Phi_{exc} N_{Si-np} \tau_{PL}, \quad (1.30)$$

where the same notation of eq. (1.7) has been used. Smaller Si-np posses both a shorter  $\tau_{PL}$  (shorter radiative lifetimes) [13] and a smaller absorption cross section [26]. If the population is not completely dominated by Auger recombination, it is expected that in smaller Si-np a smaller number of excitons is created, this in turn means minor CCA losses.

The results of fig. 1.25 for samples CA3 and CA4 qualitatively reproduce the above-mentioned expected results, with reduced CCA in the sample with smaller nanoparticles. Conversely, the results of sample CA2 does not fit with this simple model, being the magnitude of  $N_{exc} \sigma_{CA}$  of the same order of the one found for sample CA3. This again points out the effects of energy transfer which contributes to a fast exciton depletion, reducing CCA losses. Empirically, the  $\text{Er}^{3+}$  emission intensity under indirect excitation was stronger in sample CA3 than in CA2, suggesting that in the

latter, though CCA is reduced from Si-np side, a less efficient transfer makes the net losses comparable with sample CA3. It is indeed clear that a compromise between reduced CCA losses and transfer mechanism has to be found, since a reduction of the number of excitons, which would reduce the magnitude of CCA phenomena, at the same time quenches the energy transfer efficiency itself.

In fact, as will be reported in the case of sample A, while CCA losses have been strongly reduced with respect to the typical values experienced in Er-doped SRSO systems [46], the sensitization effect is not strong enough to realize optical gain.

In case of amplifying materials, it is possible to extract the system internal gain from  $\alpha^*$  ( $\alpha^* = 2g_{int} - \alpha_{abs}$ ), when population inversion is reached.

Another issue to be taken care of is represented by Amplified Spontaneous Emission (ASE) signal, which is a source of noise in the amplifier. Physically, this is formed by amplification of spontaneous emission photons generated within the excited material. Due to the isotropic and non-monochromatic nature of spontaneous emission, ASE signal is a broadband noise source, which can be evaluated in the experiments with a "pump-on, probe-off" measurements. This is necessary in order to estimate correctly  $\alpha^*$  contribution to SE. Fig. 1.26 reports the results of pump

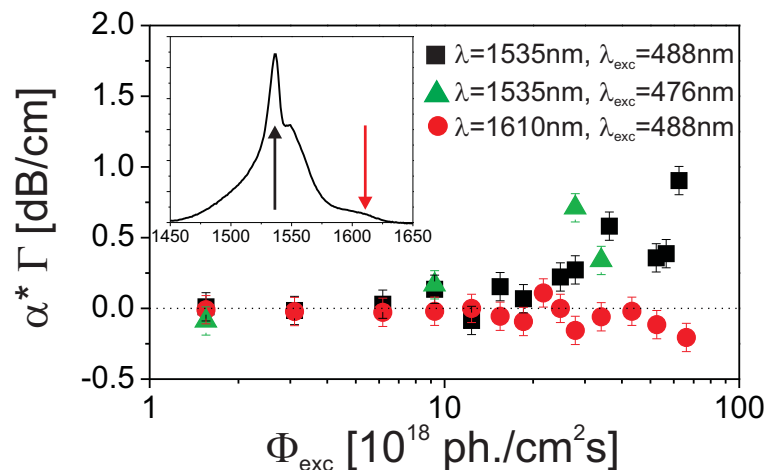


Figure 1.26:  $\alpha^*\Gamma$  measured in sample A-wg with pump & probe technique. The results for probe wavelengths tuned with the  $\text{Er}^{3+}$  emission peak (1535, black arrow in the inset) and almost outside the gain spectrum (1610nm, red arrow in the inset) and for different excitation wavelengths are compared. Resonant (488 nm) and non-resonant (476nm) excitation generates the same results, with a negligible role of  $\text{Er}^{3+}$  direct contribution. It is worth to note that at 1610nm  $\alpha^*$  reaches a value as low as 0.2 dB/cm, indicating a strong reduction of CCA-related losses.

& probe measurements on sample A-wg. When the  $\text{Er}^{3+}$  emission peak is probed ( $\lambda_{probe}=1535\text{nm}$ ),  $\alpha^*$  becomes greater than zero when the pump flux is increased; on the other hand, outside  $\text{Er}^{3+}$  emission peak ( $\lambda_{probe}=1610\text{nm}$ ), it is possible to appreciate dominant CCA-related losses, which reaches a maximum value of 0.2 dB/cm at the largest excitation flux. It is also worth to note that the same trend has been observed both for  $\text{Er}^{3+}$  resonant ( $\lambda_{exc}=488\text{nm}$ ) and non-resonant ( $\lambda_{exc}=476\text{nm}$ ) excitation, showing again how  $\text{Er}^{3+}$  direct absorption cross section is negligible with

respect to energy transfer effective cross section. Even if it is a difficult task to separate amplification and CCA contribution, we can conclude that in sample A the CCA impacts less on the amplifier performance. In fact, most of samples which have been characterized by pump & probe experiments shows a net decrease in the signal intensity when the pump is turned on. In fig. 1.27 (a) a typical results of pump & probe measurements is shown for sample E, whose composition is reported in tab. 1.5. It is interesting to note that CCA-losses contribution (which in this

| Sample | Si exc (%) | [Er <sup>3+</sup> ][cm <sup>-3</sup> ] | annealing time[min] |
|--------|------------|--|---------------------|
| E      | 10 ± 1     | 1 ± 0.1 × 10 <sup>20</sup>             | 60                  |

Table 1.5: Sample E composition. The annealing temperature was 900°C.

non-optimized sample can be as large as 1.5 dB/cm) is dominating for every probe wavelengths, although reduced at Er<sup>3+</sup> emission peak spectral position (1535 nm). On the other hand, outside the gain spectrum (1610 nm) a stronger decrease can be appreciated. This means that a competitive amplification mechanism exists, although weaker than CCA detrimental effect. The SE at 1535 nm has been finally investigated for a wide range of excitation fluxes, and results reported in fig. 1.27.

Concluding, optimized sample A-wg shows  $\alpha^*$  greater than zero. This means that

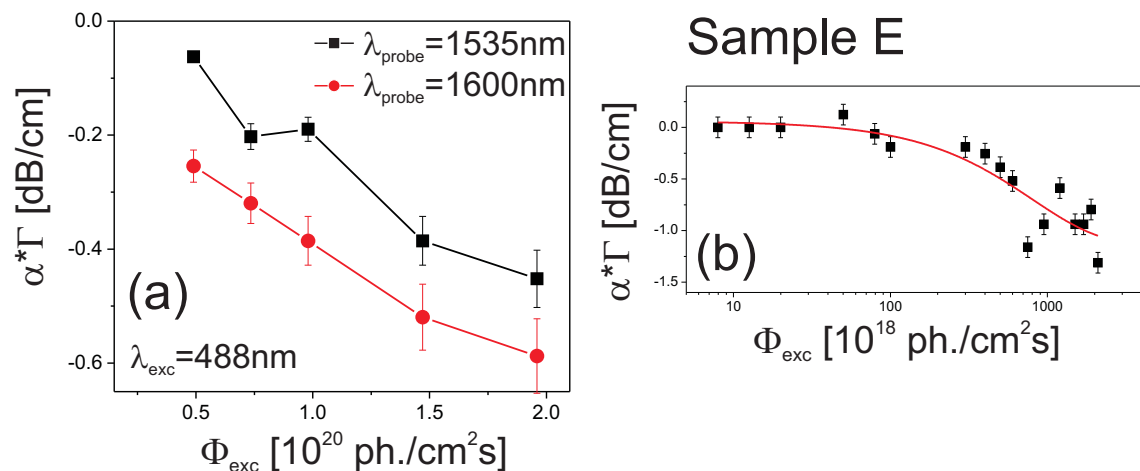


Figure 1.27: (a): Spectral signal intensity for a standard Er:SRSO waveguide (composition specified in the text), which represents the average behavior of the sets under analysis. (b):  $\alpha^*\Gamma$  at 1535nm as a function of excitation flux. The red curve is a line for the eye.

light amplification induced by stimulated emission starts to overcome excitation-induced losses, which have been attributed to the CCA mechanism. The possibility to explore sample A-wg behavior at larger excitation fluxes sounds intriguing, but additional effects, such as thermal expansion and/or nonlinear effects in Si-np, dominates the light dynamics within the waveguide, possibly masking amplification effects.

It is important to understand again the mutual role of CCA losses and optical amplification in the samples. Being both processes proportional to the number

of created excitons, it is impossible to decorrelate the contributions to the signal dynamics. As seen, even if CCA losses can be greatly reduced, obtaining positive  $\alpha^*$  values, the corresponding gain reduction does not allow the achievement of net gain in the system. On the other hand, when the number of excitons is increased, CCA-losses completely rule out optical amplification effects. A smart solution in this sense would be to increase the transfer efficiency without resorting to an increase in excitons number. This could be done, for example, enhancing the photon Density of States (DOS) at optical wavelengths in proximity of the transitions which are responsible for the energy transfer. To this end, a detailed excitation spectra measurement of Er-doped SRSO material is mandatory.

## 1.4 Conclusions

In this chapter I have shown spectroscopic experiments in photoluminescent samples where the energy transfer among Si-np and  $\text{Er}^{3+}$  ions is observed. In the last years, confined carrier absorption detrimental effect in Si-np has been widely investigated, representing one of the hindrances towards Si-np-based light emitting devices. Here, the material has been empirically characterized by means of pump & probe experiments to minimize CCA related-losses. With the most promising material composition for reduced CCA (in terms of Si-np and  $\text{Er}^{3+}$  content), an additional optimization has been performed, modifying the deposition parameters in order to maximize the energy transfer process having, at the same time, a long lifetime for  $\text{Er}^{3+}$  first excited state transition. The resulting sample has shown good potentiality as a candidate for amplifier devices: the SE coefficient  $\alpha^*$  (related to excitation-induced loss/gain) reaches 1 dB/cm and a 56% of optically active ions are coupled to Si-np. On the other hand, some issues have to be solved in order to get net gain in the system: the large fraction of optically de-active ions (89% of the total concentration), though not representing a detrimental effect, reduces the possibility to obtain large gain values and eventually overcome the passive losses of the system. Most important, it has been realized that, though reduced to low values, CCA related losses still represent an important detrimental issue in the systems, which can not be decorrelated from the amplification dynamics. To improve the understanding of the system, the energy transfer mechanism among Si-np and  $\text{Er}^{3+}$  ions has been widely investigated. Having not found traces of reported intrinsic limits to sensitization, such as Auger back-transfer effects, the hypothesis of distance-dependent energy transfer has been further strenghten. This has been modeled considering an effective trap states that acts similarly to  $\text{Er}^{3+}$  donor level in bulk Si. Even if it requires great technological effort to be accomplished, the possibility to place more  $\text{Er}^{3+}$  close to Si-np does not represent an intrinsic limit of the system and, if realized, can both increase the number of coupled ions decreasing, at the same time, the impact of CCA in the system.

## Appendix to chapter 1

### Transfer mechanism in re-annealed samples

To understand how the transfer mechanism is related to the Si-np phase a second annealing treatment has been performed in both samples A and B (see tab. 1.1), for one hour at 1100°, in order to ensure the full phase separation between SiO<sub>2</sub> and Si and the full crystallization of the nanoparticles. The new samples have been labelled as A-re and B-re. Figure 1.28 reports the decay curves of sample B-re in the visible range. The lifetimes, extracted using eq. (1.4) and plotted in the inset, show a net trend as a function of the detection wavelengths. This is indeed a clear signature of the high crystalline quality of the re-annealed samples [13]. It is worth to compare this last result with the lifetimes obtained in sample B (see fig. 1.9 (a)), which did not show any particular spectral trend. When Er<sup>3+</sup> is inserted into the sample the visible lifetime is reduced, and the PL band is quenched as a whole, reproducing qualitatively the same results whose have been observed in sample A and B. Even

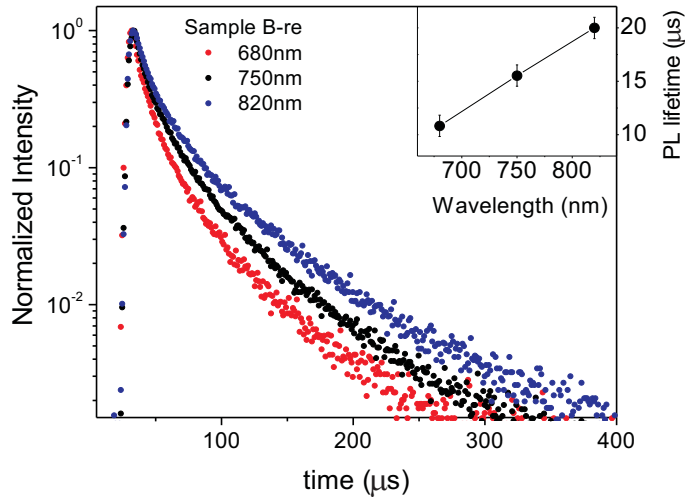


Figure 1.28: Visible PL decay of sample B-re at different detection wavelength. In the inset the average PL lifetime, extracted using eq. (1.4) is reported. Note the clear PL lifetime trend which confirms the good crystallinity of the nanoparticle in the sample.

in the IR region spectroscopic experiments give the same qualitative results which have been found for non-reannealed samples. Both in samples A-re and B-re a fast decaying lineshape is present, as reported in fig. 1.29 (a), where the comparison of the pre-annealing and post-annealing samples can be appreciated. The most striking difference in the new set of samples is related to quantitative results. Figure 1.29 (b) and (c) reports wide range PL spectra for pre and post-annealing samples. An anti-correlation between Si-np and Er<sup>3+</sup> emission can be noted: while the first is enhanced by the annealing treatment, the second is quenched of more than two orders of magnitude, indicating a less-efficient energy transfer process.

Since all the spectroscopic features analyzed for samples A and B are present in samples A-re and B-re, their experimental decay curves have been fitted using the same model of eq. (1.7), where the Dexter interaction distance has been changed

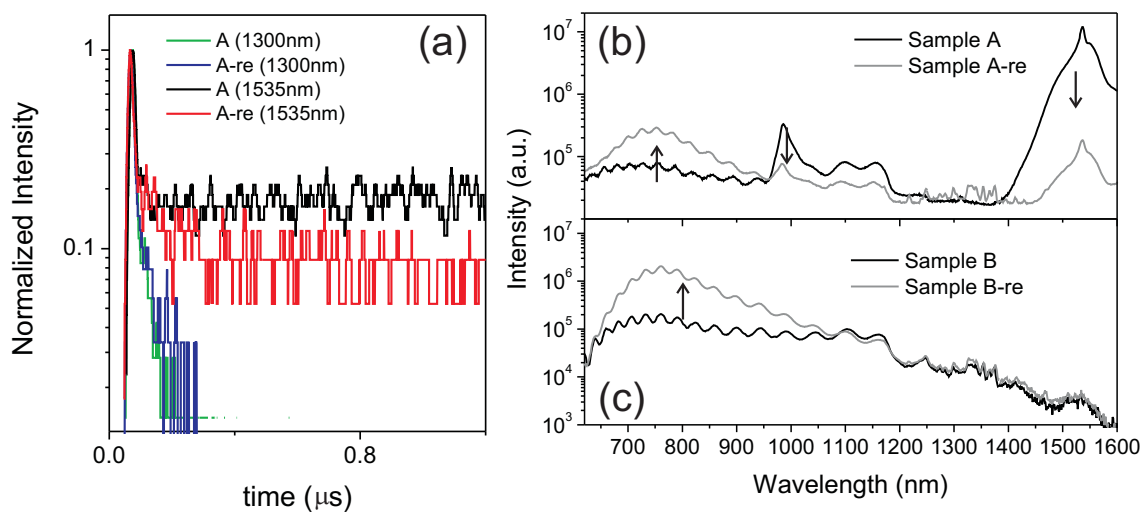


Figure 1.29: (a): Comparison of IR-PL decays of sample A and sample A-re. Note that the fast lineshape is present in every sample for every detection wavelength. (b): comparison of sample A and A-re non-resonant CW-PL ( $\lambda_{exc}=476\text{nm}$ ). Note that the reannealing both quenches  $\text{Er}^{3+}$  PL signal and enhance Si-np visible signal. (c): Comparison of sample B and B-re non-resonant CW-PL.

accordingly to take into account the crystalline nature of the nanoparticles ( $R_D = 2.1 \text{ nm}$  [28]). Results similar to those of sample A and B have been obtained for re-annealed samples, with a  $R^2$  of 0.96 and 0.88 for sample A-re and B-re, respectively<sup>6</sup>. The longer interaction distance  $R_D$  with respect to the amorphous case makes the model less reliable, since it is necessary to introduce large Er-Si-np distances ( $\sim 15\text{-}20 \text{ nm}$ , in comparison with 6-7 nm for nanoclusters) to reproduce the experimental data. For these distances the hypothesis of a single nanoparticle interacting with many  $\text{Er}^{3+}$  ions can not be strictly verified. The range of coupling constant obtained,  $k_i = [5 \times 10^{-10} - 1 \times 10^{-9}] \text{ cm}^3/\text{s}$ , has to be intended as a guess of the actual values. Nevertheless, good fit of the decay lineshapes for all the samples employing the same rate equations validate the hypothesis of the existence of a single kind of energy transfer mechanism. From the rise of the  $^4I_{11/2}$  level an average transfer time of  $117 \pm 30 \text{ ns}$  has been evaluated.

<sup>6</sup>In this case,  $C_A = 1 \pm 2 \times 10^{-33} \text{ cm}^6/\text{s}$  while  $w_{321} = \pm 3 \times 11^{10} \text{ s}^{-1}$ , where the same notation of eq. (1.7) has been used.



## Chapter 2

# Microdisk resonators: photoluminescence, strain engineering and Purcell enhancement

While in chapter 1 some properties of light emitting materials were exploited to generate/amplify radiation, in this chapter, conversely, the possible modification of material properties induced by a coupling with optical fields is analyzed. To achieve this result it is important to be able to control light with a great degree of precision. In this sense, technological improvements in the last years have developed an intense research in optical microcavities, that is dielectric structures in which electromagnetic fields at optical frequencies can be localized by means of total internal reflection effect [47]. Between the others, whispering gallery mode (WGM) resonators, where the dielectric structure is azimuthally symmetric, have raised a lot of interest mainly due to the easyness of fabrication, which relaxes the ultra-high resolution process needed to create photonic crystal cavities with similar properties. The peculiar name of such structures derives from the analysis of echoes effects of acoustic waves in the dome of St. Paul cathedral (London) by Lord Rayleigh, at the beginning of last century [48].

Further, CO<sub>2</sub>-laser melting technique in SiO<sub>2</sub> microdisks has revealed the possibility to create micro-toroid shaped resonators, where quality factors as large as 10<sup>9</sup> have been measured [49]. Such a high achievement opens the route to the employment of WGM resonators in many different fields: from applied physics, as in biosensing [50] or on-chip laser sources [51], to pure fundamental physics. WGM resonators are indeed used as platforms where Cavity-Quantum-Electrodynamics (C-QED) effects can be observed, such as light-matter strong coupling [52].

In this chapter, I will report a detailed optical characterization of microdisk resonators with Si-np. As discussed in chapt. 1, Si-np posses a wide PL band in the visible: when they are embedded in a dielectric microcavity, an external laser source is sufficient to observe WGMs generated by optical injection via spontaneous emission of the nanoparticles. The possibily to excite a *single* disk it is quite interesting

both to analyze the photonic properties of the dielectric and, at the same time, to get informations of the emitters within. In particular, I will report as the CCA mechanism can be characterized, employing simple PL measurements, whereas for standard waveguides complicated experiments have to be performed, as reported in sec. 1.3.2.

After that, I will show optical measurements related to light-matter interaction in the weak coupling regime. In this regime, field and emitters can be safely considered as separate physical entities, even though they can strongly influence each other. The radiative rate enhancement of an emitter coupled to a cavity resonance (Purcell effect [53]) will be shown for Si-np at room temperature. Even if Si-np are bad emitter for Purcell effect observation, the first convincing measurements of enhancement for this material will be reported and, more importantly, a novel technique for emitter linewidth estimation will be proposed.

When microdisks are fabricated using hybrid bi-layer structure, they are subjected to stress at the different material interfaces. This is usually considered a detrimental effect, but can be exploited to create micro-cup-shaped resonators (micro-kylix), in which the spectral region where the largest Q's are found can be tuned of tens of nm, changing the strength of stress deformation in the cavity itself.

The possibility to couple different microdisks stacking one on top of the other sounds intriguing. This geometry increases the coupling coefficient with respect to the point-like and planar coupling which is usually realized in WGM-based Coupled Resonator Optical Waveguides (CROWs) [54]. New physical phenomena can be observed, such as optical dipole forces [55, 56]. When a constituting material with only third order nonlinearities is considered, vertically coupled microdisk could offer a platform to observe the theoretically predicted optical analogous of Josephson current oscillations in superconductor-insulator junctions [57], which is due to nonlinear Optical Parametric Oscillation (OPO) effects [36, 58, 59].

As reported in [61], Si-np possess a strong Kerr nonlinearity, whereas their Pockels nonlinearity is negligible due to their centro-symmetric shape; indeed they represent the ideal candidate to be employed as nonlinear material to observe the abovementioned effects. To investigate the Josephson oscillations, I will report simulations aiming to the structure design.

## 2.1 Active microresonator with Si-np

In this section active (i.e. photoluminescent) microdisk resonators are analyzed. The active material inserted in the microcavity is composed by Si-np embedded in SiO<sub>2</sub>. The nanoparticles emit in a wide PL band in the visible, centered at about 750 nm. At first, some basics aspects regarding the physics of these structure are presented. Then, details of experimental optical characterization are discussed.

### Whispering Gallery Mode resonators: basics

As briefly stated before, WGM resonators are dielectric structures which possess azimuthal symmetry, such as disks, rings, spheres or toroids. Light circulates into the cavity due to total internal reflection at the dielectric edges. If it eventually

interferes constructively with itself after a round trip, optical resonances are generated. Physically, these are not *fully*-guided mode: a portion of light radiates outside the cavity due to its bended geometry. A photon within the cavity can be sustained only for finite time: after this it is lost, both through radiative emission or internal recombination. If one defines the average *photon lifetime* as  $\tau_{cav}$ , a usual figure of merit for the cavity is given by the quality factor  $Q$ , which is proportional to the lifetime itself:

$$Q = \omega\tau_{cav}, \quad (2.1)$$

where the proportionality constant is given by the optical frequency  $\omega$ . Resonant lineshapes are spectrally broadened (at least) due to the metastable nature of the cavity modes, forming lorentzian peak which width ( $\Delta\omega$ ) can be directly related to  $Q$  as:

$$Q = \frac{\omega}{\Delta\omega}. \quad (2.2)$$

Narrow spectral peaks in the cavity spectrum implies long photon lifetimes. Another important parameter is given by the spectral distance between neighboring resonances, which is called Free Spectral Range (FSR) and can be analitically approximated, in a circular resonator of radius  $R$ , as:

$$FSR = \frac{\lambda^2}{2\pi n_g R}, \quad (2.3)$$

where  $\lambda$  is the mean wavelength of the two resonances and  $n_g$  is the mode group index<sup>1</sup>.

Without entering too much into the details, which can be found in standard textbooks (for example, [36]), it is worth to decompose Helmholtz equation (1.18), which governs the propagation of light, for the azimuthally symmetric geometry. Starting from its expression in cylindrical coordinates  $[\rho, \theta, z]$ :

$$\left[ \frac{\partial^2}{\partial \rho^2} + \frac{1}{\rho} \frac{\partial}{\partial \rho} + \frac{1}{\rho^2} \frac{\partial^2}{\partial \theta^2} + \frac{\partial^2}{\partial z^2} + k^2 \epsilon(\rho, \theta, z) \right] E_i(\rho, \theta, z) = 0, \quad (2.4)$$

it is possible to separate the equation in the three cylindrical directions. Considering the product  $E_i = P(\rho) \cdot \Theta(\theta) \cdot Z(z)$  and the azimuthal symmetry, one has:

$$\left\{ \begin{array}{l} \left( \frac{d^2}{dz^2} + k^2(\epsilon(z) - \beta) \right) Z(z) = 0, \\ \left( \frac{d^2}{d\theta^2} + m^2 \right) \Theta(\theta) = 0, \\ \left( \frac{d^2 P(\rho)}{d\rho^2} + \frac{1}{\rho} \frac{dP(\rho)}{d\rho} + \left( k^2 \beta - \frac{m^2}{\rho^2} \right) \right) = 0. \end{array} \right. \quad (2.5)$$

---

<sup>1</sup>In a lossless medium a wavepacket travels with a velocity which is given by the derivative of its frequency-dispersion curve,  $v_g = \partial\omega/\partial k$  (group velocity). The group index is then given by  $n_g = c/v_g$ . More details on group velocity and index are reported in chapt. 3.

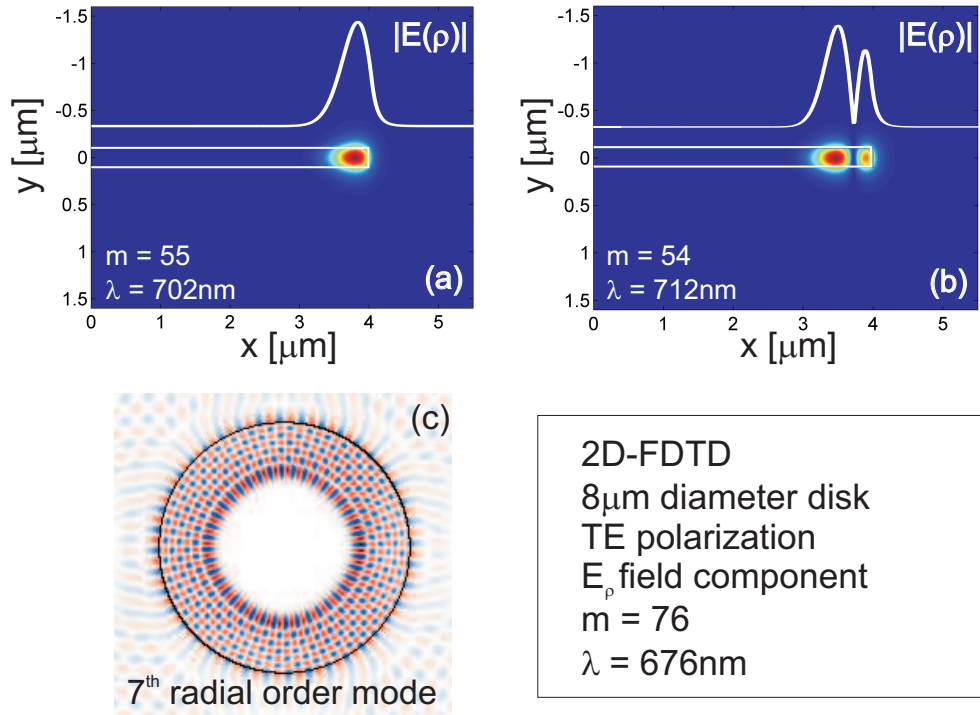


Figure 2.1: First (panel (a)) and second (panel (b)) radial families field modulus. The field amplitude along  $\hat{\rho}$  at  $z = 0$  is briefly sketched in the top part of the figures. The fields are eigenfunctions of the scalar Helmholtz equation. (c) 2D-FDTD computation of a large order radial family ( $7^{th}$ ) for TE polarization.

From the solutions of equations in the system, *optical quantum number* can be extracted to label the WGM in a disk resonator. The equation for  $Z(z)$  and  $\Theta(\theta)$  can be solved analytically: the first is the analogous of the one for planar dielectric waveguides, which has been solved in sec. 1.3.2, while the latter has a simple exponential solution,  $\Theta(\theta) \propto e^{im\theta/2\pi}$ . The equation for  $P(\rho)$  has no analytical solution. However, it can be approximated with a Bessel function inside the disk and with an exponential decaying function outside. A general WGM can then be characterized specifying the polarization (quasi-TE/quasi-TM), the azimuthal number  $m$  (number of nodes along  $\hat{\theta}$ ), the mode order along  $\hat{z}$  (with an increasing number of nodes) and the mode order along  $\hat{\rho}$  (with an increasing number of Bessel's functions antinodes). The latter represents modes which propagates at different distances from the disk's edge. For example, the simulation of a very high order mode ( $7^{th}$  radial order) is reported in fig. 2.2 (c) where a 2D-FDTD code has been employed (more on this later). It is possible to note that most of the field components are internal to the disk.

It is straightforward to solve Helmholtz's equation in cylindrical coordinates (2.4) for a scalar field: even if this represents an approximation of the real solution, it can offer useful insights on the WGM modal shape. Figure 2.1 reports the first and second radial order mode in a  $8\text{-}\mu\text{m}$  diameter disk ( $n_{disk}=2$ ). The absolute value of the field are depicted along a cross section of the structure. Along  $\hat{\theta}$ , the modes are harmonic waves with azimuthal number respectively of  $m=55$  and  $m=54$ .

A more exact solution can be obtained using different numerical methods, such as

the Finite Difference Time Domain one (FDTD) [62]. In this method, the Maxwell equations are solved in the time-domain in a discretized real space. More details about the method can be found elsewhere [63]. The following simulations, unless stated differently, have been performed with an open-source FDTD code [64]. With this technique, the eigensolutions of eq. (2.4) can be obtained exciting the disk modes with dipole sources and making the simulation run as long as all the radiative-transient related field components die out. Figure 2.2 reports the quasi-TE first order radial mode for a 125 nm thick, 8  $\mu\text{m}$  diameter disk ( $n_{\text{disk}} = 1.7$ ). Note the  $E_\rho$  discontinuity in the field profile at the edge of the disk, as expected for quasi-TE polarization. FDTD simulations are often considered as ideal experiments:

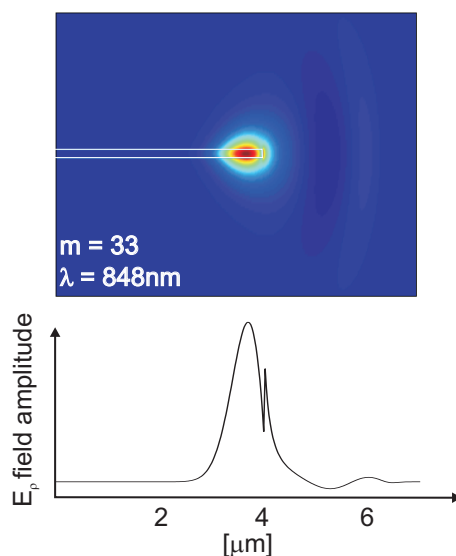


Figure 2.2: Electric field  $E_\rho$  of quasi-TE first order radial family computed with an FDTD algorithm. The dielectric structure is a 125nm thick, 8  $\mu\text{m}$  diameter disk of refractive index 2. Note the field discontinuity at the disk edge.

if the resolution of spatial discretization is large enough, it is possible to reproduce with a good reliability most of the experimental results.

### Micro-Photoluminescence characterization

Samples deposition and processing have been performed by M. Ghulinyan at Advanced Photonics & Photovoltaics, Fondazione Bruno Kessler (Trento - Italy). The deposition technique used was Plasma Enhanced Chemical Vapour Deposition (PECVD) (see, for example, [65]). In the standard procedure, a 100 - 300 nm SRSO layer is deposited on a crystalline silicon wafer. Post-annealing treatment at 1100  $^\circ\text{C}$  ensures the Si-SiO<sub>2</sub> phase separation with the full crystallization of the nanoparticles. Unless otherwise stated, the Si excess in the SRSO deposited material is 10 %  $\pm$  1. With lithographic patterning and wet/dry etching processes, array of several thousands of 8 - 12  $\mu\text{m}$  diameter disks are formed. In order to produce enough index contrast for light guiding, each disk is sustained in air by a 1  $\mu\text{m}$  high Si pedestal. Figure 2.3 reports Scanning Electronic Microscope (SEM) images of an array of identical disks (panel (a)) and the cross section of a single disk (panel (b)).

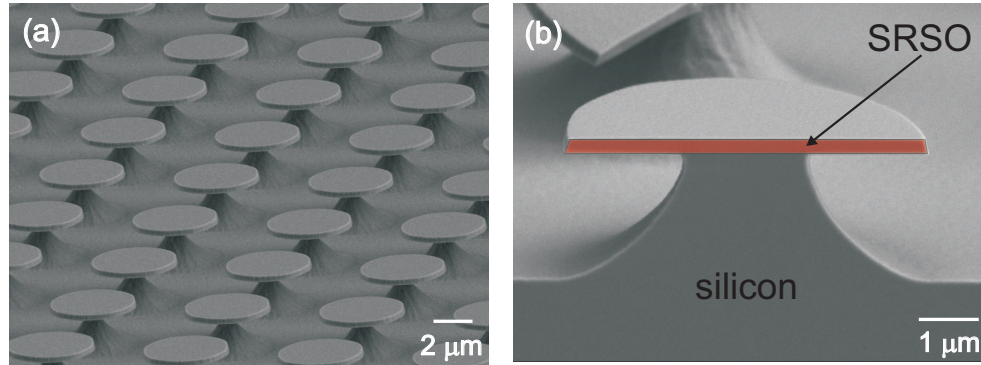


Figure 2.3: (a): SEM image of an array of identical microdisk resonators. (b) Cross section SEM image of a single microdisk.

PL characterization of the microdisk array has been performed, at first, with a

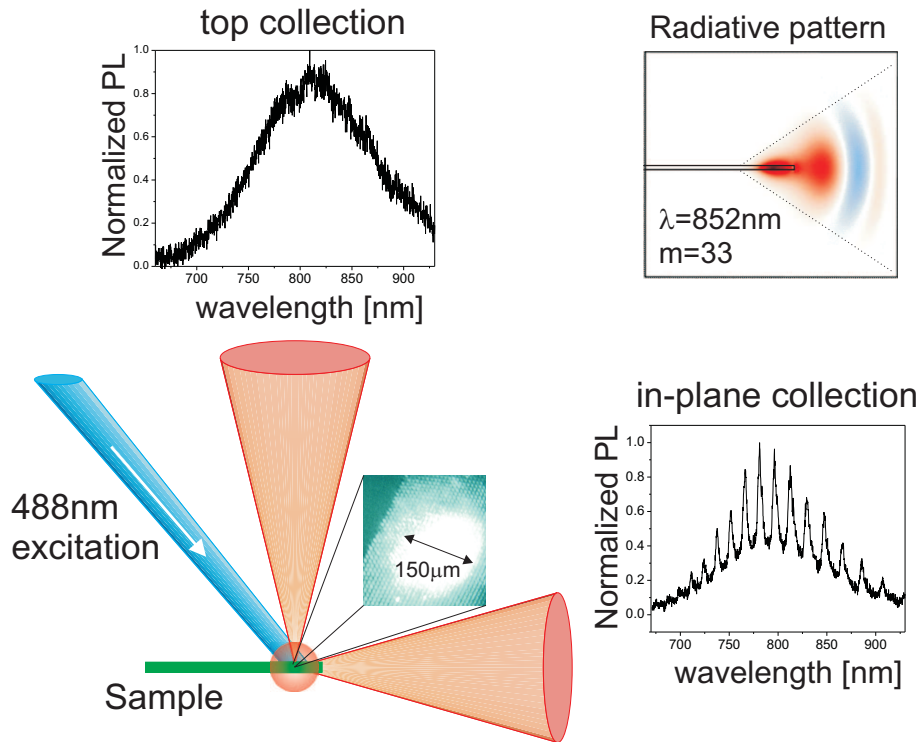


Figure 2.4: Schematic of the standard PL setup used to characterize the microdisk arrays. Relevant spectral features can be detected only when in-plane collection is used, confirming that the radiation pattern of WGM microdisk is essentially concentrated on the disk plane, as shown by the simulated optical field. The resonant mode found shows very low Q's ( $\sim 100$ ), limited by inhomogeneous broadening.

standard-PL setup. As can be inspected in fig. 2.4, the excitation spot is about  $150\ \mu\text{m}$  wide, resulting in the simultaneous excitation of thousands of different microresonators. When a large number of cavities is considered, statistical deviations in the disk geometry can not be neglected. This is the cause of inhomogeneous broadening of WGM which gives small-Q spectra ( $Q \sim 100$ ) when the PL intensity is collected

on the microdisk plane. Interestingly, when the signal is collected from the top, no spectral features due to resonant modes can be detected, confirming the planar nature of WGM mode, as sketched by the simulated optical field in fig. 2.4. Then, to overcome inhomogeneous broadening limitations, photonic characterization of the microdisks have been performed with a micro-PL experiments. A dedicated

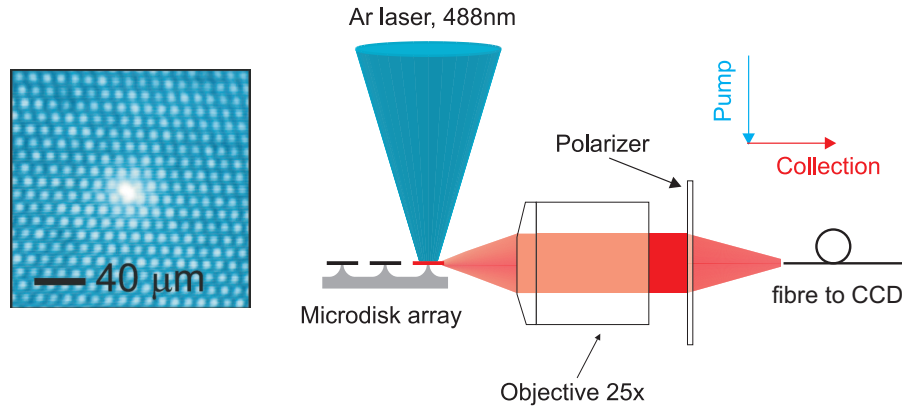


Figure 2.5: Schematic of the micro-PL setup.

setup has been built in which the excitation 488 nm laser line is focused through a 25× microscope objective on the top of the microdisk. Due to the strongly planar nature of WGMs, the collection has been performed using a 25× microscope objective mounted on a translational stage, which was focused on the disk edge, as schematically depicted in fig. 2.5. The signal is then collected through a fiber bunch and analyzed with a CCD camera coupled to a VIS-spectrograph or employing a GaAs-PMT coupled with a monochromator, with a maximum spectral resolution of 0.2 nm. Polarization resolved detection is performed placing a linear polarizer after the collection objective. The beam size of excitation line (with an area evaluated around  $10 \mu\text{m}^2$ ), allows the excitation of a *single* disk, without experiencing any inhomogeneous broadening due to multiple disk emissions. As mentioned in chapt. 1, excited Si-np emit in the visible in a broad band ( $\sim 200 \text{ nm}$ ) centered at 750 nm. The high crystalline quality of the samples ensures a strong photoluminescent emission, with an high quantum-yield. Moreover, a hydrogen passivation treatment (sintering), which has been employed for most of the samples under study, decreases the strenght of non-radiative recombinations, enhancing further the light emission effects [66]. The quasi-TE PL results for different diameter disks are reported in fig. 2.6. Clear lorentzian peaks appear with one order of magnitude Q increase with respect to the standard PL experiments of fig. 2.4. As expected, when the disk diameter is increased, both the Q's and FSR of the WGM mode is increased. Moreover, while in  $5 \mu\text{m}$  diameter disks only the first radial order mode is present, higher order modes appear in larger resonators. Due to their large Q and since the PL spectra are clear enough to grant an easy radial and azimuthal order mode analysis,  $8 \mu\text{m}$  disks have been chosen for a complete optical characterization. In fig. 2.7, the PL spectra of a bare SRSO film can be compared with the emission from a single, chosen resonator. In particular, the quasi-TE modes are investigated in microdisk with a thickness of 135nm. The refractive index of SRSO material is in this case

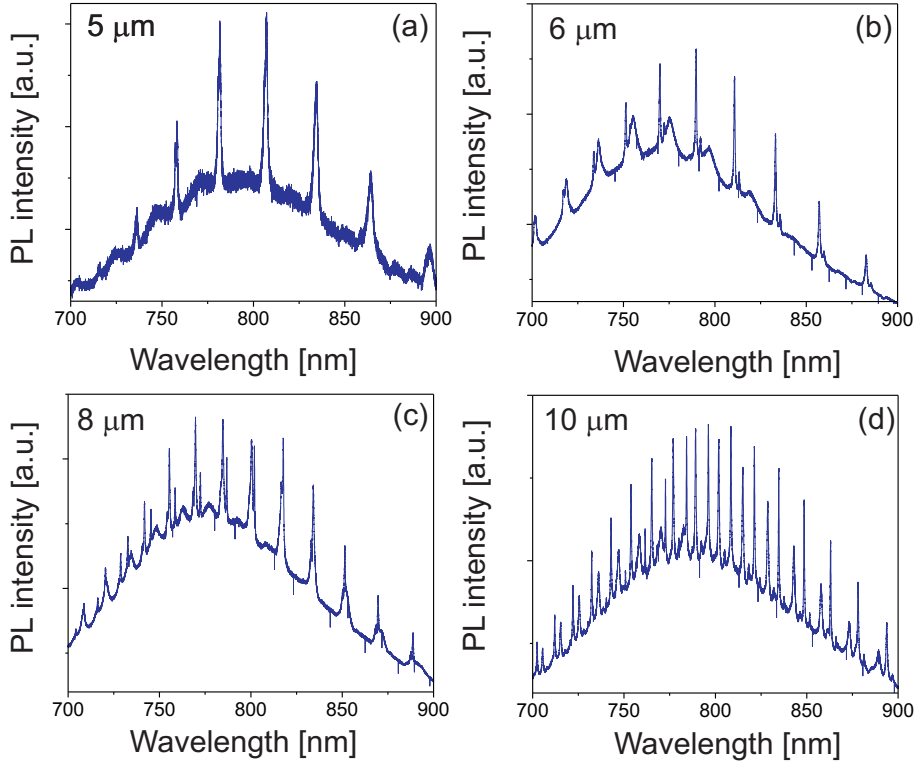


Figure 2.6: Quasi-TE micro-PL measurements in different diameter microdisks. 5  $\mu\text{m}$  (panel (a)), 6  $\mu\text{m}$  (panel (b)), 8  $\mu\text{m}$  (panel (c)) and 10  $\mu\text{m}$  (panel (d)) diameter resonators are considered.

equals to 1.8 at a wavelength of 800 nm. Clear, Lorentzian shaped peaks appear with an average FSR of 12 nm. The spectral positions of first radial order resonances have been simulated and are reported in fig. 2.7 (b), being in good agreement with experimental data. Even though simulations show that second radial order modes are supported, their intensity is expected to be much lower than the first order ones and are masked in the experimental spectrum.

It is worth to point out additional considerations regarding the quality factor of the cavity. The inverse of the total quality factor can be expressed as a sum of different contributions:

$$Q_{tot}^{-1} = Q_{rad}^{-1} + Q_{mat}^{-1} + Q_{scat}^{-1} + Q_{disor}^{-1} + \dots, \quad (2.6)$$

where each term accounts for a different loss channel:  $Q_{rad}$  indicates the losses that are due to the bended nature of the disk itself,  $Q_{mat}$  represents propagation losses within the material,  $Q_{scat}$  collects scattering-related loss terms due to possible inhomogeneities within the dielectric, while  $Q_{disor}$  is a general term of losses due to nanoscale-disorder effects. Clearly, different terms can be added up to the sum. It is possible, to a certain degree, to evaluate separately the loss contributions, in order to understand the main detrimental effects which limit the cavity quality factors.

Radiative Q's can be estimated directly from FDTD simulations. In particular, a useful harmonic filter diagonalization algorithm has been employed to get reliable Q values with moderate simulation running time [67]. Essentially the method concerns a Laplace-transform of decaying sinusoidal signals, such as the ones expected from

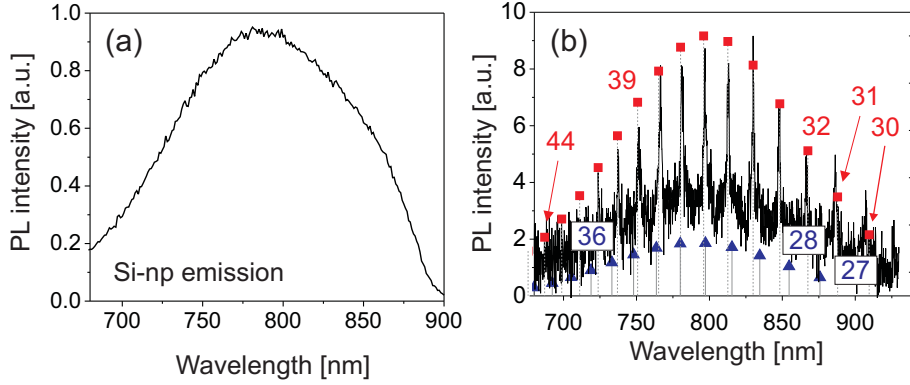


Figure 2.7: (a): PL emission from a bare SRSO thin film. (b): PL emission from the same active layer embedded in a 135nm thick, 8  $\mu\text{m}$  diameter disk. The FDTD-simulated first (squares) and second (triangles) radial families are reported.

cavity ring-down effects. The resonant frequencies and cavity lifetimes  $\tau_{cav}$  are then extracted directly from a specific fit of the data.

Absorption and material related scattering losses can be estimated by independent ellipsometric measurements on the material. From this technique it is possible to obtain both the real refractive index  $n$  and the imaginary extinction coefficient  $k$ . This is proportional to the loss coefficient  $\alpha$ , which gathers the loss contributions due to absorption and scattering (propagation losses, see sec. 1.3.2). In the visible range, the main source of losses for SRSO material is due to nanoparticles absorption, which is the main contribution to  $Q_{mat}$ . From  $k$  value, it is straightforward to get  $Q_{mat}$  as:

$$Q_{mat} = \frac{2\pi n_g}{\alpha \Gamma \lambda}, \text{ where } \alpha = \frac{4\pi k}{\lambda}. \quad (2.7)$$

Here,  $n_g$  is the group index,  $\Gamma$  the confinement factor and  $\lambda$  the vacuum wavelength. Figure 2.8 reports the evaluated and experimental value of  $Q$ 's for the SRSO disk under study. The same results have been found in most of the analyzed resonators. Employing only  $Q_{rad}$  and  $Q_{mat}$  one can easily get  $Q_{tot}$ , which has been found to be in good agreement with the measured one. In a first approximation, it is then possible to describe the quality factor dynamics of the resonators under analysis considering only  $Q_{rad}$  and  $Q_{mat}$ , neglecting the other terms which appear in eq. (2.6). Even though the radiative  $Q$ 's value could be easily increased considering larger diameter disks, the total  $Q$  will not change significantly due to the dominant absorption losses which depend on the material and not on the disk diameter.

The possibility to analyze Si-np dynamics within the resonator framework sounds appealing due to the possibility to extract useful material parameters with standard PL experiments, whereas complicated experiments are needed when the same material is used as waveguide active layer. In the following, a characterization of CCA losses for SRSO material is reported. In sec. 1.3.2 the physics of this phenomenon has been discussed and pump & probe experiments have been shown, where the CCA-loss coefficient was evaluated.

When SRSO material is embedded within an optical resonator, a dependence of  $Q$

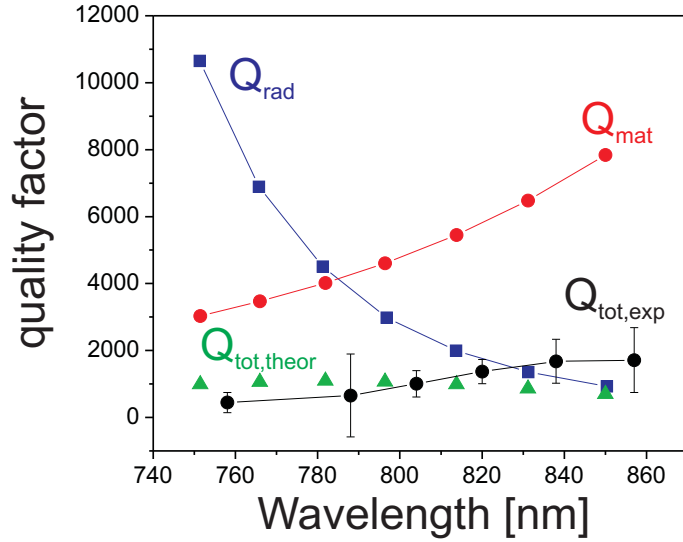


Figure 2.8: Calculated ( $Q_{rad}$ ,  $Q_{mat}$ ,  $Q_{tot,theor}$ ) and measured ( $Q_{tot,exper}$ ) Q's.

on the excitation photon flux can be observed. As discussed, the total Q can be expressed considering only the terms  $Q_{rad}$  and  $Q_{mat}$ . The first term is independent from excitation flux; the resonance spectral positions do not red shift even at the higher excitation intensity used, allowing one to neglect thermal dilatation of the dielectric. On the other hand, the term  $Q_{mat}$  depends on the excitation flux  $\Phi_{exc}$ ,

$$Q_{mat}(\Phi_{exc}) = \frac{2\pi n_g}{(\alpha_0 + \alpha^*)\Gamma\lambda}, \quad (2.8)$$

where  $\alpha_0$  and  $\alpha^*$  are respectively the loss coefficient independent and dependent from excitation flux. The latter can be expressed as a growing sigmoidal function,  $\alpha^*(\Phi_{exc}) \sim a\Phi_{exc}(1 + b\Phi_{exc})^{-1}$ , where a dominating Auger recombination has been assumed [68]. When the excitation intensity is increased,  $\alpha^*$  becomes larger and a reduction of Q is expected.

Indeed, fig. 2.9 (a) reports the measured Q's for selected resonances. For the lowest power a maximum Q of 3000 is reached. In fig. 2.9 (b), a fit of the inverse Q is reported using eq. (2.6) and (2.8). A good agreement between the fit and experimental data has been found. Moreover, extrapolating the fitted function to  $\Phi_{exc} = 0$ , an  $\alpha_0 \sim 32 \text{ cm}^{-1}$  can be extracted, which is the same as the one measured in ellipsometric experiments ( $\alpha_0 = 30 \text{ cm}^{-1}$ ).

The measured Q's are of the same order of the ones found in similar, III-V active resonators. As demonstrated, the main hindrance towards the achievement of larger quality factors is represented by the absorption loss of Si-np. Different solutions have to be considered to be able to improve cavity Q's. To this end, hybrid disk structures with passive/active materials are investigated, aiming both to the achievement of better Q's and to the study of novel physical effects.

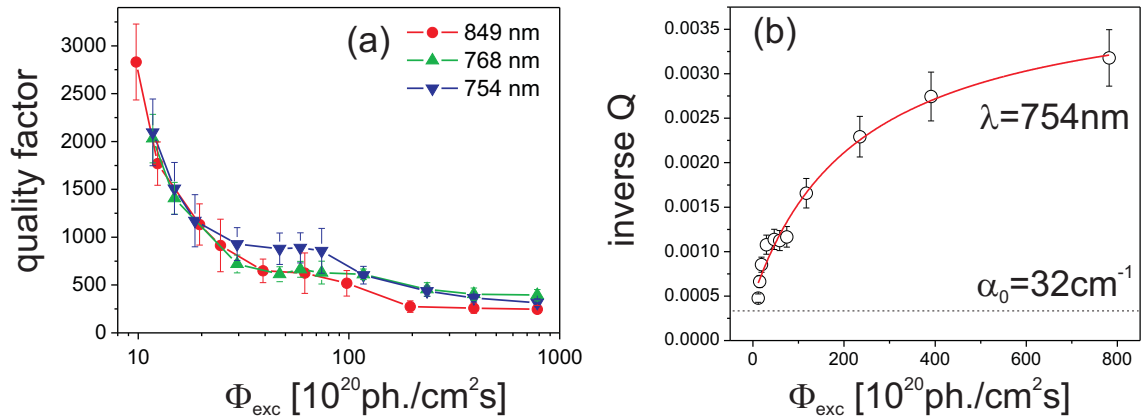


Figure 2.9: (a): Quality factors as a function of excitation flux. (b): inverse quality factor fit with eq. (2.6) and (2.8). The extrapolated at  $\Phi_{exc}$   $\alpha_0=32\text{ cm}^{-1}$  value is in close agreement with the ellipsometric one ( $30\text{ cm}^{-1}$ ).

### 2.1.1 Hybrid structure and strain engineering: kylix microresonators

The development of hybrid bilayer microdisk structures, which are constituted by passive and active materials, is one of the possible route to maintain the emitters within the cavity and, at the same time, to increase the Q's with respect to structures composed only by active materials. In general, the integration of different materials in the same dielectric structure is accompanied by material stresses at the interface, which eventually can be the cause of geometrical deformation of the global device, as well known in Micro-ElectroMechanical Systems (MEMS) related technology.

A novel approach concerns the exploitation of such deformations to tailor the optical properties of a microresonator. In the following, I will present an effort in this direction, showing a new class of WGM resonators (micro-kylix) in which the spectral region where the resonances with largest quality factors localize can be tuned of tens of nanometers.

#### Micro-kylix fabrication

The devices have been fabricated with the same technique described in sec. 2.1. A bilayer approach was used, depositing SRSO and silicon nitride  $\text{Si}_3\text{N}_4$  in different order and with various thicknesses for the different samples under study. Silicon nitride is practically transparent in SRSO emission region, decreasing the global absorption losses in the microresonator. Table 2.1 reports the compositions of the samples. In kylix samples, the deposition of  $\text{Si}_3\text{N}_4$  is performed at  $800^\circ\text{C}$ . At this temperature, the layer lattices are stress-free. When the sample cools down, the different sign of thermal expansion coefficients (negative in SRSO - tensile stress, positive for  $\text{Si}_3\text{N}_4$  - compressive stress), lifts the edge of the disk, creating a chalice-like shaped resonator. A schematic of the strained geometry can be inspected in fig. 2.10 (a). The measured stress at the material interface is of the order of  $-100\text{ MPa}$ , evaluated with a mechanical profilometer, while the edge raises with respect to the center of the disk by about  $300\text{ nm}$ . In inverted-kylix, the SRSO- $\text{Si}_3\text{N}_4$  deposition

| Sample                 | Top layer                       | Central layer | Bottom layer                    |
|------------------------|---------------------------------|---------------|---------------------------------|
| $\mu$ -disk            | $\text{Si}_3\text{N}_4$ - 50nm  | SRSO - 100nm  | $\text{Si}_3\text{N}_4$ - 50nm  |
| $\mu$ -kylix           | $\text{Si}_3\text{N}_4$ - 100nm | SRSO - 100nm  | -                               |
| Inverted- $\mu$ -kylix | -                               | SRSO - 100nm  | $\text{Si}_3\text{N}_4$ - 100nm |

Table 2.1: Layer thicknesses and material composition of flat ( $\mu$ -disk), bent-up ( $\mu$ -kylix) and bent-down (Inverted- $\mu$ -kylix) resonators. Both total and active material thickness are the same in all disks.

order is inverted, creating umbrella-like resonators, in which the edges lower with respect to the center of the disk. Moreover, since SRSO deposition temperature is lower than the  $\text{Si}_3\text{N}_4$  one, the degree of out-of-plane bending is less severe with respect to the standard micro-kylixes. In order to compare the different optical

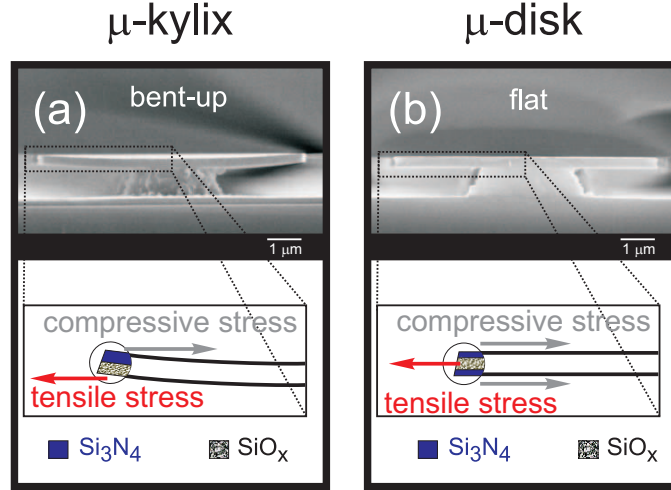


Figure 2.10: (a) SEM image and brief schematic of stresses in micro-kylix resonators. (b) The same for flat resonators.

properties, flat microdisks are created with a 3-layers approach, where top and bottom material strain can be compensated. It is worth to point out that the total thickness of this last structure is identical to the one of kylix and inverted kylix; in particular the active layer is exactly the same, while the passive layer has been divided in top and bottom layers, with a thickness which is half of the one in kylix resonators.

### Optical characterization and Q-band

Optical characterization of the strained resonators has been performed with the micro-PL setup, described in sec. 2.1. The PL spectra have then been analyzed, extracting the Q-values for the resonances belonging to the first radial order mode. To understand how the Q's are modified by the strained geometry it is necessary to recall some concepts presented in the previous section. Indeed, as shown in fig. 2.8, the dominating contributions to  $Q_{tot}$  ( $Q_{rad}$  and  $Q_{mat}$ ) have opposite trends with respect to the observation wavelength. Indeed, when these contributions are of the same order of magnitude, it is expected that  $Q_{tot}$  took the form of a bell-shaped

band, with the larger Q's localized in narrow spectral windows. With standard WGM resonator, the largest-Q-region can be shifted only modifying the disk radius (i.e. changing  $Q_{rad}$ ). If the desired shift is towards the blue, this causes a decrease of the total quality factors with an obvious modification of FSR. Kylix-microresonators allow a Q-band blue-shift of about 60 nm with a negligible change both in FSR (less than 1%) and in cavity Q's.

Figure 2.11 reports the PL spectra with the extracted Q's for a 10  $\mu\text{m}$  diameter micro-kylix and flat resonators. The absorption losses are less severe than full-

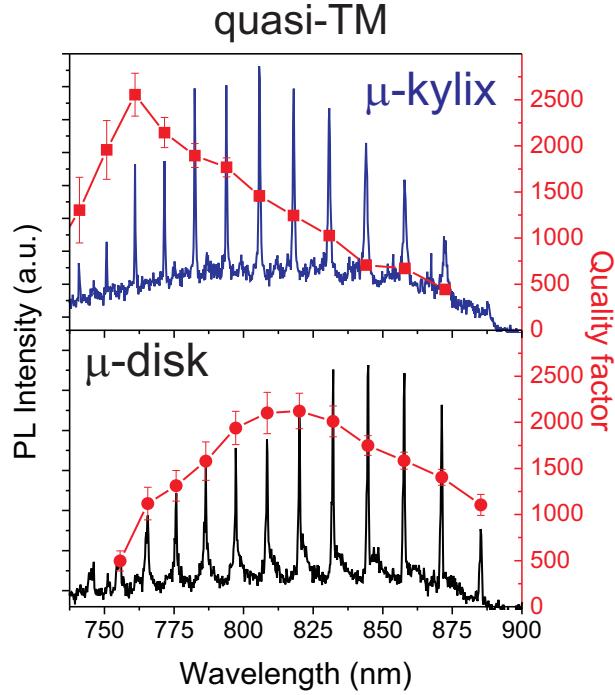


Figure 2.11: PL spectra of kylix and flat resonators. Superimposed the extracted Q-bands are reported.

active microdisks and, as expected, a Q-band is formed with a maximum at 823 nm and 762 nm for flat and kylix microdisks respectively. The total blue shift is about 60 nm with almost no change in the maximum measured Q of 2200. The physics behind the band shift is extremely simple and considers the simultaneous modification of both  $Q_{rad}$  and  $Q_{mat}$ . To simulate the effect, the modification of radiative and material losses have been considered independently and finally linked together, using eq. (2.6) to get the measured quality factors.

Radiative losses have been simulated using the harmonic inversion algorithm of the FDTD package which was described in sec. 2.1. In fig. 2.12 the main results are reported. Two kinds of modifications act on  $Q_{rad}$  in micro-kylix, which can be classified as in-plane and out-of-plane. The first are due to the reduced effective radius of 4.98  $\mu\text{m}$  which can be found in the micro-kylixes due to their cup-like shape. As can be inspected from the results in fig. 2.12, where *flat* disks of 5  $\mu\text{m}$  and 4.98  $\mu\text{m}$  radii are compared, this effect induces negligible change in the radiative quality factor values. On the other hand, when a out-of-plane bends is considered,  $Q_{rad}$

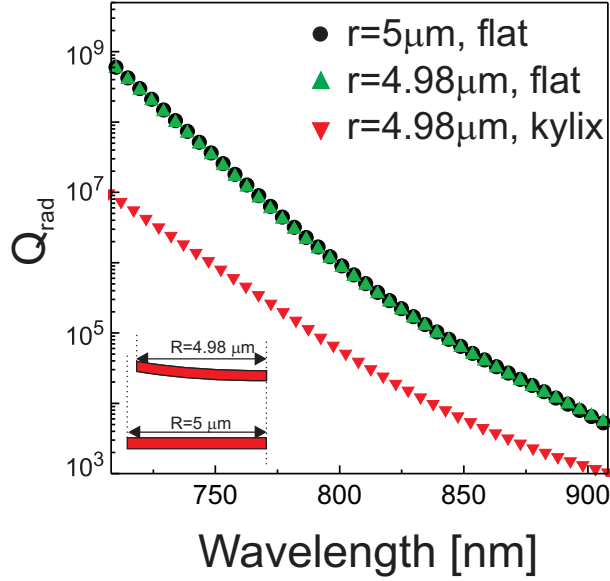


Figure 2.12: Simulated  $Q_{rad}$  for different disk resonators. The change in  $Q_{rad}$  is negligible when the flat resonator radius is modified from  $5\mu\text{m}$  ( $\bullet$ ) to  $4.98\mu\text{m}$  ( $\blacktriangle$ ), the latter representing the micro-kylix effective radius, as depicted in the scheme. When out-of-plane bend is inserted ( $\blacktriangledown$ ), the quality factor is reduced of about two orders of magnitude.

suddenly decreases of about two orders of magnitude, as shown when micro-kylix results are considered.

Material losses modification is more subtle. Recalling  $Q_{mat}$  expression of eq. (2.8), since the active material is the same, in the new geometry only  $n_g$  and/or  $\Gamma$  can be modified<sup>2</sup>. It is possible to obtain the group velocity in FDTD simulations considering that in a lossless medium (with real refractive index) this is equal to the energy velocity, using the following formula [69]:

$$v_g = \frac{\vec{P} \cdot \hat{z}}{u}, \quad (2.9)$$

where  $\vec{P} = \vec{E} \times \vec{H}$  is the Poynting vector,  $\hat{z}$  the electromagnetic wave propagation direction and  $u$  is the density of electromagnetic energy,  $u = \epsilon/2|\vec{E}|^2 + \mu/2|\vec{H}|^2$ . From FDTD simulations of the passive structures (i.e. without absorption), a group index of 2.02 and 2.12 at 800 nm has been found respectively for flat and kylix microresonators. This means a  $Q_{mat}$  modification of only 5%, which is not enough to explain the observed experimental shift. More interesting is the modification of the confinement factor ( $\Gamma$ ) inside the active SRSO region. When slab waveguides with the same multilayer structure of tab. 2.1 are considered, no apparent modification of  $\Gamma$  can be appreciated, as reported in fig. 2.13 (d). Conversely, when  $Q_{mat}$  is

<sup>2</sup>It is assumed that strain related effects, which in principle could modify  $\alpha$ , are not present in the structure. In fact the edge region of the disk, where the first radial order modes under investigation propagate, is stress-free, whereas the residual stress should concentrate in the region close to the pedestal.

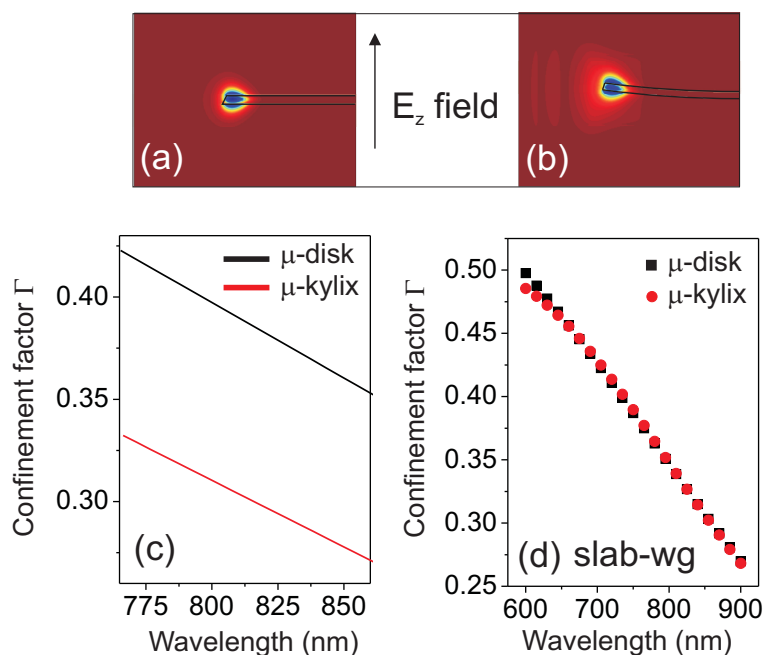


Figure 2.13: (a): FDTD-simulated quasi-TM field for the flat resonator at 800nm. (b): The same for kylix resonators. (c): Optical confinement factor calculated in flat and kylix microresonator. Note the appreciable modification which is induced by the cup-like kylix shape. (d): Optical confinement factor in slab waveguides with the same multilayer structure of flat and kylix resonator, reported in tab. 2.1.

simulated directly for the real devices, of which the fields are reported in fig. 2.13 (a) and (b), a large difference appear. Fig. 2.13 (c) reports the final results, with about a factor 3 increase in the material quality factor values of micro-kylix with respect to flat micro-disk.

With the simulated  $Q_{rad}$  and  $Q_{mat}$ , the total  $Q$  can be calculated, considering an additional constant term  $Q_{dis}$ , to reproduce the measured  $Q_{tot}$  values. Fig. 2.14 (a) reports the final results. The simulations are in qualitative agreement with the observed experimental behavior, where a  $Q$ -band shift of  $\sim 50$  nm has been simulated<sup>3</sup>.

Figure 2.14 (b) reports the comparison of  $Q$ -band of different resonators. As discussed above, inverted-kylix possess a less degree of bending with respect to standard, upwards one, and consequently, the maximum of the band localizes in the middle between micro-kylix and flat resonators. It is worth to note that it is possible to blue shift the  $Q$ -band by the same value achieved by kylix resonators employing a  $5 \mu\text{m}$  diameter flat resonator. In this case it is possible to observe a threefold decrease of the total quality factor of the resonator.

Indeed the possibility to tune the quality factor band is appealing, but a dynam-

<sup>3</sup>Since the simulations have been performed interpolating the curves representing  $Q_{rad}$  and  $Q_{mat}$ , the discretization effect induced by the resonances can improve the simulated results towards larger  $Q$ -band shifts.

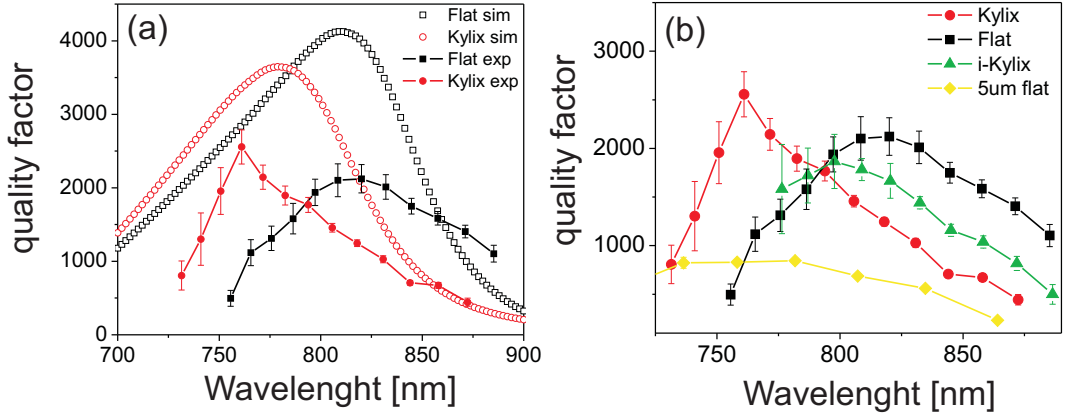


Figure 2.14: (a): Comparison between simulated and experimental Q-bands for kylix and flat resonators. (b): Comparison of experimental Q-bands for several resonators, kylix (●), 10- $\mu\text{m}$  flat (■), inverted-kylix (▲) and 5- $\mu\text{m}$  flat (◆).

ical tuning would be needed to employ such resonators in complex devices. Several possibilities arise to obtain this result. For example, this could be achieved considering piezo-electric materials, in which the geometrical aspect can be exactly controlled by external currents. More intriguing it is the feasibility of an all-optical tuning, which could be developed in the context of opto-mechanics [70], where optical forces realize a precise control of the geometric structure of the resonators [55, 56]. In sec. 2.2 some numerical analysis are presented for a vertical-coupled geometry in which the kylix could be implemented to dynamically tune the Q-band with all-optical means.

## 2.1.2 Purcell effect

The radiative rate of a two-level system  $|i\rangle, |f\rangle$  is described by Fermi's golden rule (see, for example [71]):

$$\Gamma_{f \rightarrow i} = \frac{2\pi}{\hbar} |\langle i | H' | f \rangle|^2 \rho(\omega), \quad (2.10)$$

where  $H'$  is the interaction Hamiltonian and  $\rho(\omega)$  is the photonic density of states at the transition frequency,  $\hbar\omega = E_f - E_i$ . This simple expression has been obtained with the first order perturbation theory and thus is valid in the limit of weak-coupling regime, that is when light and matter can be treated as separated, yet interacting entities.

While the Hamiltonian matrix element depends only on the emitter nature, the photonic density of states (DOS) can be strongly modified by the surrounding dielectric environment. Indeed, one of the motivation behind the introduction of photonic crystal structures was the possibility to control spontaneous emission rate when certain photonic features are centered at the emitter frequency [72]. Even though the physics of photonic crystals will be described in chapt. 3, it is instructing to consider a simple 2D square lattice of air holes in a Si layer which is infinitely extended with periodicity  $\Lambda$ . At this level it is sufficient to mention that a photonic crystal is a dielectric material in which the photons are subjected to periodic potentials,

similarly to electrons in crystal lattices. In analogy with the latter, it is possible to describe the photon states in terms of energy bands in the reciprocal space. Figure 2.15 reports the dielectric (first) and air (second) bands of the structure together with their density of states. Some features can be observed. In the photonic band

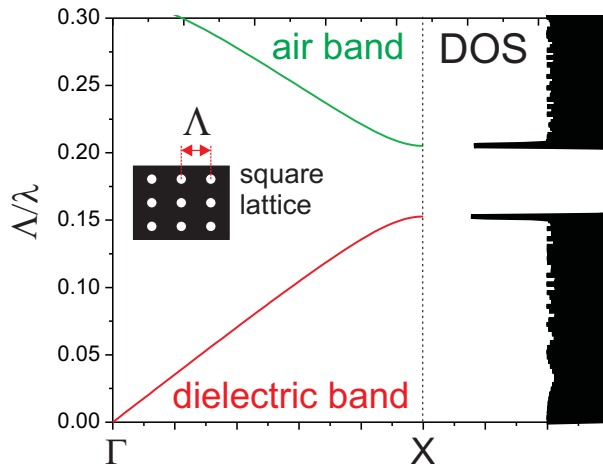


Figure 2.15: Photonic bands and density of states (DOS) for a square lattice 2D photonic crystal. Only the fundamental gap between the first (dielectric band) and the second band (air band) is reported. Note that the DOS is zero inside the gap while it is peaked close to the band edges.

gap, the DOS is zero, completely quenching the radiative rate  $\Gamma$ . On the other hand, at the band gap edges the DOS is peaked, reaching values which can be very large with respect to the one in bulk material. According to eq. (2.10), it is then expected that an emitter spectrally tuned with these peaks is subjected to an enhancement of its radiative emission rate. The same DOS increase can be observed for resonant cavity modes, such as WGM. Indeed, the expected enhancement has been observed by Purcell [53] in the 40's, for resonant atomic transition at radiofrequencies. In the last years, the same effect has been reported for III-V Quantum Dots (QDs) at optical wavelengths in dielectric microresonator [73].

The expected enhancement  $F_P$  can be readily estimated, for an ideal system, considering the increased DOS for a cavity resonant mode,  $\rho_{cav} = 2Q/\pi\omega_c$  with respect to the standard 3D one in an homogeneous material of index  $n$ ,  $\rho_{bulk} = \omega^2 V n^3 / \pi^2 c^3$ , leading to the well-known final expression:

$$F_P = \frac{3}{4\pi^2} \left(\frac{\lambda}{n}\right)^3 \frac{Q}{V}, \quad (2.11)$$

where  $V$  is the so-called mode volume, which is defined as:

$$V = \frac{\int n^2 |\vec{E}(\vec{r})|^2 dV}{\max[n^2 |\vec{E}(\vec{r})|^2]}. \quad (2.12)$$

Unfortunately, this expression holds only for ideal cavity-emitter systems, which is realized when the following conditions are fulfilled:

- Emitter homogeneous linewidth has to be narrower than the cavity linewidth.
- Emitted photons have to be spectrally tuned with and have to be in the same polarization state of the resonant mode.
- Emitter has to be placed in a field antinode.
- Non-radiative emission rate has to be negligible.

Otherwise, the so-called *bad-emitter-regime* is realized, where a Purcell effect can still be probed, though greatly reduced with respect to the ideal case. Eq. (2.11) represents a figure of merit of the cavity itself and has to be promptly corrected to take into account the non-ideal terms abovementioned. The non-ideal Purcell factor,  $\tilde{F}_P$ , which accounts for the first three points in the list is given by:

$$\tilde{F}_P = \frac{3}{4\pi^2} \left(\frac{\lambda}{n}\right)^3 \frac{Q_{eff}}{V} \frac{\Delta\omega_c^2}{\Delta\omega_c^2 + 4(\omega - \omega_c)^2} \frac{|\vec{E}(\vec{r})|^2}{|\vec{E}|_{max}^2} \eta^2, \quad (2.13)$$

where  $\Delta\omega_c^2/(\Delta\omega_c^2 + 4(\omega - \omega_c)^2)$  is the resonance-emitter spectral detuning and  $|\vec{E}(\vec{r})|^2/|\vec{E}|_{max}^2$  is a spatial correction term.  $\eta^2$  accounts for non-polarized emitters and finally,  $Q_{eff}$  takes into account emitters with broad linewidths. The latter is indeed an effective quality factor, defined as  $Q_{eff}^{-1} = \Delta\omega_{cav}/\omega_{cav} + \Delta\omega_{em}/\omega_{em}$ , with the first term cavity quality factor. The second term includes the emitter linewidth ( $\Delta\omega_{em}$ ) and central emission ( $\omega_{em}$ ) and represents a sort of *emitter quality factor* [74].

Figure 2.16 reports all the elements which are necessary to calculate the ideal Purcell factor for the kylix and flat resonators under study. The extracted values reach a maximum value of 20, although, as discussed, the real enhancement strongly depends on the emitter nature. Indeed, Si-np represent a peculiar emitter, since their optical properties still lack precise analysis and measurements, with some debate still ongoing about the origin of PL emission. In the following, some discussion on the different hypothesis is reported.

### Photoluminescence emission in Si-np

The first luminescence from nanostructured silicon was observed in porous (pSi) samples [75], igniting a intense research towards the understanding of the physical phenomenon. Indeed, when low-temperature PL measurements are concerned, this material displays particular effects which can not be found in standard, light-emitting semiconductors. As observed in fig. 2.17 (taken from [76]), the emission behavior is different when the temperature high (I) or low (II) temperature ranges are considered. In the first region, the non-radiative recombination mechanism dominates the PL lifetime and intensity, which can be described as:

$$\begin{aligned} \tau_{PL} &= \frac{1}{\Gamma_{nr} + \Gamma_r}, \\ I_{PL} &\propto \frac{\Gamma_r}{\Gamma_{nr} + \Gamma_r}. \end{aligned} \quad (2.14)$$

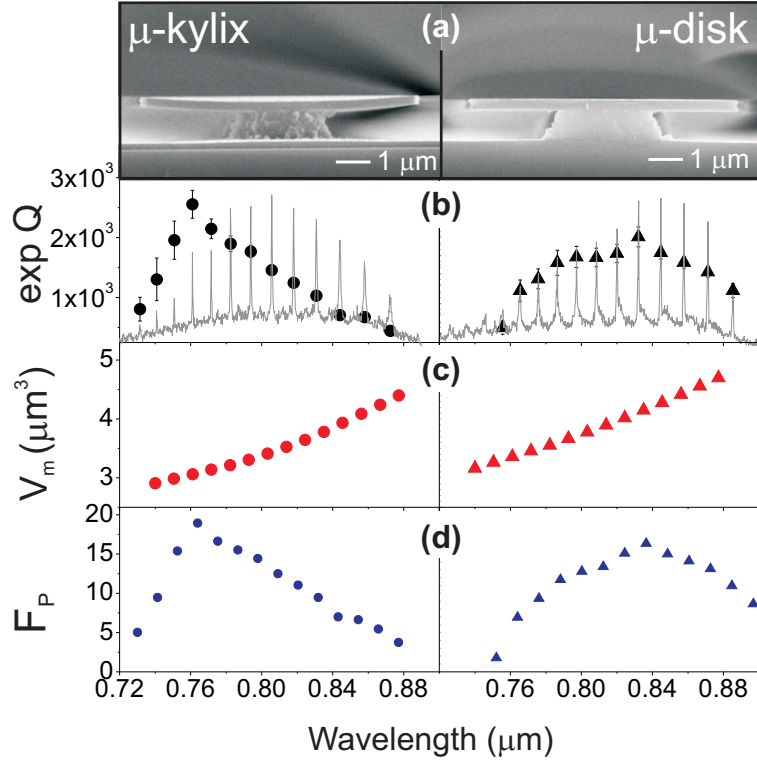


Figure 2.16: (a): SEM images of microkylix and flat microdisk resonators. (b): PL spectra and Q-bands. (c): Mode volumes. (d): Ideal Purcell factor.

Essentially, when the temperature is decreased, non-radiative rate  $\Gamma_{nr}$  is reduced with a concomitant enhancement of both  $I_{PL}$  and  $\tau_{PL}$ . On the other hand in region II, while the lifetime monotonically increases, PL intensity weakens when a temperature reduction is realized. This behaviour has been explained by Calcott [77], considering an exchange-interaction splitting of the exciton level in a triplet and singlet states, as reported in the scheme of fig. 2.17. Even if the level splitting is only of a few tens of meV, they are characterized by different oscillator strength, since the singlet recombination is an allowed dipole transition while the triplet one is forbidden. The lifetime can then be described by a temperature-averaged sum:

$$\tau_r^{-1} = \frac{3\tau_{tri}^{-1} + \tau_{sin}^{-1}e^{-\Delta/kT}}{3 + e^{-\Delta/kT}}, \quad (2.15)$$

with  $k$  Boltzmann's constant and  $\tau_{tri}$  ( $\tau_{sin}$ ) triplet (singlet) recombination lifetimes. When  $T$  is large enough a fast thermalization between the levels is possible, with a dominating singlet transition. On the other hand, for  $kT < \Delta$ , the triplet transition starts to dominate, with a resulting lengthening of  $\tau_{PL}$ .

This very same model has been recently applied to Si-np, where the singlet and triplet recombinations have been respectively attributed to quantum-confined and surface-related PL [25, 78]. It is clear that the usual low-temperature PL measurements, in which optical constant are usually evaluated, are meaningless in Si-np, since a different, triplet transition is probed, with respect to the dominating, singlet one at room temperature.

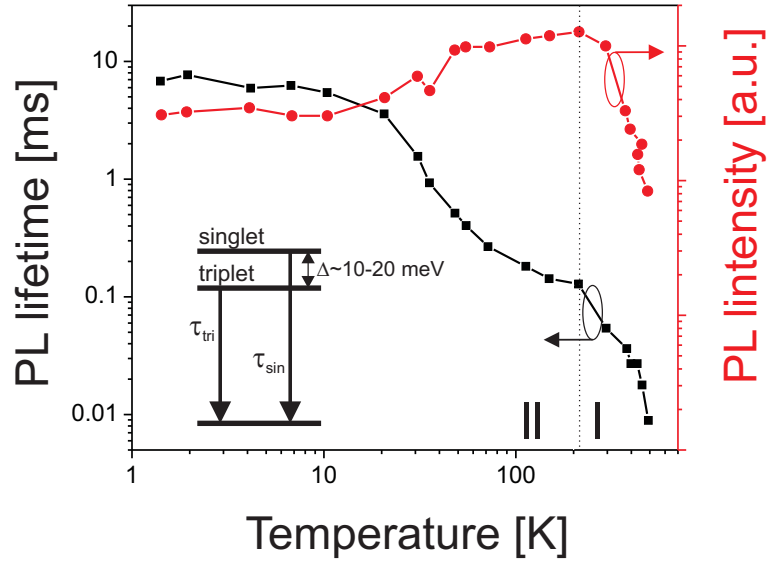


Figure 2.17: PL intensity and lifetime as a function of the temperature. Note the different trends in regio I and II. From [9]

Even if it is assumed that Si-np are bad emitter for Purcell enhancement observation, it is still possible to measure a modification of the spontaneous emission rate when the particles are embedded within a cavity. Inverting eq. (2.13), it is then possible to obtain information about optical constants, such as emitter linewidths, from the measured enhancement value.

In the following, an estimation of  $F_P$  for Si-np embedded in microdisk resonators is reported. Moreover, comparing theoretical and experimental results the Si-np linewidth  $\Delta_{em}$  can be indirectly estimated.

It is worth to note that often, the Purcell enhancement is estimated as the ratio of measured PL intensities from a cavity resonance and the bulk material. Even if the PL intensity is directly proportional to the radiative recombination rate, this approach, however, results in strongly overestimated  $F_P$ 's; geometrical correction effects have to be taken into account when the WGM cavity emission (usually within a small solid angle) and the bulk emission (isotropic) are compared [79]. The degree of uncertainty by which the correction factors can be estimated, allows to extract Purcell enhancement only by comparing lifetimes for an emitter coupled and for an emitter not-coupled (uncoupled) with a cavity mode, as previously done for III-V quantum dots in [73]. Figure 2.18 (a) schematically reports the contribution of PL emission of coupled and uncoupled photons. Indeed, when cavity photons are probed, a background emission coming from photons coupled to leaky mode can be detected, as shown in a detail of PL spectrum reported in panel (b). In fig. 2.18 (c) a *visibility parameter*  $A$  is calculated, as the peak to dip intensity ratio. A large visibility parameter means that most of the collected radiation comes from emitter whose photons are coupled with a WGM mode.

The PL lifetimes have been measured through time-resolved experiments using the 488 nm line of a kHz-modulated CW laser source. At first, lifetimes in spectral

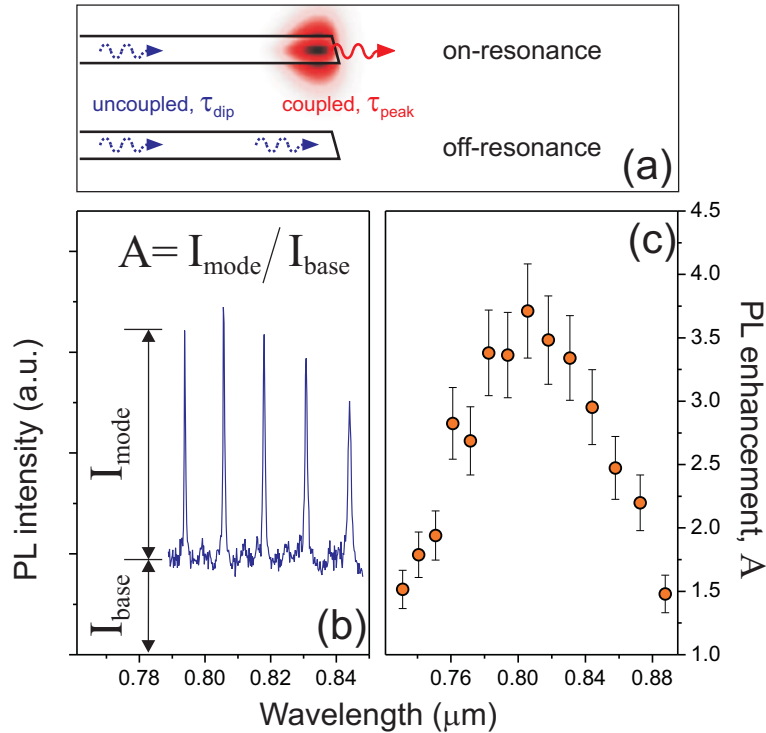


Figure 2.18: (a): Graphical sketch explaining the use of exponential decay functions for on- and off resonance conditions. (b): Detail of a PL spectrum of the microdisk resonator. (c): The visibility parameter  $A$  which has been employed in eq. (2.16), defined as the PL intensity ratio of the WGM,  $I_{mode}$ , and the background,  $I_{base}$ . The extracted values of  $A$  are from the PL spectra of fig. 2.16

dips between neighboring WGM resonances have been measured. There, the excitons are considered to be uncoupled to any cavity mode. The decays have been fitted by a stretched exponential function (see eq. 1.4). In this case, it does not account only for inter-particle hopping phenomena of excitons in Si-nps [21], but an emission/detection frequency detuning effects contributes to the decay distribution, as will be discussed in the following. The stretched exponential represents a distribution of decays with different lifetimes (Kohlrausch-Williams-Watts (KWW) distribution). The parameters  $\tau$  and  $\beta$  allow to extract the average PL lifetime as the first order moment of the distribution,  $\tau_{PL} = \tau/\beta G[1/\beta]$ , as reported in eq. (1.4). The PL lifetimes at cavity peak wavelengths have to be treated with greater care. Since the emitters are uniformly distributed in the resonator, the PL emission from peaks results from a contribution of (i) photons coupled to the cavity mode and (ii) a background signal of emitters uncoupled to the WGMs (leaky contribution), as described in fig. 2.18. In this scheme, the decays have been fitted employing the expression:

$$\frac{I(t)}{I_0} = A e^{-[(t-t_0)/\tau_{peak}]^\beta} + e^{-[(t-t_0)/\tau_{dip}]}, \quad (2.16)$$

where the value used for  $A$  are reported in fig. 2.18 (c). In (2.16),  $\tau_{peak}$  is the lifetime of mode-coupled emitters, while  $\tau_{dip}$  represents the average lifetime at the peak wavelength extracted from interpolated  $\tau_{PL}$  data for dips (and, thus, represents

the uncoupled emitters lifetime). Figure 2.19 reports an example of measured peak

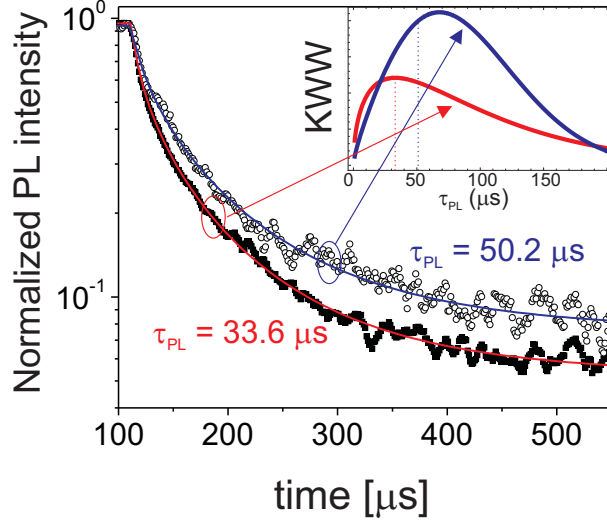


Figure 2.19: Measured out-of-resonance (full squares,  $\lambda = 853$  nm) and on-resonance (empty circles,  $\lambda = 846$  nm) PL signals. The data have been fitted using single and double stretched exponential decays, respectively. The inset shows the KWW distributions derived from fit parameters.

and dip lifetimes, where important differences can be appreciated. In the inset, the extracted KWW distribution curve, with the corresponding average PL lifetime (dashed lines) is reported. The extracted lifetimes at various resonances and dips in a wide spectral range are summarized in fig. 2.20.

Before addressing the Purcell enhancement, it is worth to consider the implication of stretched exponential decay in the conditions of bad emitter regime. For simplicity, neglecting the non-radiative recombination rates, one can write the total emission rate from a single nanocrystal at the frequency  $\omega$  as:

$$\Gamma(\omega) = \Gamma_r [1 + Af(\omega)\tilde{F}_P\delta(\omega - \omega_{cav})], \quad (2.17)$$

where the function  $f = \frac{\Delta\omega_{em}^2}{\Delta\omega_{em}^2 + 4(\omega - \omega_{cav})^2}$  describes the spectral detuning of the emitter from the cavity resonance. In the bad emitter regime, the latter has been considered as a Dirac  $\delta$ -function. With this result the PL-decays of an ensemble of  $N$  emitters, each one characterized by its own frequency  $\omega_i$  and radiative rate  $\Gamma_i$ , can be described as the sum:

$$I_{PL}(t) = \sum_i^N \frac{\Delta\omega_{em}^2}{\Delta\omega_{em}^2 + 4(\omega - \omega_i)^2} (1 + A\delta(\omega_i - \omega_{cav})) e^{-\Gamma_i t}. \quad (2.18)$$

Eq. (2.18) tends to a stretched exponential decays with different sets of  $(\tau, \beta)$  depending on the detection frequency (spectral dip or peak). The spectral detuning effects, in fact, are included in the KWW distribution parameters and thus are already considered during the fitting procedure of PL-decays. Note that when Eq. 2.18 is resolved *a posteriori* with the estimated in this thesis linewidth,  $\Delta\omega_{em}$ , a larger  $\beta$  ( $\tau$ ) is extracted for the dip frequency with respect to those at the peaks. This has

been verified for all our experimental data. This finding further confirms the presence cavity-related dynamics, strengthening the proposed model. It is important to point out that the stretched exponential decay is a peculiarity of the bad emitter regime, whereas in the limit of  $\Delta\omega_{em} \ll \Delta\omega_{cav}$ , such as in the case of III-V quantum dots, usually single exponentials are observed [73].

Regarding the experiment, at room temperature, the non-radiative recombination rate can not be neglected. Therefore, the ratio  $\epsilon = \tau_{dip}/\tau_{peak}$ , has been measured. This is a function of radiative,  $\tau_r$ , and non-radiative lifetimes,  $\tau_{n-r}^{-1} = \tau_{dip}^{-1} - \tau_r^{-1}$ , which can be read as,  $\epsilon = 1 + \frac{\tau_{dip}}{\tau_r}(\tilde{F}_P - 1)$ . In this particular case, the non-ideal Purcell factor  $\tilde{F}_P$  has been estimated from empirical considerations following the general procedure described in [74]:

$$\tilde{F}_P = g \frac{3}{4\pi^2} \frac{\tilde{\lambda}^3}{V_m} \left( \frac{1}{Q_{cav}} + \frac{\Delta\omega_{em}}{\omega_{em}} \right)^{-1} f(\langle\omega\rangle), \quad (2.19)$$

where the clockwise-anticlockwise mode degeneracy,  $g$ , has been considered ( $g = 2$ ). Spatial and polarization averaging effects have been evaluated employing eq. (2.16), where the contribution from leaky modes has been eliminated [73]. Note that the experimentally determined fitting coefficient  $A$  in eq. (2.16) is proportional to  $\langle \cos(\theta)^2 \rangle$ , where  $\theta$  is the angle between the unpolarized Si-np dipole emission and the polarized TM-like WGM. Therefore,  $A$  takes into account the correction factor for polarization mismatch. While the spectral detuning effects are already included in the  $(\beta, \tau)$  set of the stretched-exponential distribution, in eq. (2.19) an additional Lorentzian-shaped term [73] has been considered,  $f(\langle\omega\rangle)$ , and averaged for the finite spectral resolution of the detecting system.

While the difference between peak and dip lifetimes is appreciable, the resulting ratio  $\epsilon$  is slightly larger than unity (fig. 2.20 (b)), with a maximum relative shortening  $(1 - \epsilon)$  of about 70 %. Note that  $\epsilon$  represents the lower limit of  $\tilde{F}_P$  when non-radiative recombination rates are non-negligible, as in this case. On the other hand, when  $\Gamma_{n-r} \rightarrow 0$ , the values of  $\epsilon$  and  $\tilde{F}_P$  coincide ( $\lim_{\tau_{n-r} \rightarrow \infty} \epsilon = \tilde{F}_P$ ). In the expression for  $\epsilon$ , the radiative lifetime has been attributed to the singlet state [78]. In fact, the  $H_2$ -passivation step which has been used in the investigated samples is known to quench the triplet state recombination rate in Si-nps, [25]. Comparing  $\epsilon$  and  $\tilde{F}_P$ , effective linewidths have been extracted ( $\sim 10$  meV) for spontaneous emission enhancement (fig. 2.20 (c)).

The effective linewidth describes the average nanocrystal/resonant-cavity-field coupling, and is expected to be of the same order of Si-np's homogeneous electronic linewidth. The literature does not report any data for this last in PECVD-grown Si-nps, therefore, the results are discussed considering other material systems containing Si-np. It is known that due to their reduced size, Si-np can show breakdown of  $\vec{k}$ -conservation rule in optical transitions [8]. Indeed, for high quantum confinement energies, the No-Phonon (NP) quasidirect transition probability starts to rule out the Phonon-Assisted (PA) indirect one, which represents the main radiative recombination path in bulk Si. While PA transitions show temperature-dependent linewidth broadening, NP transitions are considered energetically sub-natural (nar-

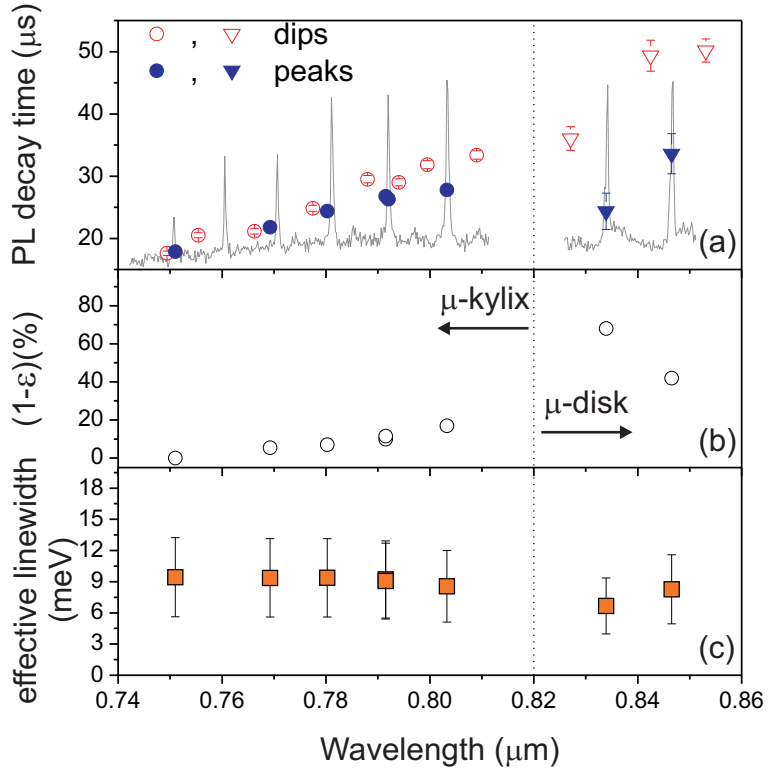


Figure 2.20: (a): Measured peak and dip lifetimes in micro-kylix and micro-disk resonator, using the procedure described in the text. The extracted lifetime enhancement  $\epsilon$  is reported in panel (b), where a maximum of 70% has been found. (c): Extracted effective linewidth  $\Delta\omega_{em}$ .

rower than  $kT$ ) [80]. This has been confirmed in low-temperature spectroscopic experiments on tens of nm-sized single Si-nanopillars [80], where a 2 meV narrow linewidth at 35 K has been measured. As predicted in ref. [8], the NP to PA transitions ratio should be even stronger in SiO<sub>2</sub>-embedded Si-ncs of a few nm in size with respect to nanoparticles obtained from mesoporous Si oxidation ( $\sim 10$  nm). In addition, quenching of the triplet state recombination through  $H_2$ -passivation should cause a further narrowing of the linewidth.

A measured linewidth of 10 meV corresponds to *emitter Q factors*,  $Q_{em} = \omega_{em}/\Delta\omega_{em}$ , of the order of 200. These Q's impose an upper limit on the cavity linewidth which can be efficiently exploited to couple Si-nps to resonator modes. Larger Q-factor does not affect the radiative lifetime but simply filter out the emission. However, the Purcell enhancement can be still favored by a small mode volume of the cavity [51] (in the resonators here analyzed, for example,  $V_m \sim 25\tilde{\lambda}^3$ ). Utilizing ultras-small mode volumes ( $V_m \sim \tilde{\lambda}^3$ ), such as those of photonic crystal nanocavities [81], Purcell enhancements of  $\tilde{F}_P \sim 25$  can be expected.

## 2.2 Vertically coupled passive microresonators

Though interesting for different applications such as biosensing and light emission/amplification, in active microdisk hindrances imposed by the absorption losses forbid the achievement of large Q's. Indeed, passive WGM microresonators can reach Q as high as  $10^9$  [49], which are comparable with the best photonic crystal planar nanocavities [81]. Anyhow, Q values of  $10^4 - 10^5$  are sufficient to observe interesting and new physical phenomena [52, 82].

The most immediate consequence to have large quality factors is the possibility to store a large fraction of electromagnetic energy within the resonant mode. This is suitable for nonlinear optics experiments, and Optical Parametric Oscillations (OPO) regime has been recently reported in Si-based WGM resonators [83, 84]. Moreover, if two spatially separated yet coupled resonators are considered, new physics, such as non-equilibrium optical Josephson-like oscillations can be observed. In the following, I will report some simulations towards a realization of vertically-coupled passive microdisk resonators. Using Si-np non-linearity [61], this geometry seems promising to observe the abovementioned oscillation regime, which will be discussed as a possible future perspective.

Photonic properties of passive devices are usually probed via a mechanically-pulled tapered fiber, in which the diameter is reduced to few  $\mu\text{ms}$  [85]. A schematic of the measurement is reported in fig. 2.22 (a). When light passes through the pulled region, if phase-matched with a WGM resonance, can evanescently couple to the cavity mode. The fiber transmission spectrum shows lorentzian-shaped dips when the light is coupled into the resonator. From these, the Q-factor can be evaluated with eq. (2.2). As preliminar stage, single  $\text{Si}_3\text{N}_4$ , 50  $\mu\text{m}$  diameters, 135 nm thick microdisks have been investigated in the IR range. Note that in the near-infrared spectral region under analysis  $\text{Si}_3\text{N}_4$  material is transparent, and thus does not contribute to the Q-factor degrading via absorption mechanism. Figure 2.21 shows a typical transmission measurement of the sample under investigation. Sub-nanometric features appear, with a Q-factor of the order of  $10^4$ . The best result obtained was of 97000 (not shown). With Q's of this order of magnitude, interesting phenomena can be observed, such as optical dipole forces [82] and strong coupling [86].

Particularly interesting is the possibility to couple two microdisks vertically aligned, as in the scheme of fig. 2.22 (a). If the disk-to-disk distance is low enough, the eigenmodes localized in each resonators overlap significantly, in analogy to what happens for wavefunctions in a double-well potential. It is a well known fact that the states perturb each other via tunneling effect, which splits the wavefunction in a symmetric and anti-symmetric state, similarly to what happens for the orbitals of diatomic molecules, like in  $\text{H}_2$  [71].

Considering the electromagnetic fields within the cavity as the sum of two modes (2-modes approximation), it is possible to express the equation of motion for the

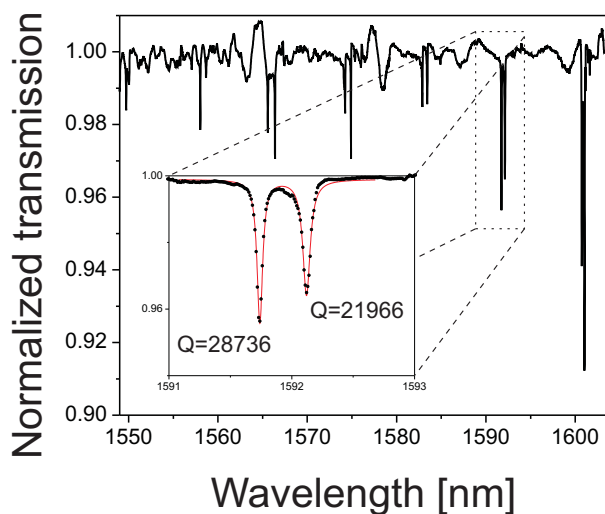


Figure 2.21: Transmission measurement in 50- $\mu\text{m}$  diameter, 135nm thick,  $\text{Si}_3\text{N}_4$  microdisk resonator. The light has been coupled within the cavity via a tapered-fiber. In the inset a Lorentzian fit of a couple of peaks is shown. The resulting Q's is of about 20000 for both resonances.

mode amplitudes in upper,  $\psi_1$  and lower disk,  $\psi_2$  as [58]:

$$\begin{cases} i\hbar\dot{\psi}_1 = \hbar\omega_1\psi_1 - i\frac{\Delta\omega_1}{2}\psi_1 - J\psi_2 + F_1, \\ i\hbar\dot{\psi}_2 = \hbar\omega_2\psi_2 - i\frac{\Delta\omega_2}{2}\psi_2 - J\psi_1 + F_2, \end{cases} \quad (2.20)$$

where  $\Delta\omega_i$  is the cavity loss rate (linewidth) and  $F_1$ ,  $F_2$  are generic excitation terms (pump).  $J$  is the coupling coefficient and is equal to the energy-splitting between the symmetric ( $\psi_s$ ) and the antisymmetric resonant modes ( $\psi_a$ ), defined as:

$$\begin{cases} \psi_s = \frac{1}{\sqrt{2}}(\psi_1 + \psi_2), \\ \psi_a = \frac{1}{\sqrt{2}}(\psi_1 - \psi_2). \end{cases} \quad (2.21)$$

Indeed, the vertical configuration enhances the coupling between the WGMs which are phase matched along the resonator circumference. The modes have then the possibility to interact with each other along an optical path which is extremely larger than in the Q-independent, point-sized side coupling which is realized in many resonator systems [87, 88].

Since most of interesting phenomena appear when a clear distinction between symmetric and antisymmetric modes is realized, an *a priori* knowledge of the coefficient  $J$  is needed. If the separation between the resonators is large enough, starting with the field amplitude of a single, unperturbed disk, the symmetric and antisymmetric states can be constructed with eq. (2.21), considering different disk to disk distances and a possible radii mismatches, which is likely to occur in lithographic-related processing. This way of proceeding is called perturbative approximation (PA). The

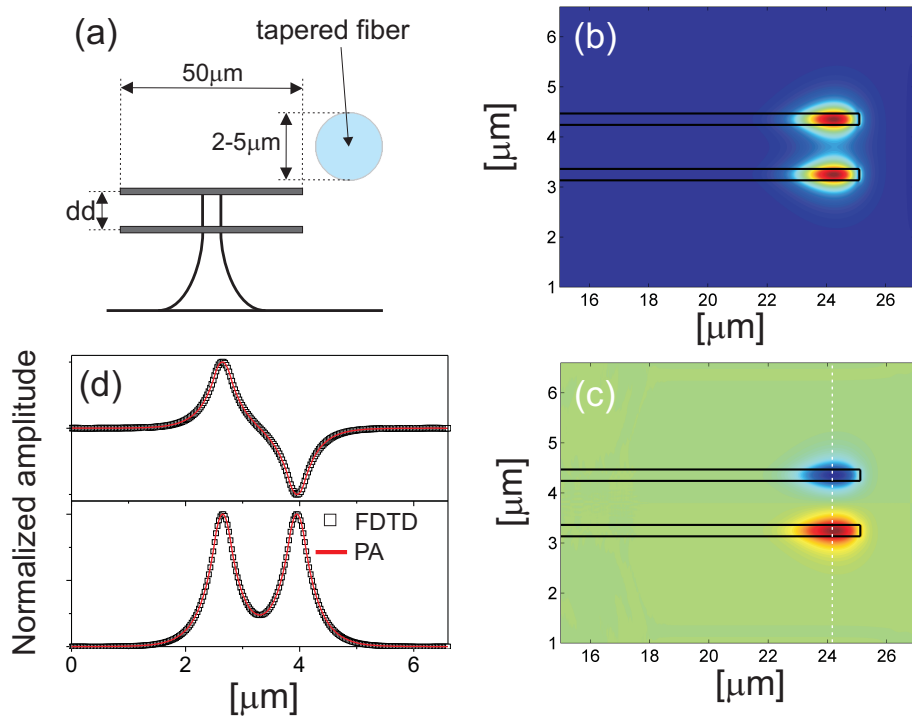


Figure 2.22: (a): Schematic of the measurement of vertically coupled microdisks. (b): Symmetric mode  $\psi_s$  obtained with FDTD algorithm (TE-like polarization). (c): The same for anti-symmetric mode  $\psi_a$ . (d): Comparison between slices of FDTD-obtained fields along the dashed line in panel (c) and the fields constructed in perturbative approximation (PA).

single disk considered is a  $50 \mu\text{m}$  diameter,  $300 \text{ nm}$  thick  $\text{Si}_3\text{N}_4$  disk. For comparison, the FDTD-obtained fields for symmetric and antisymmetric modes are reported in fig. 2.22 (b) and (c), for two identical disks (no-radii mismatch) placed at a distance of  $1 \mu\text{m}$ . The field amplitudes along the dashed line reported in panel (c) are then compared with the modes which have been constructed with the perturbative approximation. As can be verified in fig. 2.22 (d), the mode amplitudes are very well reproduced. The same agreement has been found up to distance as low as  $300 \text{ nm}$ ; after that, the PA does not hold any more and is not possible to consider a perturbative coupling interaction. Once  $\psi_s$  and  $\psi_a$  have been constructed, the coupling coefficient  $J$  has been evaluated as the energy difference of symmetric and antisymmetric resonances  $\hbar(\omega_a - \omega_s)$ . This have been calculated by inverting the spatial Helmholtz equation for the abovementioned states:

$$\begin{cases} \nabla^2 \psi_s = - \left( \frac{\omega_s}{c} \right)^2 \psi_s, \\ \nabla^2 \psi_a = - \left( \frac{\omega_a}{c} \right)^2 \psi_a. \end{cases} \quad (2.22)$$

Considering again the PA, while the single disk state  $\psi_1$  is known from FDTD simulations,  $\psi_2$  is obtained with rigid traslations of  $\psi_1$  at the desired spatial position.

It is then possible to determine  $J$  in the geometrical radii-mismatch<sup>4</sup>, disk-to-disk distance parameter space. Fig. 2.23 (a) reports the evaluated results. In panel (b) of the same figure the values of  $J$  for the case of no radii-mismatch has been reported. As expected, due to tunneling-like interactions,  $J$  is an exponential de-

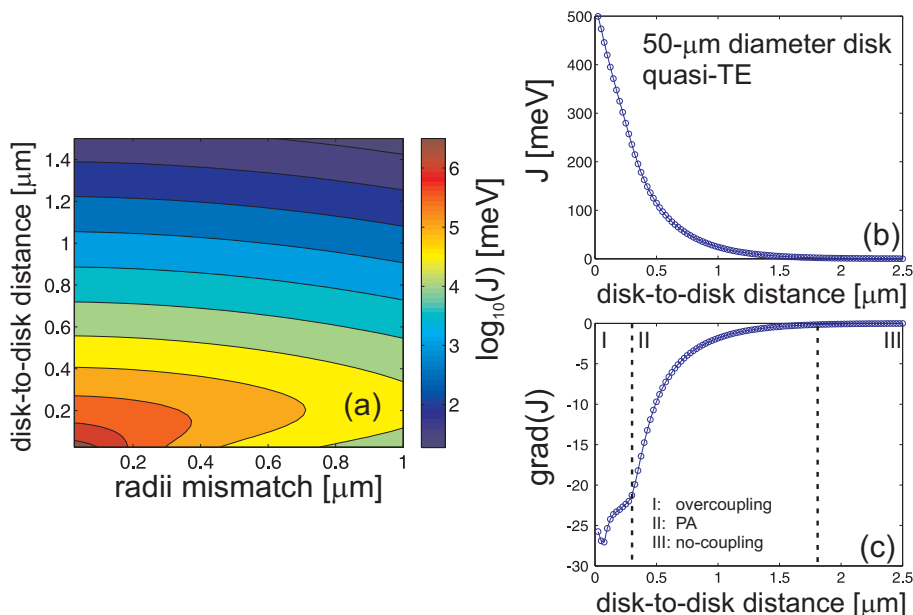


Figure 2.23: (a): Coupling coefficient  $J$  (in log scale) in the disk-to-disk distance, radii mismatch parameter space. (b): The extracted result in case of no-mismatch. (c): Gradient of  $J$  in panel (b). From the different slopes, different coupling regions can be investigated.

creasing function. When the derivative of  $J$  is investigated, three different regions can be observed, as reported in fig. 2.23 (c). In the first region, the PA does not hold any more, and the mode fields should be extracted employing full FDTD calculation of the whole, double disk structure. For disk-to-disk distances ( $dd$ ) larger than 300 nm, the PA formalism is valid and reproduce well the full wavefunctions. In this region the coupling is an exponential decreasing function with the distance, as expected. Finally, for  $dd$  larger than 1.8  $\mu\text{m}$ , the disk are practically uncoupled, and the resonances became that of the single disk,  $\omega_{a,b} \rightarrow \omega_1$ .

This particular geometry, which has been investigated so far, is a good candidate to observe interesting physical effects, such as optical dipole forces, coupled-resonator-induced-transparency (CRIT) [89] or optical potentials [56]. In particular, the possibility to observe Josephson-like oscillations in Optical Parametric Oscillation (OPO) regime will be discussed as a future perspective.

<sup>4</sup>Indeed, for the radii mismatch the PA could result a more crude approximation, since the field intensity in each disk will be different for the symmetric and anti-symmetric modes. Indeed the regularity of the map of fig.2.23 (a), suggests that, at first order, PA holds even in this case.

## 2.3 Conclusions and future perspectives

In this chapter the physics of active and passive of Si-based WGM microresonators has been discussed. This kind of devices are interesting both for practical applications, such as light emitting or biological sensing, that as platforms to evaluate and study constituting material optical properties. Indeed, since the cavity-modified photon DOS interacts with the emitters embedded within the resonators, some effects characteristic of the weak-coupling regime (like Purcell effect) can be probed and used to get informations on material optical properties. In this case, this has been used to evaluate the unknown Si-np linewidth in a bad emitter regime.

For applications, strain engineering effects can be exploited to realize Q-band tuning, which can be important to overcome mode competition in active devices. The  $\mu$ -kylix resonators I have presented represent an effort in this direction.

Finally, I have reported some feasibility discussions to investigate new physical phenomena in vertically coupled resonators. This geometry maximizes the mode coupling, which has been investigated in the perturbative approximation. One of the most interesting experiments regarding vertically coupled disks is the observation of non-equilibrium Josephson-like oscillation, which can be realized through Kerr nonlinearities of the microdisk constituent material. In the following, the perspective to observe this physical phenomenon is discussed.

### Optical Parametric Oscillation in SRSO coupled resonators

The refractive index which has been described so far is valid in the linear approximation of the material susceptibility. In principle, additional, higher order field-dependent terms should be included in its exact expression [90]:

$$n = n_0 + n_1|E| + n_2|E|^2. \quad (2.23)$$

The physical origin of these nonlinear contributions is due to the local modification of the microscopic polarizability of the material. In particular, second order terms are called Pockels nonlinearities, while the third order are called Kerr nonlinearities. If coupled identical resonators are constituted by a material in which Pockels effect is absent but Kerr one is present (as happens, for example, in centrosymmetric materials), eq. (2.20) reads as:

$$\begin{cases} i\hbar\dot{\psi}_1 = \hbar\omega_1\psi_1 - i\frac{\Delta\omega_1}{2}\psi_1 - J\psi_2 + g_k|\psi_1|^2\psi_1 + F_1, \\ i\hbar\dot{\psi}_2 = \hbar\omega_2\psi_2 - i\frac{\Delta\omega_2}{2}\psi_2 - J\psi_1 + g_k|\psi_2|^2\psi_2 + F_2, \end{cases} \quad (2.24)$$

where  $g_k$  is a third order nonlinear coefficient. Neglecting the loss and pump contributions, it is worth to note that, when the nonlinearity is turned on,  $\psi_a$  and  $\psi_s$  are no longer eigenstates of the system. Generally, the new eigenstate are labelled  $\psi_+$  and  $\psi_-$ .

Some of the solutions of eq. (2.24) are quite similar to the dynamics which describes the Josephson effect in two superconducting materials separated by a thin insulator (Josephson junction). If a constant voltage is applied in such system, an

alternate current with oscillation frequency equals to the energy difference between the Cooper pair in the two superconductors can be observed [57]. In analogy with this phenomenon, in a coupled resonator system, for particular values of  $g_k$ , it is possible to find spectral region of parametric instability, in which the field amplitude of WGM mode within a disk oscillates with a  $J/\hbar$  frequency<sup>5</sup> [58].

Noteworthy, even if the dynamics is similar, the optical Josephson-like oscillations are generated by very different physical mechanism than the superconducting current one. The most striking difference is that while Josephson current oscillations are realized in an equilibrium regime, the optical ones are the result of strongly out of equilibrium nonlinear instabilities (parametric instabilities). More in detail, the physics behind this behavior originates from Optical Parametric Generation (OPG) nonlinear effect. In this process, a pump photon interacts with the vacuum field generating a signal and idler photons of different frequency [50]. The frequency of these is fixed by the energy conservation and phase-matching conditions [50]. In particular, in vertically-coupled WGM cavities, the interacting modes are phase matched point-by-point along the disk circumference, maximizing the nonlinear effect.

Starting from this point, it is possible to understand the onset of the oscillating regime. Consider a pump source  $F_i$  in one of the two resonator which is spectrally detuned from the cavity resonances. Increasing the pump intensity, the cavity eigenstates are blue shifted (if  $g_k > 0$ , red shifted in the opposite case), and eventually becomes resonant with the signal or idler photons. If the OPG effect overcomes the loss rate of the system, the resonant eigenstate goes towards a lasing regime, with a line-narrowing effect. In nonlinear optics this situation is known as Optical Parametric Oscillation (OPO). Since the eigenstates are linked together by the coupling coefficient  $J$ , a OPO regime is reached even for the eigenstate which is non-resonant with the signal/idler photons. The condition of the so-called parametric instability makes the field amplitude oscillates between the eigenstates of the system at a frequency value of  $J/\hbar$ , as briefly discussed above. The characteristic signature of this phenomenon can be inspected in the field spectrum by the appearance of extremely narrow symmetrical resonant peaks, spectrally detuned from the pump frequency by the same value  $J/\hbar$ . While the system of eq. (2.24) has been solved in the literature [58] and can applied to various physical systems, in this context it is useful to determine the feasibility to observe this phenomenon in vertically coupled WGM resonators. FDTD simulations have then been performed considering Si-np nonlinear material, whose nonlinear refractive index has been taken from the literature [61]. To reduce the computational effort, small, 10- $\mu\text{m}$  diameter disk have been considered. Figure 2.24 (a) reports the expected Josephson-like oscillations in the top disk, in which is physically placed the non-resonant, CW pump source. Figure 2.24 (b) reports the comparison between eq. (2.24) analytical solution and FDTD calculation in the same pumping condition. A good agreement can be observed, even in higher order replicas, as the one which appears at about 4.5 meV. This result assures the possibility to observe this physical effect in the proposed coupled-WGM geometry. The analytical solution is obtained in an approximated linearized regime;

---

<sup>5</sup>This is verified in systems where the cavity linewidth  $\Delta\omega_c$  is narrower than the coupling  $J$ . In strongly coupled systems, even if the physics is the same, the oscillations frequency can be slightly different from  $J/\hbar$ .

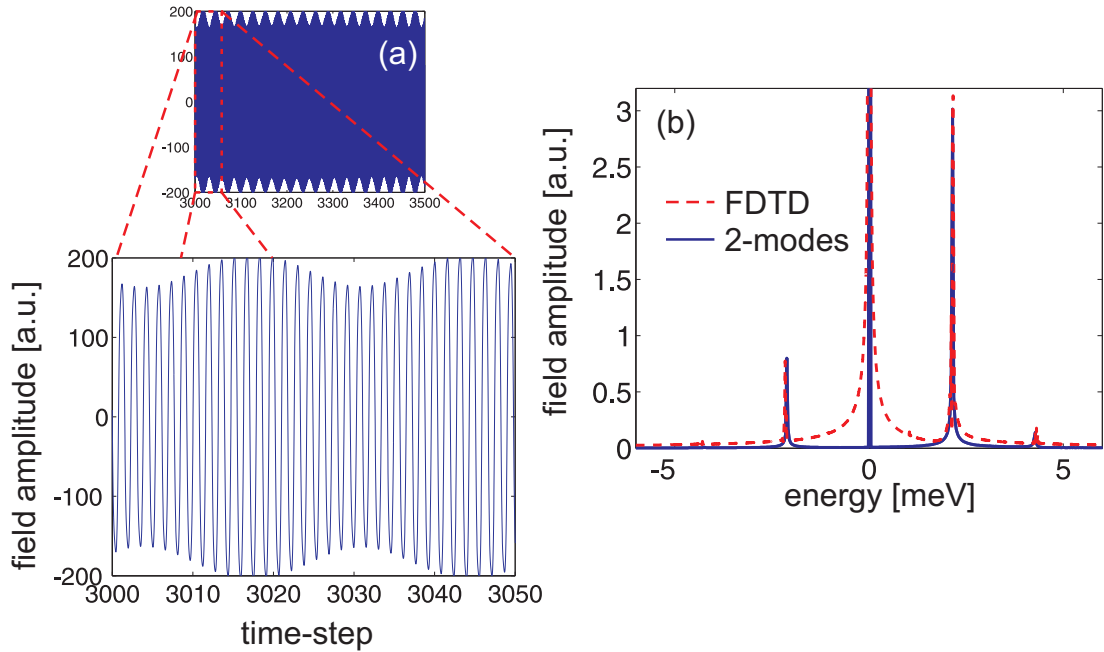


Figure 2.24: (a): Electric field amplitude in the top disk. In the zoomed frame it is possible to appreciate both the field oscillations at pump frequency and a slower Josephson-like oscillation. (b): Comparison between analytical and FDTD spectra for the coupled-disk system. Apart from the pump peak, which is slightly broadened in FDTD, the resonant peak positions and intensities are in very good agreement. Analytical curve courtesy of Davide Sarchi.

in this sense FDTD results, which are not subjected to this kind of approximation, confirm the validity of the 2-modes approximation, since all the spectral features are well reproduced in both methods.[58].

This kind of devices, if produced, are appealing for different reasons. From a fundamental point of view, an all-optical Josephson oscillations regime could be observed, since no experimental results in this kind of system have yet been reported. From an application side, the development of Si-based OPO sounds interesting in a further advance towards an efficient light emitter made of this material. In fact, the intrinsic nature of the physical effect under investigation allows one to realize a spectral tuning of the OPO emission, since the pump source must be nonresonant with the cavity modes frequencies. For the same reason, extremely high  $Q$  values are not necessary to observe the effects, whereas up to now optical nonlinear effects have been exploited only in ultra-high  $Q$  WGM cavities [83, 84, 91].

## Chapter 3

# Light-matter interaction enhancements in slow-light waveguides

When the control of light propagation at the nanoscale is achieved, electromagnetic radiation can be used to enhance material optical properties, such as photon emission/absorption or nonlinear effects. One of the possible way to do this is to increase the interaction time between light and matter. While a naive solution to this end requires an increase in the optical path traveled by light, a more clever possibility acts directly to slow down the group velocity of the radiation [88].

The physics of so called slow light has been investigated for some years in several systems. The slowing down process is achieved mainly through material dispersion related schemes, where physical phenomena such as Electromagnetic Induced Transparency (EIT) [92], Coherent Population Oscillation (CPO) [93] or Four-Wave Mixing (FWM) [50] are used to induce rapid change in the material refractive index. Alternatively, waveguide dispersion induced by complex dielectric structures can be exploited to slow down the light [94, 95]. Recently, delays as large as 500 ps have been obtained in Coupled-Resonator Optical Waveguides (CROW) devices with a footprint smaller than  $0.09 \text{ mm}^2$  [97]. This large delay can be used to obtain all-optical buffers in which lights can be stored and then subsequently retrieved. But even systems where a moderate slowing down of light is achieved reveal very useful properties when light-matter interaction related phenomena are considered. The almost flat photonic band dispersion increases the nonlinear efficiency [98] or, from another point of view, displays a large photon Density of States (DOS), with a correlated large spontaneous emission enhancement effect (Purcell factor).

Waveguide dispersion is often controlled by means of periodic patterning of the dielectric structure. In these periodic dielectrics, called photonic crystals [72, 99], the periodicity is of the same order of optical wavelength. Thus, photonic bands are created, similarly to electrons in crystalline lattice hosts. In this scheme, the group velocity is defined as the first derivative of the band energy in the reciprocal space. All the informations regarding light propagation is then included in the reciprocal space of the fundamental, irreducible real-space cell (First Brillouin zone). It is important to point out that the photonic DOS is inversely proportional to the

group velocity modulus. . As briefly shown in the explanatory photonic bands of fig. 2.15, in total analogy with the electronic counterpart, regions where no photon can propagate (band-gaps) are formed, with a corresponding photon DOS equals to zero. Conversely, at the band edge and around defect states, the group velocity is strongly reduced and the DOS can reach values extremely larger than its bulk counterpart.

In this chapter I will present theoretical simulations and experimental characterization of photonic crystal waveguides in which the speed of light can be severely reduced in order to tailor different effects. At first, the possibility to localize light in nonlinear, low index materials is investigated through the use of high index contrast slot waveguides. Successively, a scheme based on photonic crystal patterning of the waveguides for the enhancement of nonlinearity is proposed. In this sense, I will show that even a moderate slowing down of the light is enough to increase the effective nonlinear coefficient of some orders of magnitude. Additionally, preliminary experimental results are presented in which the desired spectral features can be observed in transmission experiments.

Due to the possibility of precisely control the electromagnetic field at the nanoscale, in a different waveguide structure, the theoretical Purcell enhancement for an ensemble of many emitters is analyzed. Even if slow-light waveguides for Purcell effect observation have been proposed in the literature [100, 101], their performances are strongly limited by spatial averaging terms, which have been described in eq. (2.13). These photonic structure are usually investigated in the limit of single emitter embedded within the waveguide. The realization of optical waveguides in which many emitters are placed in regions with large DOS is indeed intriguing both for an efficient excitation of photonic crystal optical modes and for the observation of peculiar physical effects, such as the theoretically predicted bandgap superradiance [102].

### 3.1 Slow light in silicon coupled cavities waveguides

In this section design, simulations and preliminary optical characterization of CROWs are reported in order to achieve a slow light effect [88]. As mentioned in the previous section, slow light greatly enhances the nonlinear optical properties of the material. This can be easily understood considering, for example, the band structures reported in fig. 3.1 for a homogeneous material and for a typical CROW device. It is possible to model the effect of nonlinear refractive index modification,  $\delta n$ , as a rigid energy translation of band structure of a quantity  $\delta\omega$  [98] as:

$$\frac{\delta\omega(k)}{\omega} = \sigma \frac{\delta n}{n}, \quad (3.1)$$

where  $\sigma$  is a coefficient which considers the energy fraction involved in the nonlinear process. As can be inspected in fig. 3.1, when a flat dispersion is considered, the induced  $\vec{k}$ -vector shift is larger than the one correlated with bulk material linear dispersion. In several applications, like optical switching, nonlinear processes are

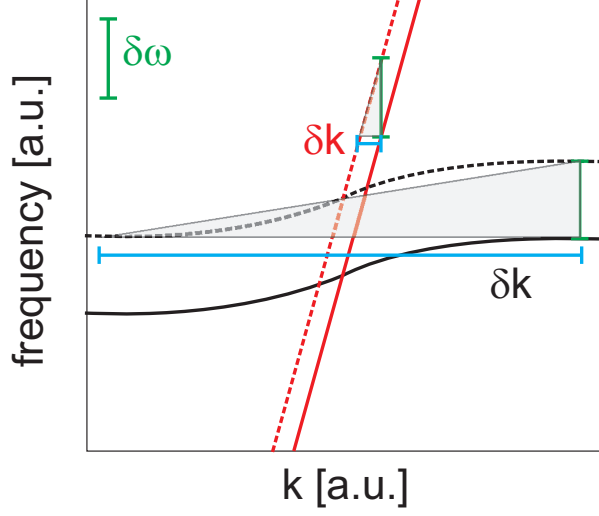


Figure 3.1: Schematic comparison of  $\delta k$  modification induced by the same frequency shift  $\delta\omega$  for a defect mode (flat-like dispersion, more on this later) and for a bulk material (linear dispersion).

used to induce a light phase shift  $\delta\phi$ , which depends on the  $\vec{k}$ -vector as:

$$\delta\phi = \delta k \cdot L, \quad (3.2)$$

where  $L$  is the length of the device. Clearly, the  $\vec{k}$ -vector shift is directly proportional to the phase shift. Using eq. (3.1), it is possible to relate the latter with the nonlinear refractive index change,

$$\delta\phi = \frac{2\pi\sigma L}{\lambda} \left( \frac{\delta n}{n} \right) \left( \frac{c}{v_g} \right). \quad (3.3)$$

While the refractive index modification  $\delta n$  depends on the chosen material, it is interesting to note an additional factor  $c/v_g$  which stems directly from the waveguide dispersion. It is straightforward to see that large phase shifts can be achieved when the group velocity  $v_g$  is reduced with respect to the speed of light in vacuum  $c$ . Alternatively, it is possible to get the same phase shift, considering an ideal device where  $v_g = c$ , with a length reduction of the same factor  $c/v_g$ . Since nonlinear effects are activated injecting energy in the system, it is possible to obtain the same power density of the ideal device with an additional excitation power reduction of  $c/v_g$ . Concluding, when an ideal device is compared with a slow light device of the same length and at the same pumping power, an overall enhancement of  $(c/v_g)^2$  for nonlinear effects is obtained. Even moderate values of  $v_g$ , like one-tenth of speed of light in vacuum ( $0.1 c$ ), realize a two-orders of magnitude enhancement of investigated nonlinear effects.

As briefly mentioned in 2.3, Si-np have revealed good nonlinear properties, with a nonlinear refractive index coefficient  $n_2$  of the same order of GaAs and at least one order of magnitude larger than bulk Si one [61]. Since Silicon-Rich-Silicon-Oxide (SRSO) is CMOS-compatible, it would be interesting to employ it as active material for nonlinear-optical waveguide devices. Due to its low refractive index (1.7-1.8 at

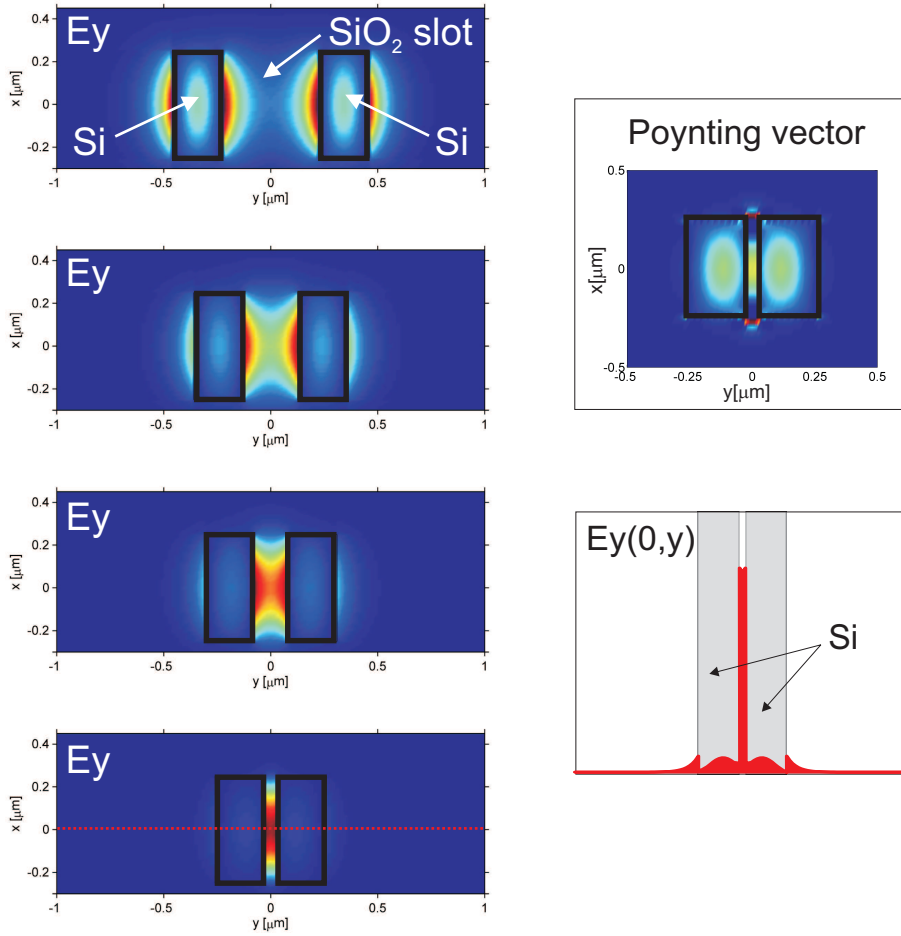


Figure 3.2: Slot effect for different wires distances. While in the top panel the electric field is concentrated in the Si wires, in the bottom one the maximum is inside the slot region. In the inset the Poynting vector for the bottom panel geometry is reported.

$\lambda = 1.5 \mu\text{m}$ ) SRSO waveguides directly lithographed on  $\text{SiO}_2$  substrate ( $n_{\text{SiO}_2} = 1.45$ ) occupy a large footprint due to poor light-confinement. A solution for this problem employs large index contrast waveguides where the electric field can be localized in low index materials, using a geometry called slot waveguide [103]. The slot geometry is composed by two high index material wires (wall region) which sandwich a thin layer of a low refractive index material (slot region). As shown in fig. 3.2 for Si walls and air slot, when the distance between the wires is reduced, the electric field component which is perpendicular to the wall-slot interface is increased, due to the sum-up of the evanescent fields in the slot region. This effect, due to field discontinuities, can be observed only for the TE polarization in vertical slot waveguide as the one in fig. 3.2. The peculiar field profile of the slot optical mode is reported in the inset, where a cut in the middle of the structure (dashed red line) has been realized. With the same physical considerations it is possible to produce horizontal slot waveguides which works for TM polarization. It is worth to mention that in the same geometry the Poynting vector experiences only a partial enhancement (see fig. 3.2, inset). In fact, only the electric field is subjected to the discontinuity necessary for the achievement of slot effect while the magnetic field is still confined within the

high index dielectric.

Several approaches can be considered to increase the nonlinear effects in this structure. The easiest one is to realize a resonant cavity in which the light can circulate for a certain time, thus increasing the effective interaction length between field and material. This is directly proportional to cavity Q, as seen in chapt. 2, and a large increase in the interaction length requires large-Q cavities. While these can be achieved with some technological efforts, the sharp resonant lineshape does not allow the propagation of laser pulses without distortion effects. A smarter approach requires the use of coupled photonic crystal defect modes.

A photonic crystal is a periodic complex dielectric structure with discrete trans-

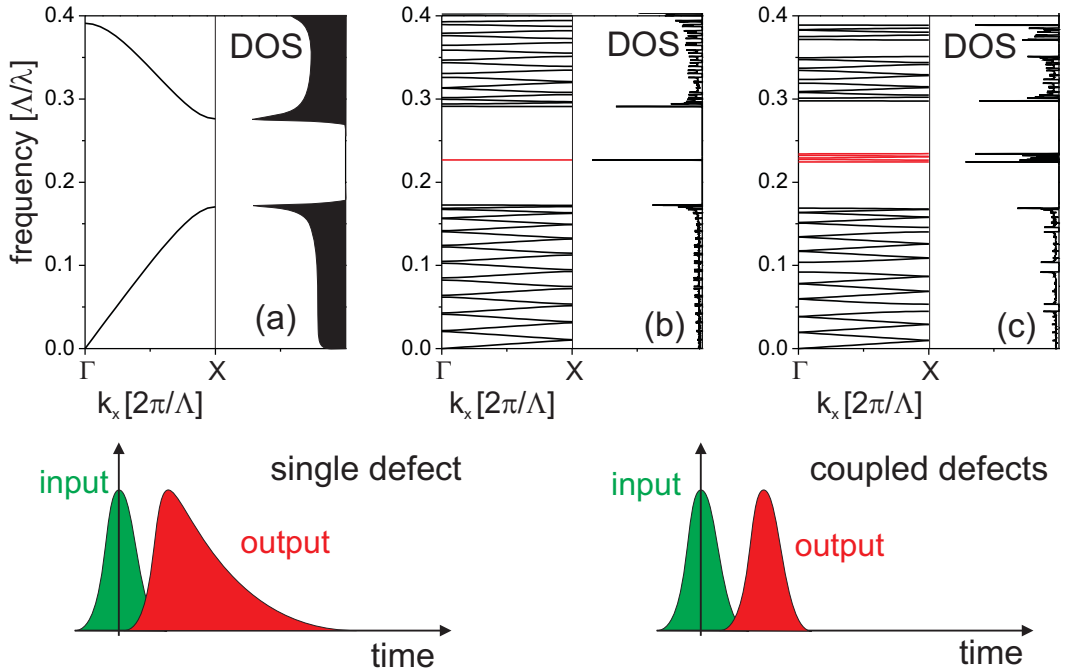


Figure 3.3: Energy bands and DOS for different 1D Si-air multilayer structures. (a): Simple mirror. (b): Single defect. (c): Five coupled defects separated by 8 periods. Bottom panel: Schematic of distorted and undistorted pulse traveling in structure of panel (b) and (c) respectively.

lational symmetry. In total analogy with electrons in a crystalline host, the photon modes form energy bands in the reciprocal space. From this restricted region, light propagation on the whole structure can be inferred. The Bloch theorem is valid even in the photonic case and the electromagnetic eigenfunctions can be written for continuous translational symmetry as:

$$\Psi_{n\vec{k}}(\vec{r}) = e^{i\vec{k}\cdot\vec{r}} u_{n\vec{k}}(\vec{r}), \quad (3.4)$$

where  $u_{n\vec{k}}$  is the electromagnetic field in the fundamental cell, which is the representation of the irreducible group of the structure symmetry [104]. The functions  $\Psi_{n\vec{k}}(\vec{r})$  (Bloch modes) are then standing waves with the same periodicity of the photonic crystal.

The photonic band structure can be calculated with different methods. In the work here described an open-source package based on the plane-wave expansion method has been employed [105]. As example, fig. 3.3 (a) reports the first two bands on an infinite Si-air multilayer with period  $\Lambda$  along the  $\hat{x}$  direction (Bragg mirror). Each period is composed by a single Si and air layer each of thickness equal to  $\Lambda/2$ . Along the vector  $k_x$ , which is the reciprocal of the vector  $x$ , a band structure can be observed. The points  $\Gamma$  and  $X$  represent high symmetry points in the first Brillouin zone [104]<sup>1</sup>. The DOS relative to the band structure is sketched in the same panel. It is evident that no photon can propagate in band gap spectral region, due to the zero DOS. On the other hand, it is possible to observe a DOS increase in the band edge regions.

When a single defect is inserted in the structure, for example replacing a single air layer with a Si one, the structure is no more *strictly* periodic and the so-called defect modes appear within the gap. Even if the fundamental cell is now the whole dielectric structure (in this case infinite), when a single defect is present, the photonic bands can be reproduced using a finite super-cell, which is composed by a defect surrounded by many fundamental cell periods in order to de-couple possible interactions between adjacent defects modes. If this new cell is considered as the periodic unit, it is possible to find a degenerate defect mode which approximates the ideal, infinite case.

In fig. 3.3 (b), the flat-dispersion curve of the defect mode is reported in red and falls energetically in the middle of the gap. Due to the lack of available DOS within the band gap, the defect mode is well isolated from the external environment, which is manifested by the sharp,  $\delta$ -like DOS curve. The partial folding of the photonic bands is due to the finite size of the super-cell used in the simulation. If the separation between adjacent defects is not large enough, the defect mode is splitted due to tunneling-like interactions, with the same physical mechanism discussed in sec. 2.2. In fig 3.3 (c) five interacting (coupled) defects in a super-cell are reported. If the interaction is properly tuned, the defect modes can form a mini-band, with a flat, constant DOS and consequently with a constant group velocity. If this is properly done, a pulse spectrally contained within the flat miniband, injected as waveguide input, can be retrieved undistorted at the output. On the other hand, a single uncoupled defect would form a sharp transmission band, resulting in distortion of the pulse, due to the strong differences of group velocities of harmonic components tuned and detuned from the resonance. This is briefly shown in the schematic of fig. 3.3, bottom panel.

## CROW design and simulation

Different geometries can be considered in order to realize a photonic crystal within an underlying slot waveguide structure. In fact, vertical slot waveguides offer different possibilities, like internal/external comb indentation [106]. Unfortunately, the high resolution, deep-UV lithography needed to realize the nanometric geometrical features, makes the sample processing extremely difficult, with a collateral increase in waveguide propagation losses. The use of horizontal slot waveguides offer a sim-

---

<sup>1</sup>In particular, the point  $\Gamma$  and  $X$  have respectively coordinate  $[0, 0, 0]2\pi/\Lambda$  and  $[0.5, 0, 0]2\pi/\Lambda$

pler choice, yet limiting the photonic crystals geometry which can be employed. In particular, the etching of full trenches is proposed to create a Bragg mirror with gap centered at  $1.55 \mu m$ . The mirror geometry is depicted in fig. 3.4, where additionally the underlying slot waveguide geometry is described.

While the final design and simulations have been realized for the full, 3D wave-

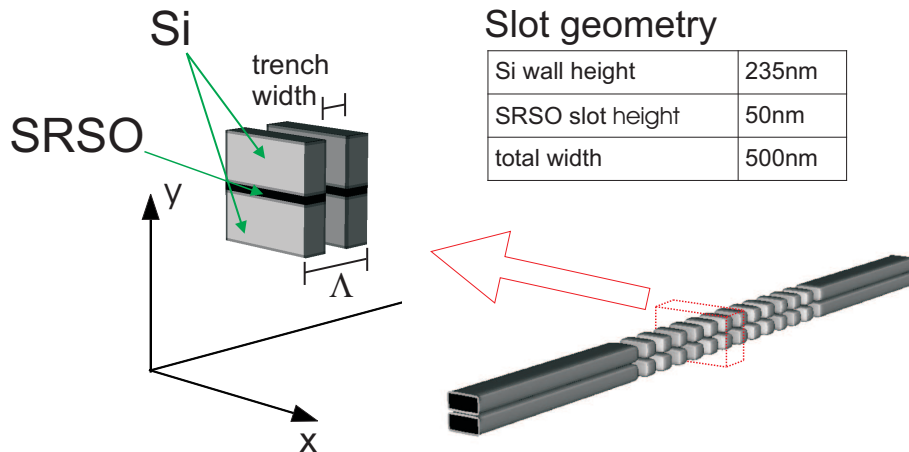


Figure 3.4: 3D scheme of the photonic crystal waveguide proposed. The fundamental cell composed by Si walls ( $n_{Si} = 3.45$ ) and SRSO slot ( $n_{Si} = 1.6$ ) is zoomed. The geometrical parameters of the slot waveguide are added for completeness.

guides, some features like finite-size effects and adiabatic tapering have been fully analyzed employing 2D simulations (infinite width waveguides) in an effective index approximation scheme [36].

Figure 3.5 (a) reports the quasi-TM photonic bands for the infinite photonic crystals whose fundamental cell is reported in fig. 3.4. In this case the trench width was of 150 nm while  $\Lambda = 407$  nm was the lattice periodicity<sup>2</sup>. In a photonic crystal, the difference between guided Bloch modes and radiative modes is depicted employing the line-of-light dispersion. This is defined considering the external environment index ( $n_{env}$ ) as  $\omega = c/n_{env} \cdot k$ ; a band state which falls energetically above this line is a radiative mode, while conversely, the Bloch guided modes are concentrated below the line [104]. When the line-of-light (dashed red line) is added in the bands of fig. 3.5 (a), a pseudo-gap between Bloch mode opens, whereas the states lying above the line-of-light are not bounded to the dielectric.

The fundamental cell bands can be compared with the bands of a typical CROW device, reported in fig. 3.5 (b). Here the defect is represented by an unperturbed waveguide length of 480 nm which is replicated each 8 fundamental cell periods ( $8\Lambda$  mirror). With such a separation between adjacent interacting cavities, a mini-band defect mode is then formed. This is magnificated in fig. 3.5 (c).

From the band curve derivative, the group velocity can be obtained. For the defect mode, the absolute value of  $v_g$  is reported in the same panel, as a dashed line. Note that it can reach very low values, up to  $5 \times 10^{-5}c$  in the ideal, 2D case here discussed.

<sup>2</sup>These parameter have been obtained to maximize the pseudo-gap width and center it in the NIR region, around  $1.55 \mu m$  [107].

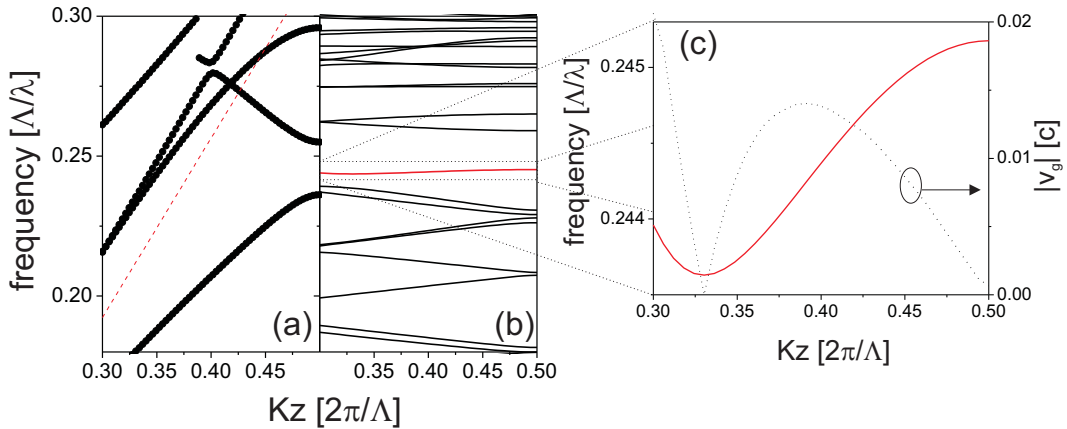


Figure 3.5: (a): Photonic bands in a 2D effective index approximation for the fundamental cell depicted in fig. 3.4. (b): Photonic bands for an infinite CROW where a 8 period (8  $\Lambda$ ) mirror has been posed between neighboring cavities. (c): Zoomed defect mode mini-band and group velocity modulus.

Since in real devices finite-size effects and possible adiabatic tapering have to be taken into account, photonic-bands related simulations do not represent the best approach to design the final structure. The next design steps are therefore based on FDTD simulations of different waveguides. A particular interesting parameter, in this case, is represented by the transmission value of light pulse through the waveguide. To appreciate the connection between photonic bands and transmission, in fig. 3.6 (a) a 3D simulation of the bands of the infinite defectless photonic crystal is reported. This can be easily correlated with the 3D transmission FDTD simulation of a  $16\Lambda$  mirror with the same geometrical structure. The photonic gap feature appears as a minimum in the transmission curve, since the propagating modes are stopped by the zero DOS in this spectral region.

Fig. 3.6 (c) reports the transmission curves for different structures, of which a

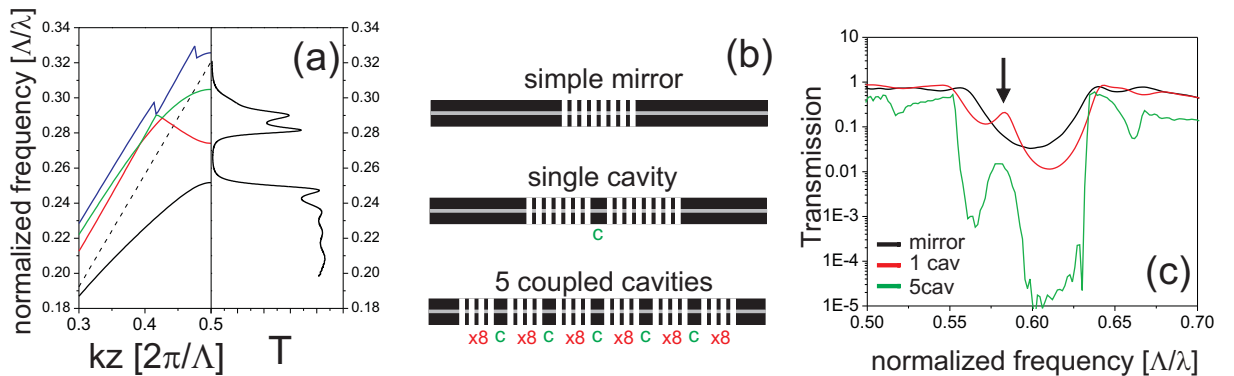


Figure 3.6: (a): Photonic bands for the full 3D photonic crystal waveguide and FDTD transmission curve for a  $16\Lambda$  mirror. (b): Waveguides composed by a different number of defects. Their FDTD-simulated transmission curves are reported in (c).

geometrical scheme is reported in fig. 3.6 (b). Again the 2D effective index approximations has been used. It can be seen that when the number of interacting defects

is increased a flat-band is formed, which spans for some nanometers (indicated by an arrow in the figure). It is right to point out that the transmission peak value is far from the maximum achievable value of 1. This is due to two different kinds of losses: geometry-related losses, which can be reduced correcting for finite-size effects and employing an adiabatic tapering, and intrinsic radiative losses. The latter can be understood considering that the Bloch modes are usually coupled with a continuum of radiative modes and thus a portion of their energy is continuously radiated outside the dielectric. Since the Bloch mode (3.4) are standing waves which are harmonic in time, i.e.  $\propto e^{i\omega t}$ , the losses terms can be extracted considering the imaginary part of the complex frequencies  $\omega$ . If this is considered, the field amplitude is then proportional to an exponential decay time function. It is possible to transform the time-rate loss in a distance-rate loss using the group velocity, getting a final value for the loss coefficient  $\alpha$  of:

$$\alpha = \frac{\Im(\omega)}{v_g}, \quad (3.5)$$

where  $\Im(\omega)$  represents the imaginary frequency. More formally this can be derived by time-dependent perturbation theory [108]. It is important to point out that in a slow-wave device, though the nonlinear effects are enhanced, a contemporary linear losses enhancement is unavoidable [109]. This is one additional reason to work with moderate group velocity, whereas in case of extremely low group velocities extraordinary efforts both from technological and from design point of views should be performed to keep the losses in a realistic range for a working device. Despite the presence of this effect, manageable experimental insertion losses of 7 dB have been found in 27  $\mu\text{m}$  devices, as reported in fig. 3.10 (c).

When dealing with a real waveguide, finite size effects, which do not compare in the ideal, infinite structure, have to be considered. In particular, in an analogy with electrical circuitry physics, the photonic crystal structure impedance has to be matched with the external environment one. This can be done considering a reduced number of periods for the most external mirrors: for a  $M$  periods internal mirrors, one should consider  $M/2 + 1$  periods external ones [110, 111]. The effect is clearly visible in the transmission/reflection spectra of fig. 3.7 (a) for a two-coupled cavities air-Si wire photonic crystal. The periodic structure even in this case is made of fully-etched trenches. When no impedance matching is considered the structure is composed by three 8-periods mirrors ( $8\Lambda$ ) which sandwich two defects (C). The whole structure can be schematized as  $8\Lambda\text{-C-}8\Lambda\text{-C-}8\Lambda$ . Conversely, the impedance-matched (IM) structure possesses reduced external mirrors,  $5\Lambda\text{-C-}8\Lambda\text{-C-}5\Lambda$ . While in the original structure transmission spectra it is possible to clearly distinguish the resonant modes transmission (reflection) peaks (dips), when the IM is considered, not only the transmission value is increased, but an almost-flat pass-band is achieved.

Even if impedance-matched, some additional losses can be related to the abrupt change of the optical mode when injected in the photonic crystal. This passes from a travelling wave mode in the slot waveguide, to a standing-wave photonic crystal Bloch mode within the CROW. The same degrading mechanism acts at the interfaces between the periodic mirror and a defect. A smoother change can be realized

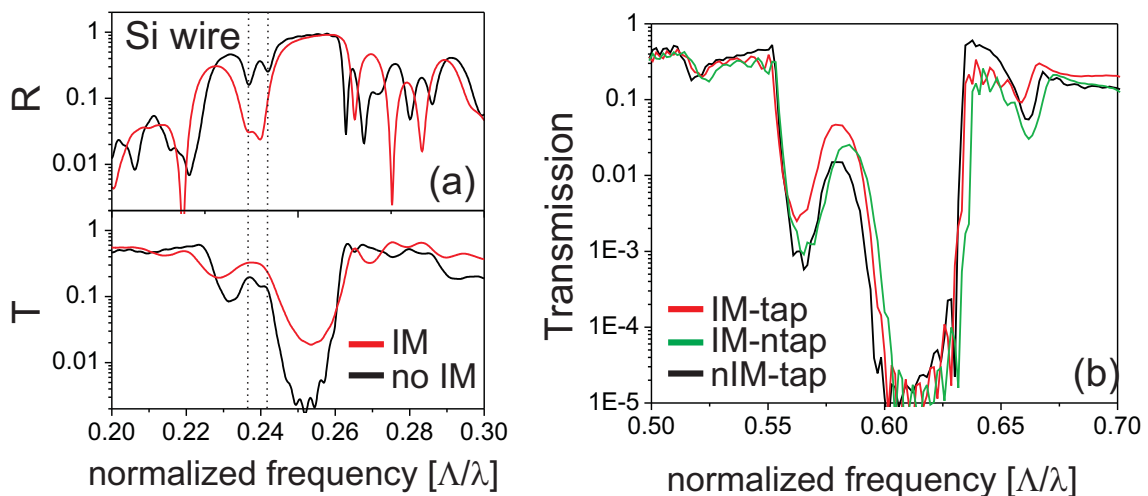


Figure 3.7: (a): Effect of impedance matching for a two coupled-cavities photonic crystal composed by air trench on an underlying Si wire. The IM effect both flattens and enhances the defect-related transmission peak. (b): Transmission curves in 2D effective index approximation for the  $8\Lambda$  mirror, 5 coupled cavities device reported in fig. 3.6. When both the IM and the adiabatic tapering (tap) of the first and last period of each mirror is considered, a six-fold enhancement of the transmission peak can be observed.

considering an adiabatic tapering in which the periodic structure is gradually modified to better match the surrounding environment [112]. The main problem with this kind of solution is that an analytical method to determine the tapering geometry does not exist. Even though numerical algorithms can be used, if the whole periodic structure is considered, the tapering can be designed employing multi-dimensional empirical optimization, or momentum-space design technique [113] which represent though computational problems. To overcome this limitation, a tapering of only the first and last period in each mirror has been considered. The optimized geometry for this period has been found narrowing the first trench length to 120nm. Figure 3.7 (b) reports the modified transmission when the impedance matching (IM) and the adiabatic tapering (tap) are considered. A six-fold increase in the transmission peak can be revealed. Eventually, this can be further enhanced considering the adiabatic tapering of a larger number of periods.

If the number of periods composing the mirrors is increased it is possible to enhance the quality factor and the group velocity reduction of the defects mode, at expense of the flat-band width. The time delay, bandwidth product in fact represents a standard figure-of-merit for the slow light devices. This can be verified in fig. 3.8 (a), which reports the transmission spectra for CROWs composed by 5 cavities ( $5c$ ) considering respectively mirror of 8 and 16 periods ( $8\Lambda$ ,  $16\Lambda$ ).

To evaluate the group velocity in this kind of device the time-of-flight technique has been employed. A quasi-monochromatic pulse is injected at the waveguide input and its analyzed employing a FDTD-sensor placed at the structure output. Figure 3.8 (b) reports the normalized field collected from the sensor in different environments. Due to the nature of FDTD algorithm, the time-envelope amplitude of the injected pulse is a gaussian function, which can be clearly recognized in the figure. The three

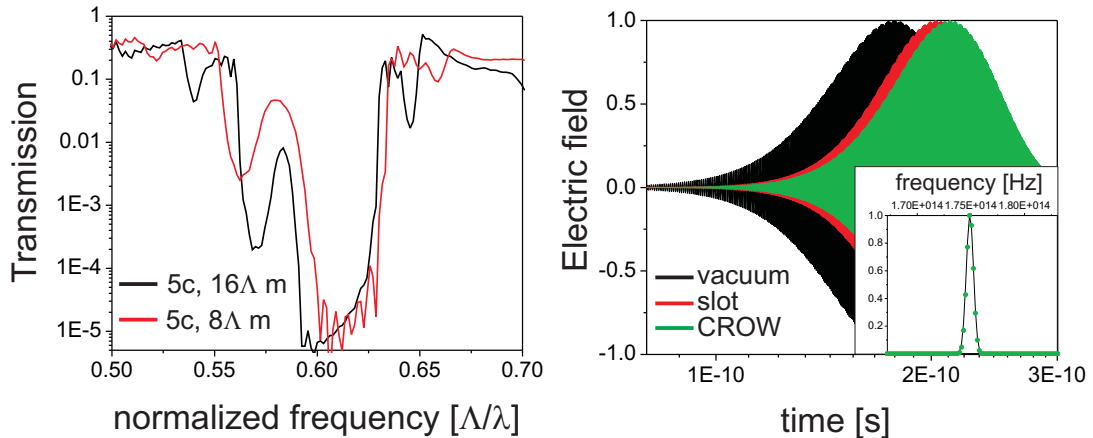


Figure 3.8: (a): Transmission spectra of 5-cavities CROWs with respectively 8 and 16 periods mirrors in 2D effective index approximation. (b): Normalized quasi-monochromatic pulse electric field propagation in different environment. The pulse central frequency is tuned in the middle of the transmission peaks of panel (a). The distance between the source, which is turned on at  $t=0$ , and the sensor which collects the field is  $32 \mu\text{m}$ . The comparison between the vacuum (black curve), a simple slot waveguide (red curve) and the 5c, 16 $\Lambda$  m of panel (a) (green curve) is reported. The delay between the first and last curve is of 34.71 ps, corresponding to a group velocity  $v_g$  of 0.003  $c$ . In the inset a comparison between the Fourier transform of the vacuum (solid line) and CROW (green dots) pulses is reported, where the undistorted pulse propagation can be appreciated.

curves show the effects of different group velocities when the same pulse is injected in vacuum (black curve), in a horizontal slot waveguide (red curve) or in the 5c, 16 $\Lambda$  CROW of fig. 3.8 (a) (green curve). The pulse central frequency has been chosen to fall in the middle of the transmission spectrum resonant peak. It is worth to note that the pulse is practically undistorted when propagates in the CROW: this can be checked in the inset of fig. 3.8 (b), where the comparison of Fourier transform of the vacuum and CROW pulses is reported. From the pulse-to-pulse delay and the known device length ( $32 \mu\text{m}$ ) a reduced group velocity of 0.003  $c$  can be extracted. In similar structures, as the 5c, 8 $\Lambda$  showed in panel (a), less reduction  $\sim 0.1 c$  is accompanied by a wider flat transmission band. Indeed, a slow down of  $v_g = 0.1 c$  can sound interesting, due to the fact that while on one side increases the losses of one order of magnitude, the nonlinear effects are enhanced by two orders of magnitude, namely scaling with  $(c/v_g)^2$ . It has to be taken into account that it is possible to develop straight slot waveguide with propagation losses as low as 3 dB/cm [114]: with such an underlying structure a loss enhancement should not represent an hindrance impossible to overcome.

Preliminary optical characterization of the device has been performed with CW transmission measurements. The setup used is the same described in sec. 1.3.2. The sample have been fabricated by CEA-Leti Institute in Grenoble (France). A scanning electron microscope (SEM) top-view image of one the fabricated devices is reported in fig. 3.9. In the same figure a table with the comparison between fabricated and nominal parameters is reported, while the underlying horizontal slot

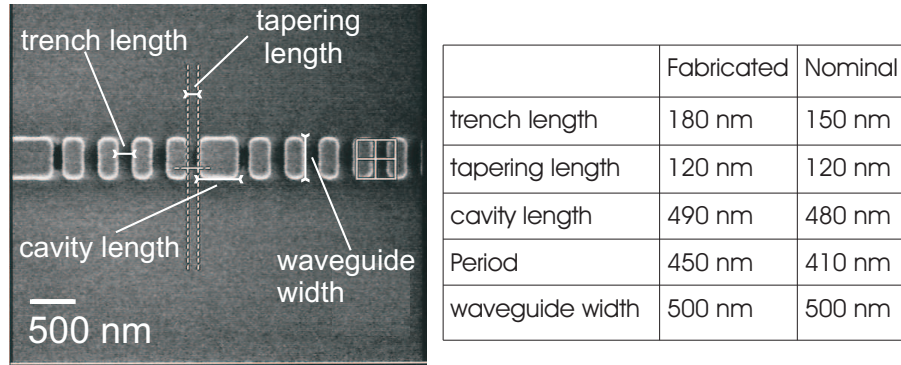


Figure 3.9: SEM top-view image of the photonic crystal waveguides under investigation. In the table a comparison between the fabricated and nominal geometrical parameters is reported. SEM image courtesy of CEA-Leti.

waveguide structure is described in fig. 3.4. Note the slight discrepancy among nominal and real values. Figure 3.10 reports the results for a  $5c$ ,  $8\Lambda$  CROW. In panel (a) and (b) a comparison between the simulated and experimental data is reported. Even though the structure was designed to have a defect at  $1550\text{nm}$ , some flaws during the processing stage made the real geometrical parameters slightly different from the nominal ones, as reported in fig. 3.9. This induces a  $50\text{ nm}$  blue shift of the whole spectral features. It is worth to note that even in simulated data the bands energies are rigidly red-shifted due to correction of the 2D effective index approximation. When the spectra are compared opportunely normalizing their central wavelength they are quite in agreement with each other. In panel (b) of fig. 3.10 a quantitative

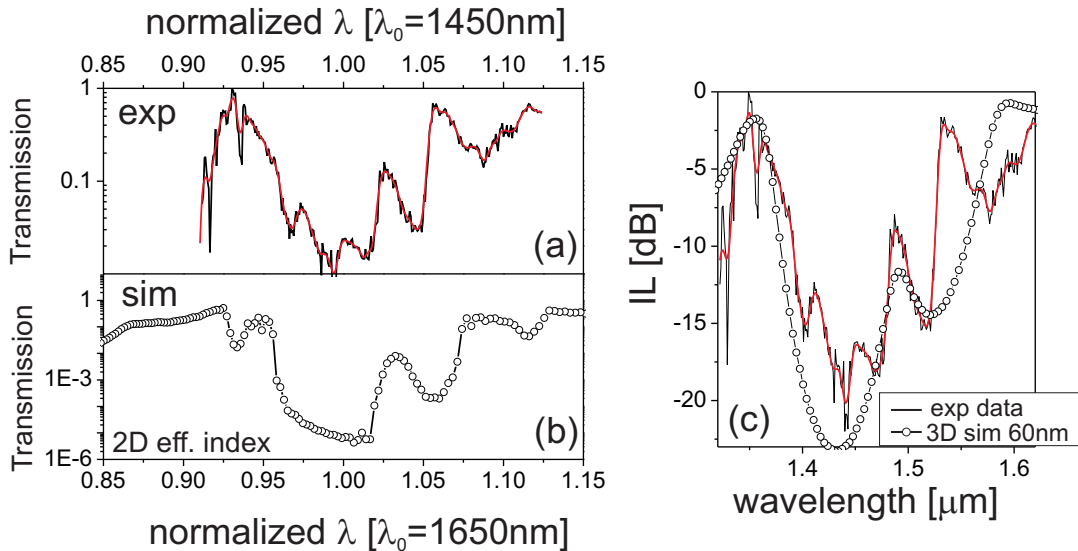


Figure 3.10: Comparison between experimental (a) and simulated (b) transmission curves in  $5c$ ,  $8\Lambda\text{m}$  CROW device. The simulations have been performed employing a 2D effective index approximation. (c): Insertion losses of the photonic crystals normalized to the straight slot waveguide. The 3D full simulations of a single cavity device is added for comparison.

measurement is reported, in which it is possible to observe an extinction ratio of 20 dB in the band gap. This has been evaluated normalizing on a straight waveguide and thus represents the photonic crystal insertion losses. In the same panel a comparison with a full 3D FDTD simulation of a single cavity device is reported. In this case, the resonant peak is centered at  $1.5 \mu\text{m}$ , as expected and have to be corrected for the different realized geometry ( $\sim 60 \text{ nm}$  red-shift). When this is done, resonant gap and defect mode are found to be quite similar to the experimental ones.

While it has been possible to realize CROW devices on underlying slot waveguides, with the advantage of small footprints and direct integration in optical chips, this particular geometry does not represent the best structure to be employed for nonlinear optics experiments. When the etching process includes the slot core, usually high losses are expected: the chosen full-trenches geometry, which is the only possible in horizontal slot waveguides, intrinsically increases the photonic crystal insertion losses. On the other hand, vertical slot waveguides would offer alternative approaches to the photonic crystal design in which the slot material is not directly perturbed [106], but they suffer more from processing related issues, which causes very large propagation losses ( $\sim 20 \text{ dB/cm}$ ) even in un-patterned waveguide. Thus, the use of whispering gallery mode cavities such as ring or disk [94, 114] could represent a more effective strategy to slow down the light. Interesting is the possibility to have a real planar photonic crystal waveguide (PhCW), in which the waveguide mode is a defect itself (bandgap-guiding), in opposite to the index-guiding structures here presented [109]. It is possible to design a single air slot in the PhCW. Filling the trench with the active materials, sensing [115] or nonlinear optics applications [116] can be accessed. In these structure, even if the footprint is increased due to the planar nature of the photonic crystal, a better control of the losses and band tuning is possible, increasing the feasibility to have working devices.

The possibilities induced by field localization effect in slot waveguides are appealing to precisely control the Local Density of States (LDOS) in a waveguide system. In the next section, some discussions are reported about photonic crystal vertical slot waveguides in which a large number of emitters is efficiently coupled to a large DOS Bloch mode.

## 3.2 LDOS, Purcell factor and superradiance in Si-patterned slot waveguides

As discussed in sec. 2.1.2, light control at the nanoscale can deeply influence the optical properties of emitters within the dielectric. It is a well known fact that the DOS depends directly from the velocity of the wavepacket: for example, the 3D DOS in a homogeneous material is directly proportional to the cube of refractive index:

$$\rho_{bulk} = \omega^2 n^3 / \pi^2 c^3, \quad (3.6)$$

which, in this case, is equal to the group index itself,  $n = n_g$ . In complex dielectrics more complicated expressions for the DOS hold, yet they are all characterized by an

inverse proportionality with the group velocity. In a slow-light system it is therefore expected to have a huge enhancement of the spontaneous emission rate, as can be seen from Fermi's golden rule, reported in eq. (2.10) [117]. The usual hindrances to the observation of the Purcell enhancement reported in sec. 2.1.2 hold: while most of these can be overcome choosing an appropriate emitter with the desired optical properties, usually the spatial correction effect can not be avoided when a large number of emitters is considered. Unavoidably, some of the emitters uniformly distributed within the dielectric will fall in proximity of an optical field node: in this points the DOS goes to zero, completely losing the enhancement effect. In fact, the main research line in Purcell enhanced, slow-light devices, regards single photon sources, in which a single emitter is placed as close as possible to a field antinode [100, 101]. At processing stage, it is extremely difficult to place an emitter in a chosen spatial position: both AFM manipulation [118] and post-processing techniques [119] are based on statistical approach and can be done at expense of reproducibility. While single photon sources can be interesting to study many quantum mechanics related effects, such as photon entanglement, opening the route towards quantum computing and cryptography, some collective phenomena which involve a large number of interacting particles can not be observed.

In the following a proposal for a slow-light photonic crystal waveguide in which a large number of emitters can be safely placed in the proximity of a field anti-node is presented. Using simple infiltration techniques, all the deposited particles can be put in optical region with large DOS. Using the Green's tensor formalism, a calculation of the Local Density of States (LDOS) and thus the local Purcell factor is reported [117, 120]. The possibility to couple many emitters to the very same optical Bloch mode sounds promising for the observation of widely studied collective phenomena, such as superradiance (SR) in proximity of a photonic band gap [99].

### LDOS and Purcell factor

When a photonic crystal is realized on an underlying optical waveguide, the mode dispersion is strongly affected by the dielectric periodicity. While often the Bloch mode related to a defect is used to achieve small group velocities, in principle the Bloch modes relative to bandgap edges can be used to the same end. As reported, for example in fig. 3.3, these modes can show very low group velocities with a corresponding large DOS.

Here a Si wire waveguide with periodic trenches is presented. Figure 3.11 (b) reports a schematic of the structure. In each period three trenches are present: these can be air holes which can be infiltrated with colloidal particles or alternatively can be filled, at the processing stage, with rare earth based materials, like Er-doped SiO<sub>2</sub>. For the case study here presented, the geometrical parameters have been optimized to localize the third photonic band in the NIR range, at the same time maximizing the optical field within the trenches, for reasons which will become apparent later. In tab. 3.1 the geometrical parameters of the waveguide are reported.  $n_{wg}$  and  $n_{tr}$  indicates, respectively, the waveguide and trenches refractive indices. Even if the eventual waveguide height is reported, unless otherwise stated, the proof of concept simulations regard a 2D waveguide with  $h \rightarrow \infty$ . This allows faster simulations in

| Parameter | [nm] | Parameter | [nm] |
|-----------|------|-----------|------|
| $\Lambda$ | 370  | W         | 1000 |
| $t_{int}$ | 150  | $t_{ext}$ | 120  |
| tt        | 260  | h         | 500  |
| $n_{wg}$  | 3.45 | $n_{tr}$  | 1.45 |

Table 3.1: Geometrical parameters for the Si patterned waveguide used as case study.

which the main physical features can be described, whereas the passage to the full 3D calculation does not change the physics involved but requires huge computational efforts.

Figure 3.11 (a) reports the firsts quasi-TE photonic bands, while the relative Bloch mode electric field intensity in the point  $[0, 0, 0.5]2\pi/\Lambda$ , is reported in panel (b) for the geometry described in tab. 3.1. As can be inspected, while the fields relative

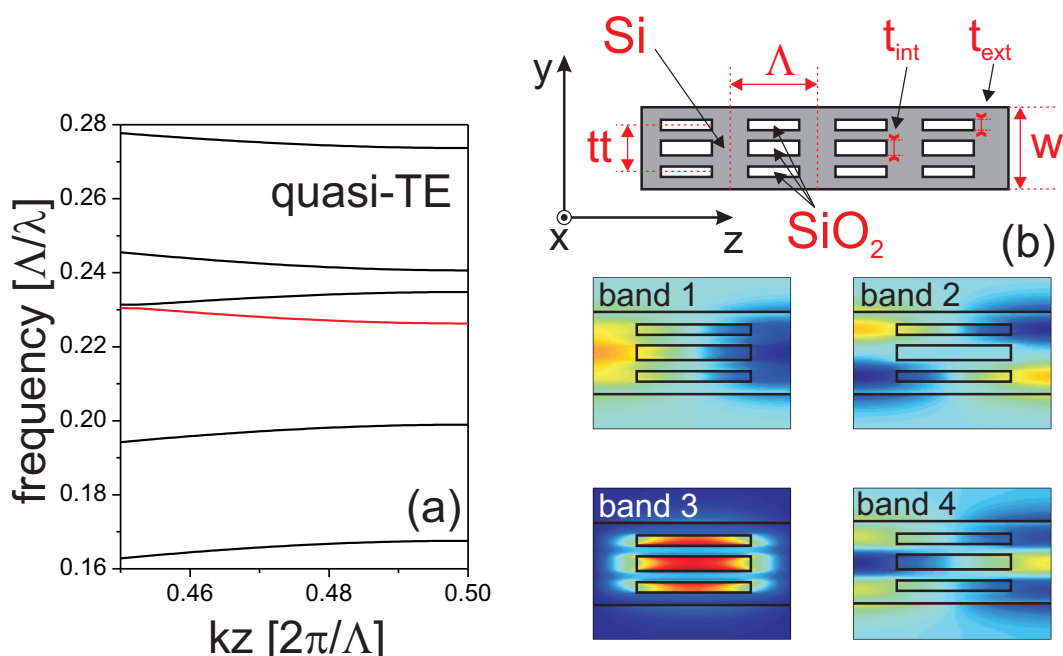


Figure 3.11: (a): Band structure in quasi-TE polarization for the geometry described in tab. 3.1. (b): Schematic of the photonic crystal waveguide and Bloch mode electric field amplitude for the first four bands in the reciprocal point  $[0, 0, 0.5]$

to the first, second and fourth bands localize mainly in the high index dielectric, with a node in the center of the trenches, band three field exactly localizes within the trenches, with a field antinode in the center of the fundamental cell. Adding to that, the steep refractive index difference between Si and SiO<sub>2</sub> guarantees a slot effect, with an enhancement of the Bloch mode electric field, as discussed in the last section. Since it is possible to localize the active, emitting particles within the trenches, it is expected a maximum coupling between material emission and the Bloch mode of the third band. Moreover, it is possible to observe that a small group velocity is expected in the proximity of bandgap edge, resulting in a large DOS. It is important to point out that in this case the spatial average does not represent a

strong hindrance towards the observation of large Purcell factor, since no field antinodes are present in the region where active particles are placed. In the following, quantification of the Purcell factor in such structure is reported, where the Green's tensor formalism has been used to obtain the Local Density of States (LDOS). The latter represents a spatial map of the density of states. The standard DOS can then be obtained by integrating LDOS in the photonic crystal fundamental cell [120]. The electromagnetic Green's tensor  $G_{ij}$  is widely exploited in computational electromagnetism due to its link with the local density of states [63]:

$$\text{LDOS}(\vec{r}, \omega) \propto \Im[\text{Tr}(G_{ij})]|\vec{r}, \quad (3.7)$$

where

$$G_{ij} = \begin{pmatrix} E_{xx} & E_{xy} & E_{xz} \\ E_{yx} & E_{yy} & E_{yz} \\ E_{zx} & E_{zy} & E_{zz} \end{pmatrix}, \quad (3.8)$$

with  $E_{ij}$  electric field components and where  $\Im$  indicates the imaginary part. In Appendix a more detailed discussion on the calculation technique is reported. The Green's tensor determination can be performed both in analytical [117] and numerical ways [121]. The analytical method is based on the decomposition of the optical field in a guided Bloch mode ( $\vec{E}_{bound}$ ) and a radiative contribution ( $\vec{E}_{rad}$ ) [100]. The analytical shape of the Bloch mode  $\Psi$  is that of eq. (3.4), where the optical field in the fundamental cell has been obtained employing the plane-wave expansion algorithm [105]. The Green's tensor for this mode is then given by [117]:

$$G_{bound} = i \frac{\Lambda \omega}{2v_g} [\Psi_{\vec{k}}(\vec{r}) \times \Psi_{\vec{k}}^*(\vec{r})]. \quad (3.9)$$

Since the Green's tensor for a homogeneous material is well known,  $i\omega^3\sqrt{\epsilon}/(6\pi c^3)$ , it is straightforward to derive an expression for the Purcell factor [100] as a function of spatial position  $\vec{r}$ :

$$F_P(\vec{r}) = \frac{3\pi c^3 \Lambda}{\omega^2 \sqrt{\epsilon} v_g} |u_{\vec{k}}(\vec{r})|^2, \quad (3.10)$$

where  $u_{\vec{k}}$  has been normalized in such a way to hold,  $\int \epsilon(\vec{r}) |u_{\vec{k}}(\vec{r})|^2 d\vec{r} = 1$ . For the sake of discussion polarization mismatch effects have been neglected. Figure 3.12 (a) shows  $F_P(\vec{r})$  analytically evaluated for the third band Bloch mode of fig. 3.11 (a), in the reciprocal point  $[0, 0, 0.5]2\pi/\Lambda$ .  $F_P$  reaches a maximum value of about 60 but, more importantly, the enhancement effect is tightly localized within the trenches where the active material is, while it is practically negligible outside. In panel (b),  $F_P$  spectral trend along the same band is reported. Moving away from the Brillouin zone edge, the group velocity becomes larger with a corresponding decrease in  $F_P$ . While the analytical method does not require important computational efforts for  $F_P$  determination, it lacks the ability to determine Green's tensor for radiative non-guided modes. Indeed, this contribution can be very important in structures in which the photonic bands folds above the light line, with corresponding large radiative losses.

Numerical determination of Green's tensor in finite-size photonic crystals, with

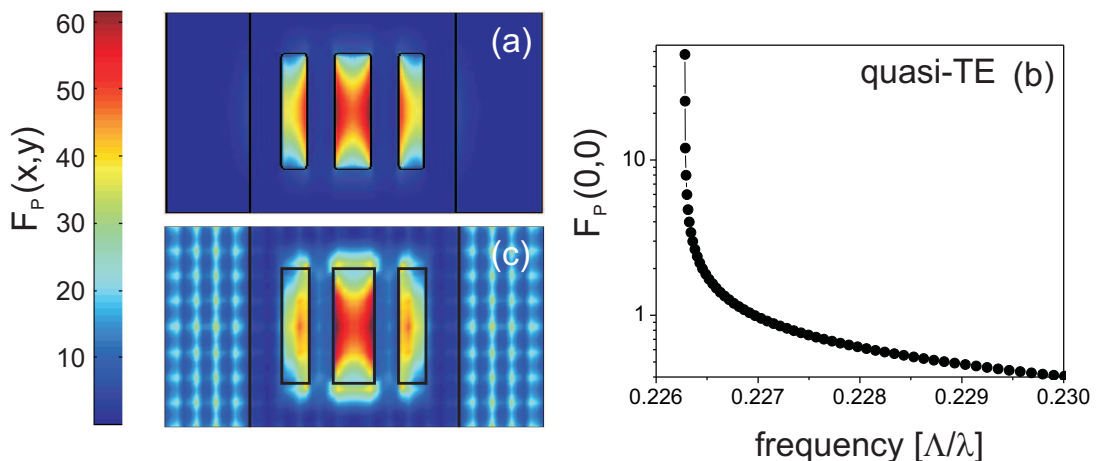


Figure 3.12: (a):  $F_P(x,\vec{y})$  obtained with analytical Green's tensor method for the third band Bloch mode described in fig. 3.11 (a) in reciprocal point  $[0, 0, 0.5]$ . For the point in the center of the cell  $F_P(0, 0; \omega)$  has been determined and reported in panel (b). (c):  $F_P(x,\vec{y})$  obtained with numerical Green's tensor method employing a FDTD algorithm. The cell and photonic features sizes are reported in tab. 3.1.

FDTD algorithms, collects all the contribution coming from bound and radiative modes. An accurate description of the method can be found in Appendix. It is interesting to compare results of fig. 3.12 (a) with the FDTD obtained LDOS when a fundamental cell with Bloch boundary conditions (i.e. infinite periodicity) is considered.

Note that in this case, while the radiative contribution is present, it represents a transient which does not survive for long simulation running time. Only the field harmonics which satisfy Bloch boundary conditions can eventually coconstructively interfere with themselves, generating long-lasting contributions. These are practically the modes related to the band structure of fig. 3.11 (a). Figure 3.12 (b) reports the final result. Since Green's tensor has a punctual nature (see Appendix), the map has been obtained scanning the entire cell with 900 different simulations, in which the LDOS was calculated point-by-point. While an interference-pattern due to the finite size of simulation cell can be noticed, the main fields features are well reproduced with numerical methods.

In finite-size devices, it is possible to compare numerical and analytical methods to calculate how much of the emitted field is coupled to a Bloch mode. This is done evaluating the coupling constant  $\beta$ , defined considering different rates which can constitute the recombination paths of an emitter placed in the structure. In particular:

$$\beta = \frac{\Gamma_{bound}}{\Gamma_{bound} + \Gamma_{rad} + \Gamma_{nrad}}, \quad (3.11)$$

where  $\Gamma_{bound}$  and  $\Gamma_{rad}$  represent, respectively, the decay into a Bloch and a radiative mode.  $\Gamma_{nrad}$  represents a non-radiative contribution, which will be neglected for the sake of discussion<sup>3</sup>. If a finite-size photonic crystal is considered, it is possi-

<sup>3</sup>In principle, it is possible to consider a low-temperature regime where, in many cases,  $\Gamma_{nrad} \rightarrow 0$ . Moreover some material, like Er-doped  $\text{SiO}_2$  can reach very low values of  $\Gamma_{nrad}$  thanks to

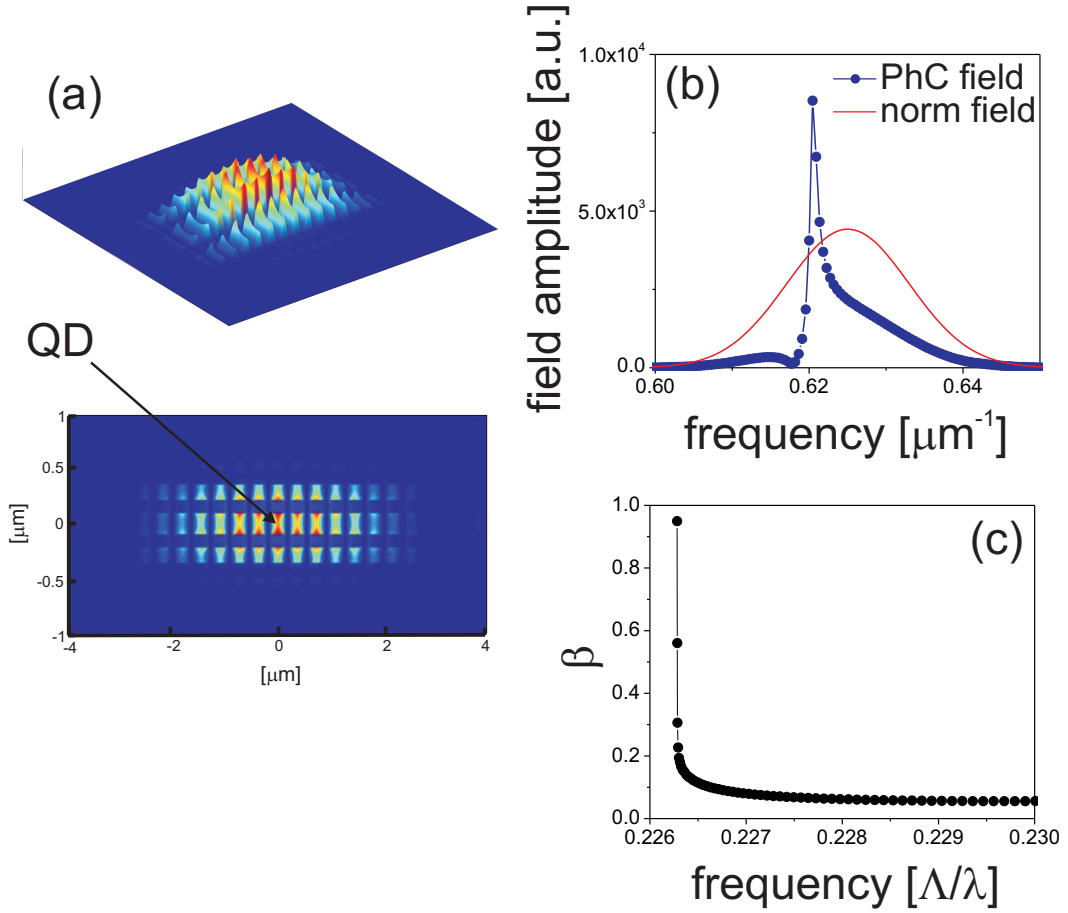


Figure 3.13: (a): Quasi-TE electric field generated by placing a single QD source in the center of a 16 periods photonic crystal whose geometry is described in tab. 3.1. (b): Comparison between the electric field spectral shape of the source when placed in vacuum or embedded in the photonic crystal. Note the strong field enhancement in proximity of the band edge. (c): Calculated  $\beta$  value.

ble to compare LDOS's and  $F_P$ 's calculated by analytical and numerical methods, which respectively considers only the bounded contribution and the total contribution terms.

Figure 3.13 (a) reports the quasi-TE optical field generated by placing a single emitter, like a QD, in the center of a 16-periods ( $16\Lambda$ ) photonic crystal. As expected, a clear field enhancement is found within the trenches, which progressively decreases moving towards the waveguide edges [101]. The Fourier transforms of the time-evolution imaginary field amplitudes of identical sources, respectively embedded in the photonic crystal and in vacuum, are reported in panel (b). As described in appendix, these are directly proportional to their relative Green's tensors. While the pulse in vacuum appears as a gaussian function, the inhomogeneous DOS generated by the complex photonic environment strongly modifies the pulse spectral shape, with a large field enhancement which can be related to band edge proximity effect. Finally, fig. 3.13 (c) reports the obtained  $\beta$  value in the center of the structure.

---

post-annealing treatments.

Close to the bandgap edge  $\beta$  can reach extremely large values, which are clearly reduced moving towards the structure edges. The  $\beta$  factor here calculated takes into account light propagation both in the forward and backward direction, resulting in roughly 50% of emitted photons which can be collected considering a single waveguide output.

The same results which have been described in 2D waveguides still hold when a full, 3D Si waveguide is considered. With the analytical method previously described, it is possible to determine the Purcell factor in the fundamental 3D cell.

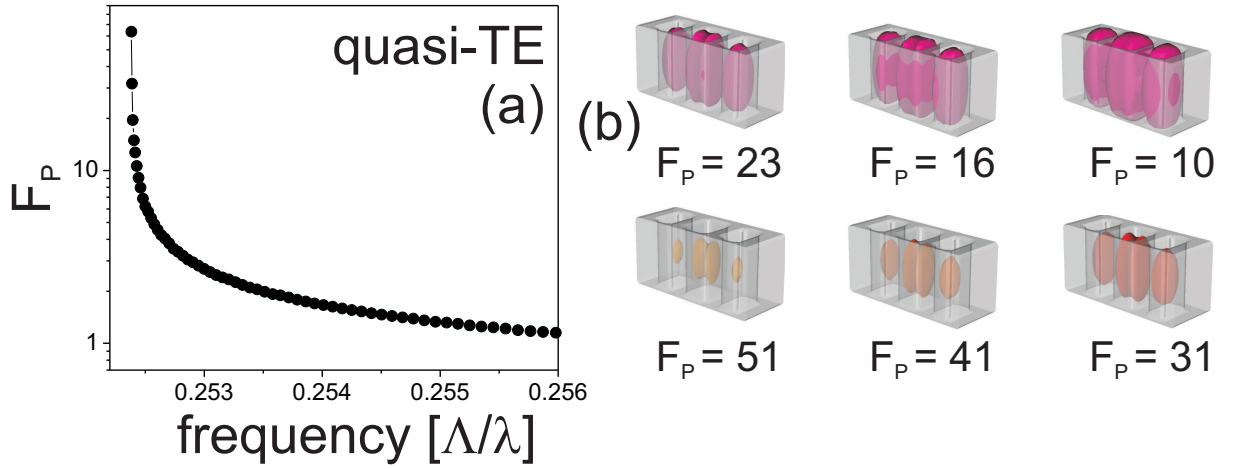


Figure 3.14: (a): Spectral Purcell factor calculation for a 3D infinite photonic crystal waveguide. (b): Isosurface corresponding to different Purcell factors.

fundamental cell. The values obtained are comparable with the ones reported in fig. 3.12 for 2D waveguides.

Even in 3D, it is possible to employ the LDOS to get spatial maps of  $F_P$ : as example in fig. 3.14 (b) the isosurfaces related to different values of  $F_P$  are reported. It is worth to note that every emitter placed in the trenches experience a Purcell factor greater than 16, at least in the ideal, infinite system.

If, as a title of example,  $\text{Er}^{3+}$  doping is considered, a maximum ions concentration of about  $1 \times 10^{20} \text{ cm}^{-3}$  is achievable with negligible ions-clusterization effects. With such a doping level, it is possible to localize about  $1 \times 10^6$  particles within the three trenches of the photonic crystal fundamental cell, where, though in a narrow spectral range, they can experience spontaneous emission enhancement.

The possibility of couple so many particles together with the same optical mode, suggests the use of this kind of waveguide as a platform to observe collective phenomena such as superradiance. In the following, the feasibility to observe this mechanism is discussed considering, as a proof of concept, Er-doped  $\text{SiO}_2$  as active material.

## Feasibility of SR observation for rare earth ions

In 1954, Dicke pointed out that the spontaneous emission in a gas can not be described as the sum of separate single particle processes, whereas all the atoms/molecules interact with a common radiation field. This acute observation triggered, some years ago, a focused research to investigate the regime described by Dicke, in which the spontaneous emission of many emitters produces a single state of coherent radiation (for a review, see [123]). This phenomenon, known in literature as superradiance (SR) or superfluorescence, is particularly interesting since it allows the production of laser-like light without the need of a resonant cavity nor of a probe signal through which stimulated emission can be generated. The signature of the onset of the regime is a PL intensity signal proportional to  $N^2$ , where  $N$  is the number of superradiating emitters. If collective effects are not considered, a familiar PL intensity signal proportional to  $N$  is then expected.

While in the 80's this collective effect has been observed in the physical systems described by Dicke, which are atomic/molecular gases, recently the same phenomenon has been proven to exist in QDs systems [124]. Moreover, complete theoretical models have been realized to investigate the SR mechanism when a collection of atoms is placed within a photonic band-gap material [102, 125]. The DOS deformation induced by the periodic structure strongly modifies the radiation field, with a corresponding alteration of the SR process. The latter can then generate a PL intensity pulse which is proportional to  $N^3$  in 3D, anisotropic band-gap systems.

In the following a case study for the possible observation of SR mechanism in photonic crystal waveguides is reported. The chosen emitting material is Er-doped  $\text{SiO}_2$ , being the ion spontaneous emission in the NIR spectral range with a long-living metastable level ( $\sim$  ms) (for more informations about  $\text{Er}^{3+}$  optical properties, see chapt. 1). Additionally, the nonradiative recombination rate can be very low if ions clusterization is avoided, while inhomogeneous line broadening is less severe than in QD systems, where a large particle size dispersion is always present.

Even though the theoretical framework to describe the SR phenomena can be quite complicated, in this applied work only a little formalism is needed to get some insights about the physical model described by Dicke.

The interaction Hamiltonian between a two-level system and the radiation field, is given by [126]:

$$H_{int} = \vec{\mu}_{tot}(t) \cdot \vec{E}(t), \quad \text{where } \vec{\mu}_{tot} = \vec{\mu} \sum_{n=1}^N (b_n + b_n^\dagger), \quad (3.12)$$

with  $\vec{\mu}$  dipole moment and  $b_n$  ( $b_n^\dagger$ ) annihilation (creation) excitation operators. If a collective raising and lowering operators are defined,  $R_+ = \sum_{n=1}^N b_n^\dagger = R_1 + iR_2$  and  $R_- = \sum_{n=1}^N b_n = R_1 - iR_2$ , it is possible to describe the collective states (Dicke states) using the same algebra of angular momentum in quantum mechanics [71]<sup>4</sup>. It becomes natural, in this framework, to label the Dicke states as  $|l, m\rangle$ , where

---

<sup>4</sup>As additional hypothesis the investigated volume is considered much smaller than the cube of the radiation wavelength

$l$  is called cooperation number [122], while  $m$  represents the population inversion, defined as:

$$m = \frac{1}{2}(n_2 - n_1), \quad (3.13)$$

With  $n_2$  ( $n_1$ ) population of excited (fundamental) state.

It is possible to get the probability of emission of radiation photons ( $w_{emit}$ ) for the transition  $|l, m\rangle|vacuum\rangle \rightarrow |\psi\rangle$ , as [126]:

$$w_{emit} = (l + m)(l - m + 1)A_{21}, \quad (3.14)$$

with  $A_{21}$  Einstein's coefficient. If all the emitters are in the ground state,  $m = -N/2$ ,  $l = N/2$  and thus  $w_{emit} = 0$ . On the other hand, if, for example, half of the emitters are inverted,  $m = 0$  and  $l$  can have any value between 0 and  $N/2$ . If the latter is the case,  $w_{emit}$  reads as:

$$w_{emit} = \frac{1}{4}N(N + 2)A. \quad (3.15)$$

Note that the emission probability is proportional to  $N^2$ , as mentioned before. In this case,  $\psi$  is called a superradiant Dicke state.

The description of the system collective phenomena can be improved when the time-evolution dynamics is considered<sup>5</sup>. To get the full time-dependence of the SR emission, the so-called Dicke master equation has to be solved [126]:

$$\langle \ddot{R}_3 \rangle = -2\frac{A_{21}}{2}(1 - \langle R_3 \rangle), \quad (3.16)$$

where  $\langle R_3 \rangle$  is the mean value of population inversion operator,  $R_3|l, m\rangle = m|l, m\rangle$ .  $R_3$  is linked to the collective raising and lowering operators by the standard commutation rule for angular momentum,  $[R_i, R_j] = \epsilon_{ijk}R_k$ .

Equation (3.16) has been solved considering  $\text{Er}^{3+}$  ions in a  $\text{SiO}_2$  matrix, in a homogeneous volume with the same dimension of the trenches in the fundamental cell of the photonic crystal waveguide described in fig. 3.11.

The small volume approximation is then valid, considering a peak Er-ions emission at 1535nm. Figure 3.15 reports the obtained solutions for different  $\text{Er}^{3+}$  doping concentration, considering a fully inverted population as initial condition. It is important to point out that, in order to assure that the initial state of the system is noncoherent, excitation should be performed employing pump laser pulses faster than the SR characteristic recombination time.

SR emission is a short pulse, with a peak value of  $N^2A_{21}$ . Interestingly, not only the pulse intensity, but even the delay of the pulse depend on the particle concentration. Larger the concentration, faster and more intense the SR pulse.

Spontaneous emission can be seen as a sort of stimulated emission process triggered by the vacuum radiation field: when an emitter is embedded within a complex photonic structure, its spontaneous emission rate and radiative pattern can strongly differ from the one in homogeneous material. This has been seen in fig. 3.13, where

---

<sup>5</sup>For example, if the initial condition of full inverted population is looked upon ( $m = N/2$ ,  $l = N/2$ ), eq. (3.15) gives  $w_{emit} = 0$ , while it will be shown from the solution of Dicke master's equation (3.16) that SR emission is expected even in this case.

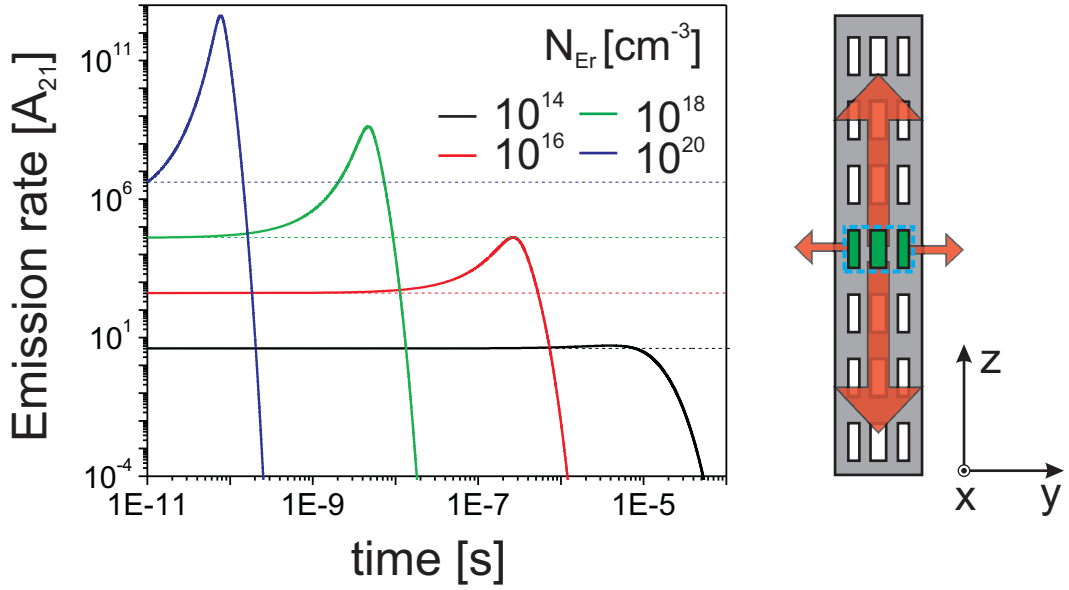


Figure 3.15: Solution of Dicke master equation (3.16) for different  $\text{Er}^{3+}$  concentrations in a homogeneous volume with the same value of the holes in the fundamental cell of the photonic crystal described in fig. 3.11. The dotted line represent the PL intensity when collective effects are neglected. A schematic of Er emission when embedded in the waveguide is added. The large coupling constant and increased DOS make the emission of SR pulse along the waveguide highly probable.

the coupling constant  $\beta$  has been considered. In the same way, it is expected that when a superradiating volume is inserted within a photonic crystal, the SR emission could acquire a non-isotropic shape, being heavily coupled with the large DOS Bloch modes. As reported in the brief sketch of fig. 3.15, it is then expected that most of superradiating emission were collected by the degenerate propagating and counter-propagating Bloch modes, whereas only a few contribution should be collected by the radiative, isotropic modes.

In this simple example the onset of SR has been analyzed considering a punctual system with very low spontaneous emission rate. In real cases, the SR regime can be reached only when the inverse of SR rate ( $\Gamma_{SR}$ ):

$$\Gamma_{SR}^{-1} = \tau_{SR} = \frac{2\pi N L^{-3} d^2 \omega}{\hbar \tau_t^{-1}}, \quad (3.17)$$

is both larger than the transit time  $\tau_t$  and smaller than the spontaneous emission lifetime, that is:

$$\tau_t \ll \tau_{SR} \ll \tau_{SE}. \quad (3.18)$$

Here, the transit time is defined as  $\tau_t = L/v_g$ , where a volume of  $L^3$  has been assumed. The symbol  $d$  represents the dipole matrix element.

The left hand side of inequality (3.18) assures that photons can leave the volume in a time shorter than interatomic correlations induction time (stimulated emission processes), while the right hand one means that collective processes happen faster

than individual relaxation of single emitters (spontaneous emission processes).

Rare-Earth deposition related issues do not allow the doping of the holes of a single cell, whereas the entire waveguide structure of fig. 3.11 can be composed by Er-doped SiO<sub>2</sub> trenches. For an infinite waveguide, if the condition (3.18) holds, each photonic crystal period is expected to generate independently a SR pulse, summing up to a total photonic crystal Bloch mode which does not possess temporal coherence.

Indeed, this situation is not likely to occur: finite size effects in real photonic crystals create different LDOS when the center or outer edges of the dielectric are considered. This fact can be exploited to produce a coherent SR pulse in a finite size photonic crystal waveguide.

Considering the case study here described, it is possible to analyze the validity of (3.18) for different Er<sup>3+</sup> concentration, when this is placed within a single cell in an infinite photonic crystal waveguide. Er<sup>3+</sup> is modeled as a two level system, where the light emission is generated by the transition  ${}^4I_{13/2} \rightarrow {}^4I_{15/2}$ . As can be seen in fig. 3.16 (a), the condition  $\tau_{SR} \ll \tau_{SE}$  is always well verified due to the long lifetime of the first excited state  ${}^4I_{13/2}$ . On the other hand, if the concentration is too large ( $> 10^{18} \text{ cm}^{-3}$ ), the transit time becomes longer than  $\tau_{SR}$  with a concomitant, non-negligible presence of stimulated emission processes.

From the results of fig. 3.16 (a), one can safely assume an infinite spontaneous emission recombination time, since this is much larger than  $\tau_{SR}$  and  $\tau_t$ . Even when the SR condition is fulfilled in a single cell, this is not enough to achieve coherent emission in the waveguide. The finite-size waveguide here considered is composed by 15 periods, which have been labeled with an increasing index, starting from -7. In this way, the Er-doped central cell is considered as the site number zero.

The different LDOS between the center and the border of the structure plays a fundamental role in this game. Consider a SR pulse emission from the central (zero) cell: if the pulse reaches the other cells before the onset of their own SR emission, the pulse will be amplified by stimulated emission, maintaining its coherence. This can be expressed considering a cell-i-to-cell-j transit time  $\tau_{t,ij}$ . This has to be shorter than the j-th cell SR time,  $\tau_{SR,j}$ . If this is not the case, more than one single SR pulse will be emitted and the coherence will be lost.

A doping of the all 15 cells is considered: likely, the SR pulse will be emitted at first in the zero cell due to its larger Purcell factor.

Figure 3.16 (b) reports  $\tau_{SR}$  and the transit time  $\tau_t$  for each of the 15 cells for a frequency of 0.2263 (band edge point), with a Er<sup>3+</sup> ions concentration of  $10^{18} \text{ cm}^{-3}$ . As confirmed by the results in panel (a), no SR emission is expected in this case, since  $\tau_{SR}$  is always shorter than  $\tau_t$ .

In panel (c) of fig. 3.16, the same comparison is done for a doping concentration of  $10^{17} \text{ cm}^{-3}$ . While each single cell reaches the SR condition, fulfilling the inequality (3.18), the transit time  $\tau_{t,01}$  is shorter than  $\tau_{SR,1} - \tau_{SR,0}$ , resulting in a SR incoherent emissions coming both from the cell 0 and from the cells 1 and -1.

In the last case of panel (d), where a doping concentration of  $10^{16} \text{ cm}^{-3}$  is considered, not only all the cells fulfill the SR condition (3.18), but each cell-to-cell transit

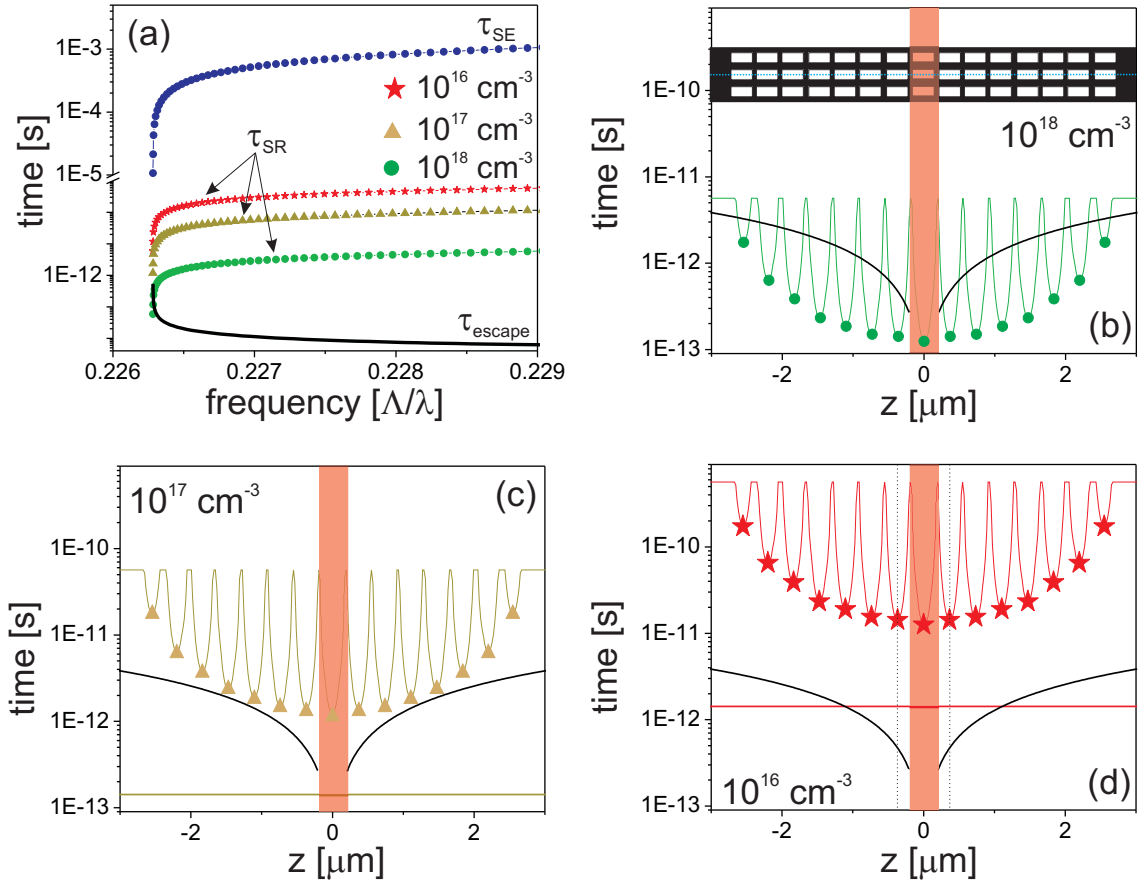


Figure 3.16: (a): Feasibility of SR emission for different frequencies considering emitters in a single cell of the infinite photonic crystal waveguide previously described. Three different  $\text{Er}^{3+}$  concentrations have been considered. (b): SR regime in a finite-size, 15 periods photonic crystal for a  $\text{Er}^{3+}$  concentration of  $10^{18} \text{ cm}^{-3}$ . (b): The same for  $10^{17}$  ions per  $\text{cm}^3$ . The dark yellow line represents the difference between  $\tau_{SR}$  in the central cell and in the first neighboring cells. (c): The same for  $10^{17}$  ions per  $\text{cm}^3$ . The red line represents the difference between  $\tau_{SR}$  in the central cell and in the first neighboring cells.

time is shorter than the SR time in the cell itself. It is then expected that a SR pulse coming from the cell 0 propagates being amplified by stimulated emission in the neighboring cells.

While in principle is then possible to have coherent pulses emission from a Si-based photonic crystal waveguide, clearly the real situation reveals more complications with respect to this simple, semiempirical model.

At first, since SR is triggered by the vacuum radiation field, it is expected that each pulse will propagate in a single direction: while all the above discussion applies considering the cells placed along the emission sense, the other half of the photonic crystals will possibly perturb the output emission with its own SR pulses. It is true that these last will be subjected to absorption in the adjacent cells, where the population inversion has been eliminated by stimulated emission induced by the first pulse. Thus, their magnitude is expected to be lower than the first, amplified SR

pulse.

Moreover, an accurate description of the dynamics should involve more detailed calculations where both optical radiative losses and nonradiative recombination rates should be implemented.

Nevertheless, considering the model of John for bandgap SR phenomena [99, 125], the peak emission intensity, in the case of an  $\text{Er}^{3+}$  concentration of  $10^{16} \text{ cm}^{-3}$  (about 500 emitters in the cell) is expected to be equivalent to the emission of  $125 \times 10^6$  independent emitters, with the additional properties of spatial directionality and coherence.

### 3.3 Conclusions

In this chapter, the interaction of slow light with nonlinear and active materials has been discussed. The possibility of slowing down the light to moderate group velocities, which are not sufficient for applications such as optical buffering and light storage, are indeed useful when the enhancement of nonlinear effects is considered. Even a group velocity of  $0.1 c$  enhances the nonlinear effects by two order of magnitude. Since the radiative losses are linearly enhanced with the group index, such delays allows to maintain acceptable insertion losses, whereas very high group index would make the device very difficult to measure. In particular, a photonic crystal has been designed on a Si-based slot waveguide, in order to maintain a small footprint and realize, by means of coupled cavities modes, an almost-flat pass band with resulting undistorted pulse propagation.

The possibility of accurately control the group velocity and spatial field localization makes this kind of structures optimal platform to observe large Purcell factors for an ensemble of many emitters, relaxing the limits imposed by spatial averaging effects, described in sec. 2.1.2. When this result is achieved, collective emission phenomena, such as QDs or Rare Earth ions superradiance, could be observed. Noteworthy, up to now these mechanisms were usually investigated mainly in atomic/molecular gases. For these reasons, I propose here a geometry where the bandgap superradiance effects proposed by John [102] can be proven and, if the theoretical prediction are confirmed, could represent a CMOS-compatible, Si-based efficient light source.

## Appendix to chapter 3

### Electromagnetic Green's tensor determination in FDTD scheme

As previously discussed, the evaluation of the electromagnetic Green's tensor reveals to be very useful for the determination of the Local Density of States (LDOS). In particular, the Green's tensor is defined as the electromagnetic system response when excited with a  $\delta$ -function:

$$\left[ \nabla^2 + \frac{\epsilon(\vec{r})}{c^2} \frac{\partial^2}{\partial t^2} \right] \overleftrightarrow{G}(\vec{r}, \vec{r}', t, t') = \overleftrightarrow{\mathbf{1}} \delta(\vec{r}, \vec{r}') \delta(t, t'), \quad (3.19)$$

where the notation  $\overleftrightarrow{\mathbf{1}}$  indicates the unit tensor. With some algebraic manipulation, it can be seen that the FDTD master equation can be written as [63]:

$$- \left[ \nabla^2 + \frac{\epsilon(\vec{r})}{c^2} \frac{\partial^2}{\partial t^2} \right] \vec{E}(\vec{r}, t) = \mu_0 \frac{\partial \vec{J}(\vec{r}, t)}{\partial t}, \quad (3.20)$$

with  $\vec{J}(\vec{r}, t)$  current density. It is straightforward to see that, in the case of:

$$\mu_0 \frac{\partial \vec{J}(\vec{r}, t)}{\partial t} = \overleftrightarrow{\mathbf{1}} \delta(\vec{r}, \vec{r}') \delta(t, t') \rightarrow \vec{J}(\vec{r}, t) = \frac{\overleftrightarrow{\mathbf{1}}}{\mu_0} \delta \vec{r}, \vec{r}' \Theta t - t', \quad (3.21)$$

then the electric field and Green's tensor exactly coincide. The source condition can be imposed considering point-like sources with a step-like turn-on, as described by the Heaviside function  $\Theta(t - t')$ . When these conditions are fulfilled, the time-dependent Green's tensor can be obtained. From that, the frequency-dependent tensor can be obtained by Fourier transform operation. The finally obtained  $\overleftrightarrow{G}(\omega, \vec{r})$  is related to the LDOS as:

$$\text{LDOS}(\vec{r}, \omega) = \frac{\omega}{\pi} \text{Norm.} \Im[\text{Tr}(G_{ij})]_{|\vec{r}}. \quad (3.22)$$

In real FDTD calculation, since  $\delta$ -functions can not be exactly realized, the system has to be properly normalized to produce realistic results. Following the procedure described in [63], considering a resolution of at least  $\lambda/40$ , the correction factor has been determined calculating the LDOS in a 2D homogeneous system for TE polarized light and comparing it with the known analytical value given by  $\rho_{2D} = \omega n^2 / \pi c^2$ . Figure 3.17 reports this comparison for different media and frequencies. As can be seen, while the non corrected calculated values strongly differ from the analytical curve, when a correction factor of  $\epsilon^4/2$  is employed, a good agreement is achieved, with a maximum discrepancy of 4%. This can be further reduced increasing more the resolution of the system. The same results have been verified for the TM polarization.

One of the most interesting advantages of FDTD method is represented by the possibility to get the field evolution in time. In this way it is possible to excite the

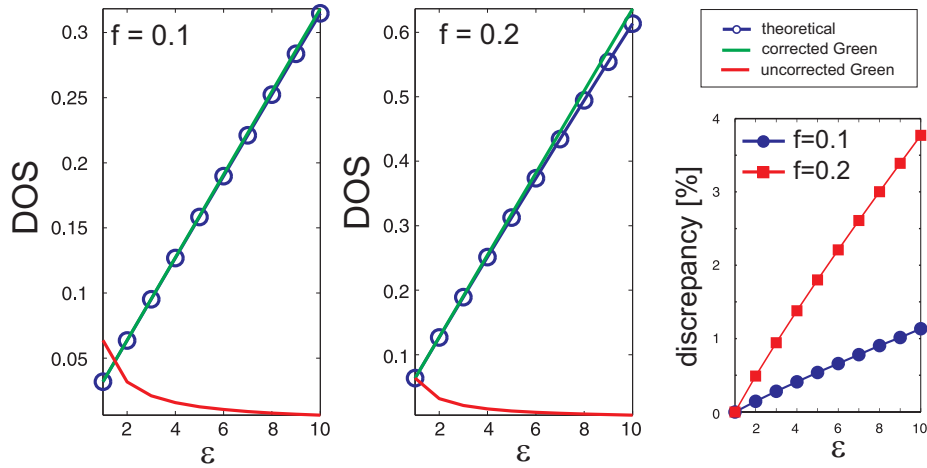


Figure 3.17: Comparison between analytical, corrected and non-corrected Green's tensor DOS determination. The discrepancy between corrected Green's tensor and analytical results is reported.

dielectric structure with a spectrally-broad, spatial  $\delta$ -like source. When the field amplitude is detected in time, in the same spatial position of the source, simple numerical implementation of Fourier transform results in the frequency-dependent Green's tensor for many different frequencies, obtained employing a single FDTD simulation.

# Conclusions and future perspectives

In this thesis, light-matter interactions in weak coupling regime have been investigated in several nanophotonic structures based on Si materials. Commonly, this research line is focused on the strong coupling regime, in which the system can be described in terms of mixed radiation-excitation eigenstates. However, even in the case of weak coupling, the reciprocal influence of electromagnetic radiation and active emitters can lead to profound modifications of the optical properties of the system. When light is influenced by matter (nonlinear optics, absorption/emission) and vice-versa (Purcell effect, superradiance) a rich physics can be investigated, both from fundamental and application point-of-views.

This particular approach could furnish the final solution for the search of integrated, CMOS compatible light source, which would allow the huge jump needed to pass from electronics-based circuitry to photons-based optical chips and computers.

In this sense my work, while exploring interesting fundamental physics effects, could be interpreted as an effort towards this final goal, which is still very far to be realized.

The first chapter of this thesis, describing material spectroscopy of Er-doped SRSO material, investigates the possibility to maintain the good emitting properties of rare earth erbium, improving its inefficient direct excitation with Silicon-nanoparticles (Si-np) sensitizers. It has been demonstrated that no intrinsic limit exists to the sensitization action. Still the most important hindrances to the net gain, that is Confined Carrier Absorption (CCA) losses and distance dependent energy transfer mechanism, have still to be solved. In fact, the huge technological efforts needed to overcome such degrading effects, like placing  $\text{Er}^{3+}$  ions spatially close to Si-np, are still challenging the modern deposition techniques.

The spectroscopic investigation, in this case, has been done without resorting to the possibility to exploit electromagnetic radiation to modify the energy transfer itself, which could represent a possible solution to increase the sensitization effect without increasing the CCA-related losses.

The second chapter deals with the physics related to resonant whispering gallery mode (WGM) cavities. These can be useful to accurately control light propagation. Interestingly, this can be partially tailored, for example considering novel WGM resonator geometry, such as the micro-kylix here presented (sec. 2.1.1). This class of

resonator offers the possibility to tune the spectral region where the largest quality factors are found of tens of nm, with an evident gain for biosensing applications or to avoid mode competition in lasing WGM microcavities.

Some applications involving light modification of material properties are then investigated (sec. 2.1.2). The increased Density of States (DOS), which can be realized by the resonant modes, can affect the material spontaneous emission, enhancing its rate by a value known as Purcell factor ( $F_P$ ). In particular,  $F_P$  has been measured for emitters far from the ideality condition (bad emitter regime), supplying the first evident proof of Purcell enhancement in Si-np based materials. Moreover, a new technique for the determination of optical constants, such as electronic emission linewidth, has been proposed.

Finally, a design to investigate novel physical phenomena in vertically-coupled resonator geometry is proposed (sec. 2.2). The feasibility to observe electromagnetic field oscillations, qualitatively similar to Josephson ones is discussed. In fact, in analogy with the oscillating current in superconductor-insulator-superconductor junction, the electromagnetic field is expected to oscillate with a frequency equal to the splitting between symmetric and anti-symmetric modes, which are known to appear when two cavities are coupled together. The physics behind is given by the effect of Kerr nonlinear materials constituting the disks; again, Si-np could represent a good candidate for this role. In this case, the matter nonlinearity influences light, with the result of interesting and possibly new physics.

In the third chapter again the influence of light over matter is discussed. When the light is slowed down with respect to its speed in vacuum, the photonic density of states is increased, due to the longer interaction time of the radiation with the surrounding environment. This effect can be exploited to enhance material nonlinear effects (sec. 3.1). In particular, the overall enhancement goes as  $(c/v_g)^2$ , with  $v_g$  group velocity of light. Even moderate slow light effects can then produce large enhancement of the effective nonlinear coefficient.

In this experiment, the light is slowed down employing modification of waveguide dispersion, which is induced by fabrication of a periodic pattern (photonic crystal) within the waveguide itself. It is interesting to consider slot waveguide as the underlying structure: in this case, due to a large refractive index contrast, an important portion of the optical field can be localized in usually non-guiding low index materials. When different photonic crystal cavity modes are coupled together, it is then possible to realize quasi-flat pass band, in which a propagating pulse can be transmitted undistorted.

Due to the possibility of precisely control the group velocity and field spatial position, a slot-waveguide based photonic crystal geometry is proposed in which many emitters can experience large Purcell enhancements (sec. 3.2). In standard devices only few emitters can feel the enhancement effect, due to limitation imposed by spatial averaging corrections terms. This geometry seems to favour the observation of collective spontaneous emission physics, also known as superradiance, in which an ensemble of  $N$  inverted emitters can be de-excited producing a fast, coherent light pulse with a PL intensity proportional to  $N^2$ . Other than interesting for the realization of an integrated light source, this platform can be used to experimentally

investigate band-gap superradiance, which offers a rich physics that, up to now, has been described only theoretically.

The line of research I have faced during my Ph. D. represents a peculiar situation. In fact, other than fascinating for the investigation of fundamental physics, it reveals a deep connection with applications, that could represent real innovations for technological advancements. If further analyzed, the strategy of exploit light-matter interaction can be successful, and eventually will allow a full tailor of both photonic and electronic devices.

# List of publications

## In international peer-reviewed scientific journals:

- **A. Pitanti**, P. Bettotti, D. Sarchi and L. Pavesi, *LDOS, Purcell factor and superradiance in silicon photonic crystal waveguides*, under preparation.
- **A. Pitanti**, M. Ghulinyan, D. Navarro-Urrios, G. Pucker and L. Pavesi, *Probing the spontaneous emission probability in Si-nc based microdisk resonators*, submitted to Phys. Rev. Lett.
- **A. Pitanti**, D. Navarro-Urrios, N. Prtljaga, N. Daldosso, F. Goubilleau, R. Rizk, B. Garrido and L. Pavesi, *Energy transfer mechanism and Auger effect in  $Er^{3+}$  coupled silicon nanoparticle samples*, submitted to J. Appl. Phys.
- D. Navarro-Urrios, Y. Lebour, O. Jambois, B. Garrido, **A. Pitanti**, N. Daldosso, L. Pavesi, J. Cardin, K. Hijazi, L. Khomenkova, F. Goubilleau and R. Rizk, *Optically active  $Er^{3+}$  ions in  $SiO_2$  co-doped with Si nanoclusters*, **J. Appl. Phys.** 106, 093107 (2009).
- R. Guider, N. Daldosso, **A. Pitanti**, E. Jordana, J. M. Fedeli and L. Pavesi, *NanoSi low loss horizontal slot waveguides coupled to high Q ring resonators*, **Opt. Expr.** 17, 20762 (2009). Erratum: *ibid.* 17, 23556 (2009).
- Z. Yuan, A. Anopchenko, N. Daldosso, R. Guider, D. Navarro-Urrios, **A. Pitanti**, R. Spano and L. Pavesi, *Silicon nanocrystals as an enabling material for silicon photonics*, **Proc. IEEE - special issue** 97, 1250 (2009).
- D. Navarro-Urrios, **A. Pitanti**, N. Daldosso, F. Goubilleau, R. Rizk, B. Garrido and L. Pavesi, *Energy transfer between amorphous Si nanoclusters and  $Er^{3+}$  ions in a  $SiO_2$  matrix*, **Phys. Rev. B** 79, 193312 (2009).
- M. Ghulinyan, **A. Pitanti**, G. Pucker and L. Pavesi, *Whispering-gallery mode micro-kylix resonators*, **Opt. Express** 17, 9434 (2009).
- D. Navarro-Urrios, **A. Pitanti**, N. Daldosso, F. Goubilleau, L. Khomenkova, R. Rizk and L. Pavesi, *Assessment of the main material issues for achieving an Er coupled to silicon nanoclusters infrared amplifier*, **Physica E** 41, 1029 (2009).
- M. Ghulinyan, D. Navarro-Urrios, **A. Pitanti**, A. Lui, G. Pucker and L. Pavesi *Whispering-gallery modes and light emission from a Si-nanocrystal-based single microdisk resonator*, **Opt. Express** 16, 13219 (2008).

- R. Adamo, A. Anopchenko, P. Bettotti, M. Cazzanelli, E. D'Amato, N. Daldosso, L. Ferraioli, E. Froner, Z. Gaburro, R. Guider, S.M. Hossain, D. Navarro-Urrios, **A. Pitanti**, S. Prezioso, M. Scarpa, R. Spano, M. Wang, L. Pavesi, *Low dimensional silicon structures for photonic and sensor applications*, **Appl. Surf. Sci.** 255, 624 (2008).
- D. Navarro, **A. Pitanti**, N. Daldosso, F. Gourbilleau, R. Rizk, G. Pucker, L. Pavesi, *Quantification of the carrier absorption losses in Si-nanocrystal rich rib waveguides at 1.54  $\mu\text{m}$* , **Appl. Phys. Lett.** 92, 051101 (2008).

### Books contributions

- A. Anopchenko, N. Daldosso, R. Guider, D. Navarro-Urrios, **A. Pitanti**, R. Spano and L. Pavesi, *Photonics application of Silicon nanocrystals*, Silicon Nanocrystals; Fundamentals, Synthesis and Applications, edited by L. Pavesi and R. Turan (Wiley-VCH Verlag GmbH, Berlin 2009)

### Conference proceedings and contributions

- **A. Pitanti**, M. Ghulinyan, M. Xie, G. Pucker and L. Pavesi, *Q-factor tuning in all-active whispering-gallery mode resonators with Si-nc*, Group IV Photonics, 6th IEEE International Conference, 9-11 September 2009.
- V. Donzella, V. Toccafondo, S. Faralli, F. Di Pasquale, **A. Pitanti**, N. Daldosso, L. Pavesi, F. Gourbilleau and R. Rizk *Er-doped Si nanoclusters waveguides longitudinally pumped by broad area lasers for optical amplification*, SPIE Photonic North 2009 Proceedings, 7386 (2009).
- M. Ghulinyan, **A. Pitanti**, M. Xie, G. Pucker and L. Pavesi, *Silicon-nanocrystal-based whispering-gallery mode micro-Kylix resonators*, ICTON 2009 Special session - Microresonator and Photonic Molecule: trapping, harnessing and releasing light, São Miguel, Azores (Portugal), 28 June - 2 July 2009.
- G. Pucker, M. Ghulinyan, **A. Pitanti**, M. Xie, D. Navarro-Urrios, A. Lui, L. Pavesi and A. Simoni, *Silicon quantum dots in microdisk resonators: Whispering-gallery modes, stress-induced Q-factor tuning and enhancement* (invited talk), SPIE Symposium on Microtechnologies for the New Millennium, Dresden (Germany), 4-6 May 2009.
- **A. Pitanti**, D. Navarro-Urrios, R. Guider, N. Daldosso, L. Khomenkova, F. Gourbilleau, C. Oton, W. Loh, R. Rizk, O. Jambois, B. Garrido and L. Pavesi, *Er<sup>3+</sup> coupled to Si nanoclusters rib waveguides*, Group IV Photonics, 5th IEEE International Conference, 17-19 September 2008.
- **A. Pitanti**, P. Bettotti, E. Rigo, R. Guider, N. Daldosso, J.M. Fedeli and L. Pavesi, *Coupled cavities in one-dimensional photonic crystal based on horizontal slot waveguide structure with Si-nc*, Group IV Photonics, 5th IEEE International Conference, 17-19 September 2008.

- M. Ghulinyan, D. Navarro-Urrios, **A. Pitanti**, A. Lui, G. Pucker, and L. Pavesi, *Whispering-gallery modes and Purcell effect in a Si-nanocrystal-based single microdisk resonator*, Group IV Photonics, 5th IEEE International Conference, 17-19 September 2008.
- **A. Pitanti**, D. Navarro-Urrios, R. Guider, N. Daldosso, F. Gourbilleau, L. Khomenkova, R. Rizk and L. Pavesi, *Further improvements in  $Er^{3+}$  coupled to Si nanoclusters rib waveguides*, SPIE Photonic Europe 2008 Proceedings, 4669-44 (2008).
- N. Daldosso, D. Navarro-Urrios, **A. Pitanti**, F. Gourbilleau, R. Rizk and L. Pavesi, *Erbium and Silicon nanocrystals for light amplification*, Lasers and Electro-Optics Society, 2007. LEOS 2007. The 20th Annual Meeting of the IEEE, 21-25 October 2007 Page(s): 933-934 (2007)
- D. Navarro-Urrios, **A. Pitanti**, L. Ferraioli, N. Daldosso, F. Gourbilleau, R. Rizk, L. Pavesi, *Assesment of the Excited carrier absorption losses in Si-nc rib-waveguides*, Group IV Photonics, 4th IEEE International Conference, 19-21 September 2007 Page(s):1 - 3 (2007).
- O. Anopchenko, P. Bettotti, M. Cazzanelli, N. Daldosso, L. Ferraioli, Z. Gaburro, R. Guider, D. Navarro-Urrios, **A. Pitanti**, S. Prezioso, R. Spano and L. Pavesi *Low dimensional silicon to enable silicon photonics*, Highlights on Spectroscopies of Semiconductors and Nanostructures, Conference Proceedings - Italian Physical Society, Editrice Compositori; 1999, vol 94, pages 231-242, ISSN 1122-1437 (2007)
- O. Anopchenko, P. Bettotti, M. Cazzanelli, N. Daldosso, L. Ferraioli, Z. Gaburro, R. Guider, S. Minhaz, D. Navarro-Urrios, **A. Pitanti**, S. Prezioso, R. Spano, J. Wang e L. Pavesi *Nanocristalli di Silicio: potranno permettere una fotonica basata sul Silicio ?*, FOTONICA 2007, 21-23 Maggio 2007.

# Acknowledgments

When you finish your Ph.D. you have commitments towards many gentlemen who have helped you getting the title *Philosophiae Doctor*. This is the place where credits are due: so get comfortable and let me thank who deserve it. My first thought goes to prof. Pavesi. I still remember his inspiring speech the first day of Ph.D., and hope that he appreciated the way I have interpreted it. His experience has helped me a lot, and he absolutely deserves my first thank. Dani cannot be merely catalogued as the person who taught me how to do research. He has been a mentor and a colleague but above all, a friend. He helped me a lot during the most difficult year in my life and if now I still possess some mental equilibrium it is also his merit. How to forget Romain, who has been my *compagno di sventura* during these three long years? I will really miss the beers, the movies, the bitter jokes and everything else. Don't come back to France, Italy needs you! With Paolo and Mher I've spent countless hours respectively speaking about physics and doing physics in the lab. My best hopes are to go on dealing with you guys, maybe collaborating together in some scientific projects. If some times I've tried to play some theoretical physics, I need to thank Iacopo and Davide (especially Davide, who I have bothered really a lot!). Of course, my bests go to all nanoscience lab., especially to Niko and Ale, which I'm going to visit again next year, maybe for a sledge race. Many research groups and EC funding have to be properly addressed. I wish to thank FBK AP&P lab., UB-MIND, ORC, CIMAP, SSSUP, CEA-LETI and all the researchers who participated in LANCER project.

Per i ringraziamenti non lavorativi, penso che l'italiano suoni meglio. La mia famiglia va ringraziata al primo posto. Sono stati anni difficili, ma siete riusciti a non farmi pesare la lontananza: grazie Mamma, Nicola e Lorenzo. Mio padre non è qui di persona, ma senza il suo contributo chissà dove sarei adesso. Grazie per tutto quello che hai fatto per me. Ringrazio Elisa, soprattutto per avermi dato una meta da raggiungere: riuscirò a sciare più veloce di te! Tra gli amici toscani Giorgio, Chicca e Seba non possono mancare. Molte delle persone ringraziate sopra dovrebbero essere incluse anche in questa categoria: ragazzi lo sapete, ed è superfluo nominarvi ancora.

Infine ringrazio la vicina al telefono che mi ha fatto compagnia tutti i giorni. ~~Anche se non leggerà mai neanche una riga di questa tesi~~ (malfidato!), ha fatto per me più di tutti gli altri messi insieme.

Non scorderò i miei anni a Trento e spero che non vi scordiate tanto presto di me. Hasta luego!



# Bibliografia

- [1] J. H. Davies, *The physics of low-dimensional semiconductors. An introduction.*, Cambridge University Press (1998).
- [2] L. Pavesi, L. Dal Negro, C. Mazzoleni, G. Franzo and F. Priolo, *Nature*, **408**, 440 (2000).
- [3] G. E. Moore, *Electronics* **38**, # 8 (1965).
- [4] P. C. Becker, N. A. Olson, J. R. Simpson, *Erbium doped fiber amplifier: fundamental and technology*, Academic Press (1999).
- [5] A. J. Kenyon, C. E. Chryssou and C. W. Pitt, *Appl. Phys. Lett.* **76**, 688 (2000).
- [6] L. Pavesi and D. J. Lockwood, *Silicon photonics*, Topics in applied physics - Springer (2004).
- [7] C. Canali, C. Jacoboni, F. Nava, G. Ottaviani and A. A. Quaranta, *Phys. Rev. B* **12**, 4 (1975).
- [8] D. Kovalev, H. Heckler, M. Ben-Chorin, G. Polisski, M. Schwartzkopff and F. Koch, *Phys. Rev. Lett.* **81**, 2803 (1998).
- [9] M. V. Wolkin, J. Jorne, P. M. Fauchet, G. Allan and C. Delerue, *Phys. Rev. Lett.* **82**, 197 (1999).
- [10] L. Khomenkova, F. Gourbilleau, J. Cardin and R. Rizk, *Physica E* **41**, 1048 (2009).
- [11] M. Zacharias, J. Heilmann, R. Scholz and U. Kahler, *Appl. Phys. Lett.* **80**, 661 (2002).
- [12] H. Han, S. Seo and J. Shin, *Appl. Phys. Lett.* **79**, 4568 (2001).
- [13] M. Fujii, K. Imakita, K. Watanabe and S. Hayashi, *J. Appl. Phys.* **95**, 272 (2004).
- [14] I. Izeddin, A. S. Moskalenko, I. N. Yassievich, M. Fujii and T. Gregorkiewicz, *Phys. Rev. Lett.* **97**, 207401 (2006).
- [15] O. Savchyn, F. R. Ruhge, P. G. Kik, R. M. Todi, K. R. Coffey, H. Nukala and Helge Heinrich, *Phys. Rev. B* **76**, 195419 (2007).

- [16] D. Navarro-Urrios, Y. Lebour, O. Jambois, B. Garrido, A. Pitanti, N. Daldosso, L. Pavesi, J. Cardin, K. Hijazi, L. Khomenkova, F. Gourbilleau and R. Rizk, *J. Appl. Phys.* **106**, 093107 (2009).
- [17] A. Pitanti, D. Navarro-Urrios, R. Guider, N. Daldosso, F. Gourbilleau, L. Khomenkova, R. Rizk, and L. Pavesi *Proc. SPIE* **6996**, 699619 (2008).
- [18] P.K.Tien, R.Ulrich and R.J.Martin, *Appl. Phys. Lett.* **14**, 291 (1969).
- [19] L. Khriachtchev, M. Räsänen, S. Novikov and L. Pavesi, *Appl. Phys. Lett.* **85**, 1511 (2004).
- [20] O. Savchyn, R. M. Todi, K. R. Coffey, and P. G. Kik, *Appl. Phys. Lett.* **93**, 233120 (2008).
- [21] L. Pavesi and M. Ceschini *Phys. Rev. B* **48**, 17625 (1993).
- [22] J. Linnros, N. Lalic, A. Galeckas and V. Grivickas *J. Appl. Phys.* **86**, 6128 (1999).
- [23] M.N. Berberan-Santosa, E.N. Bodunov and B. Valeur *Chem. Phys.* **315**, 171 (2005).
- [24] R. M'ghaieth, H. Maâref, I. Mihalcescu and J. C. Vial, *Phys. Rev. B* **60**, 4450 (1999).
- [25] S. Godefroo, M. Hayne<sup>1</sup>, M. Jivanescu, A. Stesmans, M. Zacharias, O. I. Lebedev, G. Van Tendeloo and V. V. Moshchalkov, *Nat. Nanotechnol.* **3**, 174 (2008).
- [26] D. Kovalev, J. Diener, H. Heckler, G. Polisski, N. Künzner, and F. Koch, *Phys. Rev. B* **61**, 4485 (2000).
- [27] D. L. Dexter, *J. Chem. Phys.* **21**, 836 (1953).
- [28] K. Choy, F. Lenz, X. X. Liang, F. Marsiglio, and A. Meldrum, *Appl. Phys. Lett.* **93**, 261109 (2008).
- [29] W. J. Miniscalco, *J. Lightwave Technol.* **9**, 234 (1991).
- [30] B. Garrido, C. García, P. Pellegrino, D. Navarro-Urrios, N. Daldosso, L. Pavesi, F. Gourbilleau and R. Rizk *Appl. Phys. Lett.* **89**, 163103 (2006).
- [31] D. Navarro-Urrios, A. Pitanti, N. Daldosso, F. Gourbilleau, R. Rizk and L. Pavesi *Phys. Rev. B* **79**, 193312 (2009).
- [32] R. Hull, *Properties of crystalline Silicon*, Academic Press (1999).
- [33] F. Gourbilleau, R. Madelon, C. Dufour and R. Rizk *Opt. Mater.* **27**, 868 (2005).
- [34] See for example J. R. Lakowicz, *Principles of Fluorescence Spectroscopy* 3rd ed., Springer, New York, 2006, and references therein.

- [35] M. J. A. de Dood, L. H. Slooff, A. Polman, A. Moroz and A. van Blaarderen, *Phys. Rev. A* **64**, 033807 (2001).
- [36] B. Saleh and M. Teich, *Fundamentals of photonics*, 2nd ed., Wiley Series in pure and applied optics, 2007.
- [37] M. Lohmeyer, *Opt. Quant. Electron.* **29**, 907 (1997).
- [38] J.Valenta, I.Pelant and J.Linnros, *Appl. Phys. Lett.* **81**, 1396 (2002).
- [39] K. L. Shaklee, R. F. Leheny and R. E. Nahory, *Phys. Rev. Lett.* **26**, 888 (1971).
- [40] O. A. Vlasenko, E. M. Zolotov, R. F. Tavlykaev, *Sov. J. Quant. Electron.* **19**, 681 (1989).
- [41] D. Navarro-Urrios, A. Pitanti, N. Daldosso, F. Gourbilleau, R. Rizk, G. Pucker and L. Pavesi, *Appl. Phys. Lett.* **92**, 051101 (2008).
- [42] M. Forcales, N. J. Smith and R. G. Elliman, *Appl. Phys. Lett.* **100**, 014902 (2006).
- [43] D. K. Schroder, R. N. Thomas and J.C.Swartz, *IEEE T. Electron. Dev.* **ED-25**, 254 (1978).
- [44] D. Navarro-Urrios, N. Daldosso, C. Garcia, P. Pellegrino, B. Garrido, F. Gourbilleau, R. Rizk and L. Pavesi, *Jap. J. Appl. Phys.* **46**, 6626 (2007).
- [45] A. Green, *Silicon Solar Cells*, University of New South Wales, Sydney, (1995).
- [46] N. Daldosso, D. Navarro-Urrios, M. Melchiorri, L. Pavesi, F. Gourbilleau, M. Carrada, R. Rizk, C. García, P. Pellegrino, B. Garrido and L. Cognolato, *Appl. Phys. Lett.* **86**, 261103 (2005).
- [47] K. J. Vahala, *Nature* **424**, 839 (2003).
- [48] L. Rayleigh, *Philos. Mag.* **27**, 100 (1914).
- [49] D. K. Armani, T. J Kippenberg, S. M Spillane and K. J. Vahala, *Nature* **421**, 925 (2003).
- [50] R. W. Boyd and J. E. Heebner, *Appl. Optics* **40**, 5742 (2001).
- [51] T. J. Kippenberg, J. Kalkman, A. Polman and K. J. Vahala, *phys. Rev. A* **74**, 051802 (2006).
- [52] T. Aoki, B. Dayan, E. Wilcut, W. P. Bowen, A. S. Parkins, T. J. Kippenberg, K. J. Vahala and H. J. Kimble, *Nature* **443**, 671 (2006).
- [53] E. M. Purcell, *Phys. Rev.* **69**, 681 (1946).
- [54] A. Yariv, Y. Xu. R. K. Lee and A. Scherer, *Opt. Lett.* **24**, 711 (1999).

- [55] G. S. Wiederhecker, L. Chen, A. Gondarenko and M. Lipson, *Nature* **462**, 633 (2009).
- [56] P. Rakich, M. Soljacic and E. Ippen, *Nat. Photonics* **1**, 658 (2007).
- [57] B. D. Josephson, *Phys. Lett.* **1**, 251 (1962).
- [58] D. Sarchi, I. Carusotto, M. Wouters and V. Savona, *Phys. Rev. B* **77**, 125324 (2008).
- [59] D. Gerace, H. E. Türeci, A. Imamoglu, V. Giovannetti and R. Fazio, *Nat. Phot.* **5**, 281 (2009).
- [60] M. Albiez, R. Gati, J. Fölling, S. Hunsmann, M. Cristiani and M. K. Oberthaler, *Phys. Rev. Lett.* **95**, 010402 (2005).
- [61] R. Spano, N. Daldosso, M. Cazzanelli, L. Ferraioli, L. Tartara, J. Yu, V. Degiorgio, E. Jordana, J. M. Fedeli and L. Pavesi, *Opt. Expr.* **17**, 3941 (2009).
- [62] A. Taflove and M. E. Brodwin, *IEEE T. Microw. Theory* **23**, 623 (1975).
- [63] A. Taflove and S. C. Hagness, *Computational Electrodynamics: The Finite-Difference Time-Domain Method*, third edition, Artech House Publishers (2005).
- [64] A. Farjadpour, D. Roundy, A. Rodriguez, M. Ibanescu, P. Bermel, J. D. Joannopoulos, S. G. Johnson and G. Burr, *Opt. Lett.* **31**, 2972 (2006).
- [65] D. Smith, *Thin-Film Deposition: Principles and Practice*, McGraw-Hill (1995).
- [66] P. Pellegrino, B. Garrido, C. García, R. Ferrè, J.A. Moreno and J.R. Morante, *Physica E* **16**, 424 (2003).
- [67] V. A. Mandelsham and H. S. Taylor, *J. Chem. Phys.* **107**, 6756 (1997).  
Erratum, *ibid.* **109**, 4128 (1998).
- [68] R. G. Elliman, M. Forcales, A. R. Wilkinson and N.J. Smith, *Nucl. Instrum. Meth. Phys. Res. B* **257**, 11 (2007).
- [69] S. Foteinopoulou and C. M. Soukoulis, *Phys. Rev. B* **72**, 165112 (2005).
- [70] T. J. Kippenberg and K. J. Vahala, *Opt. Expr.* **15**, 17172 (2007).
- [71] L. D. Landau, E. M. Lifshitz, *Quantum Mechanics - Non relativistic theory (second edition)*, Elsevier Science (1965).
- [72] E. Yablonovitch, *Phys. Rev. Lett.* **58**, 2059 (1986).
- [73] J. M. Gérard, B. Sermage, B. Gayral, B. Legrand, E. Costard and V. Thierry-Mieg, *Phys. Rev. Lett.* **81**, 1110 (1998).
- [74] J. M. Gérard in *Single Quantum Dots: Fundamentals, Applications and New Concepts*, edited by P. Michler, Springer (2003).

- [75] L. T. Canham, *Appl. Phys. Lett.* **57**, 1046 (1990).
- [76] J.C. Vial, A. Bsiesy, F. Gaspard, R. Herino, M. Ligeon, F. Muller, R. Romestain and R.M. Macfarlane, *Phys. Rev. B* **45**, 14171 (1992).
- [77] P. D. J. Calcott, K. J. Nash, L. T. Canham, M. J. Kane and D. Brumhead *J. Phys.: Condens. Matter* **5**, L91 (1993).
- [78] M. Dovrat, Y. Oppenheim, J. Jedrzejewski, I. Balberg and A. Sa'ar, *Phys. Rev. B* **69**, 155311 (2004).
- [79] B. Gayral and J.M. Gérard, *Phys. Rev. B* **78**, 235306 (2008).
- [80] I. Sychugov, R. Juhasz, J. Valenta and J. Linnros, *Phys. Rev. Lett.* **94**, 087405 (2005).
- [81] Y. Akahane, T. Asano, B.-S. Song and S. Noda, *Opt. Expr.* **13**, 1202 (2005).
- [82] M. Eichenfield, C. P. Michael, R. Perahia and O. Painter, *Nat. Phot.* **1**, 416 (2007).
- [83] J. S. Levy<sup>1</sup>, A. Gondarenko<sup>1</sup>, M. A. Foster, A. C. Turner-Foster, A. L. Gaeta and Michal Lipson, *Nat. Phot.* **4**, 37 (2009).
- [84] L. Razzari, D. Duchesne, M. Ferrera, R. Morandotti, S. Chu, B. E. Little and D. J. Moss, *Nat. Phot.* **4**, 41 (2009).
- [85] J. C. Knight, G. Cheung, F. Jacques and T. A. Birks, *Opt. Lett.* **22**, 1129 (1997).
- [86] E. Peter, P. Senellart, D. Martrou, A. Lemaître, J. Hours, J. M. Gérard and J. Bloch, *Phys. Rev. Lett.* **95**, 067401 (2005).
- [87] M. L. Povinelli, S. G. Johnson, M. Lončar, M. Ibanescu, E. J. Smythe, F. Capasso and J. D. Joannopoulos, *Opt. Expr.* **13**, 8286 (2005).
- [88] J. B. Khurgin, R. S. Tucker, *Slow light: science and applications*, CRC Press - Taylor & Francis group (2009).
- [89] D. D. Smith, H. Chang, K. A. Fuller, A. T. Rosenberger and R. W. Boyd, *Phys. Rev. A* **69**, 063804 (2004).
- [90] R. W. Boyd, *Nonlinear optics (third edition)*, Elsevier Academic Press (2008).
- [91] P. Del'Haye, A. Schliesser, O. Arcizet, T. Wilken, R. Holzwarth and T. J. Kippenberg, *Nature* **450**, 1214 (2007).
- [92] M. Fleischhauer, A. Imamoglu and J. P. Marangos (2005), *Rev. Mod. Phys.* **77**, 633 (2005).
- [93] P. Palinginis, F. Sedgwick, S. Crankshaw, M. Moewe and C. J. Chang-Hasnain, *Opt. Expr.* **13**, 9909 (2005).

- [94] Y. A. Vlasov, M. O'Boyle, H. F. Hamann and S. J. McNab, *Nature* **438**, 65 (2005).
- [95] A. Melloni, F. Morichetti and M. Martinelli, *Opt. Photonics News* **14**, 44 (2003).
- [96] T. Baba, *Nat. Phot.* **2**, 465 (2008).
- [97] F. Xia, L. Sekaric and Y. Vlasov, *Nat. Phot.* **1**, 65 (2007).
- [98] M. Soljacic and J. D. Joannopoulos, *Nat. Mater.* **3**, 211 (2004).
- [99] S. John, *Phys. Rev. Lett.* **58**, 2486 (1987).
- [100] V. S. C. Manga Rao and S. Hughes, *Phys. Rev. B* **75**, 205437 (2007).
- [101] V. S. C. Manga Rao and S. Hughes, *Phys. Rev. Lett.* **99**, 193901 (2007).
- [102] S. John and T. Quang, *Phys. Rev. Lett.* **74**, 3419 (1995).
- [103] V. R. Almeida, Q. Xu, C. A. Barrios and M. Lipson, *Opt. Lett.* **29**, 1209 (2004).
- [104] J. D. Joannopoulos, S. G. Johnson, J. N. Winn and R. D. Meade, *Photonic crystals: molding the flow of light (second edition)*, Princeton University Press (2008).
- [105] S. G. Johnson and J. D. Joannopoulos, *Opt. Expr.* **8**, 173 (2001).
- [106] F. Riboli, P. Bettotti and L. Pavesi, *Opt. Expr.* **15**, 11769 (2007).
- [107] A. Pitanti, P. Bettotti, R. Guider, E. Rigo, N. Daldosso, J.M. Fedeli and L. Pavesi, *Group IV Photonics*, 2008 5th IEEE International Conference, 17-19 September 2008.
- [108] L. C. Andreani, D. Gerace and M. Agio, *Photonic Nanostruct.* **2**, 103 (2004).
- [109] T. F. Krauss, *J. Phys. D: Appl. Phys.* **40**, 2666 (2007).
- [110] M. Ghulinyan, M. Galli, C. Toninelli, J. Bertolotti, S. Gottardo, F. Marabelli, D. S. Wiersma, L. Pavesi and L. C. Andreani *Appl. Phys. Lett.* **88**, 241103 (2006).
- [111] Y.-H. Ye, J. Ding, D.-Y. Jeong, I. C. Khoo and Q. M. Zhang, *Phys. Rev. E* **69**, 056604 (2004).
- [112] Y. Akahane, T. Asano, B.-S. Song and S. Noda, *Nature* **425**, 944 (2003).
- [113] K. Srinivasan and O. Painter, *Opt. Expr.* **10**, 670 (2002).
- [114] R. Guider, N. Daldosso, A. Pitanti, E. Jordana, J. M. Fedeli and L. Pavesi, *Opt. Expr.* **17**, 20762 (2009).

- [115] A. Di Falco, L. O’Faolain and T. F. Krauss, *Appl. Phys. Lett.* **92**, 083501 (2008).
- [116] B. Corcoran, C. Monat, C. Grillet, D. J. Moss, B. J. Eggleton, T. P. White, L. O’Faolain and T. F. Krauss, *Nat. Phot.* **3**, 206 (2009).
- [117] S. Hughes, *Opt. Lett.* **29**, 2659 (2004).
- [118] T. Junno, K. Deppert, L. Montelius and L. Samuelson, *Appl. Phys. Lett.* **66**, 3627 (1995).
- [119] K. Hennessy, A. Badolato, M. Winger, D. Gerace, M. Atatüre, S. Gulde, S. Fält, E. L. Hu and A. Imamoglu, *Nature*, **445**, 896 (2007).
- [120] R. C. McPhedran, L. C. Botten, J. McOrist, A. A. Asatryan and C. M. de Sterke, *Phys. Rev. E* **69**, 016609 (2004).
- [121] A. J. Ward and J. B. Pendry, *Phys. Rev. B* **58**, 7252 (1998).
- [122] R. H. Dicke, *Phys. Rev.* **93**, 99 (1954).
- [123] , A. V. Andreev, V. I. Emel’yanov and Yu. A. Il’inskii, *Sov. Phys. Usp.* **23**, 493 (1980).
- [124] M. Scheibner, T. Schmidt, L. Worschech, A. Forchel, G. Bacher, T. Passow and D. Hommel, *Nat. Phys.* **3**, 106 (2007).
- [125] N. Vats and S. John, *Phys. Rev. A* **58**, 4168 (1998).
- [126] A. Shojiguchi, K. Kobayashi, S. Sangu, K. Kitahara and M. Ohtsu, *A phenomenological description of optical near fields and optical properties of N two-level systems interacting with optical near fields*. In: *Progress in Nano-Electro-Optics III* edited by M. Ohtsu, Springer (2005).